GOLD-NANOPARTICLE-BASED THERANOSTIC AGENTS FOR RADIOTHERAPY OF MALIGNANT SOLID TUMORS

by

SINA MOEENDARBARI

Presented to the Faculty of the Graduate School of

The University of Texas at Arlington in Partial Fulfillment

of the Requirements

for the Degree of

DOCTOR OF PHILOSOPHY

THE UNIVERSITY OF TEXAS AT ARLINGTON

August 2016

Copyright © by Sina Moeendarbari 2016

All Rights Reserved

Acknowledgements

I would like to express my sincere gratitude to my supervisor, Dr. Yaowu Hao, for his guidance and kind support during the last four years. This work could not have been done without his knowledge, help, encouragement, perseverance, and constructive attitude.

I am truly grateful to a great team of researchers and scientists in the Radiology Department of UTSouthwestern Medical Center in Dallas, Aditi Mulgaonkar, Rakesh Tekade, Saleh Ramezani, Preston Christensen, and Dr. Weihua Mao, who greatly contributed to this study. I specially appreciate Dr. Xiankai Sun, whose knowledge and intimate support made this work possible.

Special thanks to my colleagues in Nanoscale Materials Lab in the department of materials science and engineering, Chienwen Huang, Ruiqian Jiang, Orathai Thumthan, Christopher Pickering, Akshay S Hande, and Chivarat Muangphat, who helped me with many experiments during the entire of this study, and shared with me their valuable experiences.

I would like to thank all the professors and staffs in the department of materials science and engineering, Nanofab Research Center, and Characterization Center for Materials & Biology for providing a wonderful friendly atmosphere during my program. Also, I give many thanks to all my friends who I cannot list all their names here for their help, thoughts, well-wishes, and being there whenever I needed a friend.

Finally, I have to thank my family for their love, support, and encouragement. This work is dedicated to them for their endless love and sacrifices throughout my life.

September 9th, 2016

Abstract

GOLD-NANOPARTICLE-BASED THERANOSTIC AGENTS FOR RADIOTHERAPY OF MALIGNANT SOLID TUMORS

Sina Moeendarbari, PhD

The University of Texas at Arlington, 2016

Supervising Professor: Yaowu Hao

Radiation therapy is one of the three major methods of cancer treatment. The fundamental goal of radiotherapy is to deliver high radiation doses to targets while simultaneously minimizing doses to critical structures and healthy normal tissues. The aim of this study is to develop a general, practical, and facile method to prepare nanoscale theranostic agents for more efficacious radiation therapy with less adverse side effects. First, a novel type of gold nanoparticle, hollow Au nanoparticles (HAuNPs) which was synthesized using the unique bubble template synthesis method developed in our lab, are studied in vitro and in vivo to investigate their effect as radiosensitizing agents to enhance the radiation dose during external radiotherapy. The results showed the promising potential of using HAuNPs as radiosensitization agents for efficacious treatment of breast cancer. Second, a novel radiolabeling method is developed to incorporate medical radioisotopes to gold nanoparticles. We incorporate palladium-103 (^{103}Pd), a radioisotope currently in clinical brachytherapy, into a hollow gold nanoparticle. The resulting ^{103}Pd@Au nanoparticles in the form of a colloidal suspension can be administered by direct injection into tumors, serving as internal radiation sources (nanoseeds) for radiation therapy. The size of the nanoseed, ~150nm in diameter, is

large enough to prevent nanoseeds from diffusing into other areas while still small enough to allow them to homogeneously distribute inside the tumor. The therapeutic efficacy of ^{103}Pd@Au nanoseeds have been tested when intratumorally injected into a prostate cancer xenograft model. The findings showed that this nanoseed-based brachytherapy has the potential to provide a theranostic solution to unresectable solid tumors. Finally, to make real clinical application more plausible, multi-functional magnetic nanoseeds nanoparticles for imaging-guided radiotherapy are synthesized and characterized.

Table of Contents

Acknowledgements iii

Abstract iv

List of Illustrations xi

List of Tables xvi

Chapter 1 Introduction 1

Chapter 2 Background information 4

2.1 Cancer Treatments 4

2.1.1 Surgery 5

2.1.2 Chemotherapy 6

2.1.3 Radiation Therapy 6

2.1.3.1 External beam radiation therapy (EBRT) 7

2.1.3.2 Internal radiation therapy (Brachytherapy) 9

2.1.3.2.1 Brachytherapy techniques 9

2.1.3.2.2 Brachytherapy dose rates 11

2.1.3.2.3 Brachytherapy radioisotopes 12

2.1.3.2.4 Brachytherapy of prostate cancer 14

2.1.3.2.5 Brachytherapy using nanotechnology 16

2.1.3.3 Systemic radiation therapy (Radiopharmaceutical) 20

2.1.3.4 Radiotherapy of breast cancer 21

2.2 Gold nanoparticles in cancer diagnosis and treatment 22

2.2.1 Physical and biological properties of AuNPs 22

2.2.2 Synthesis methods and different types of AuNPs 23

2.2.3 AuNPs as diagnostic agents 25

2.2.4 AuNPs as therapeutic agents 26

2.2.4.1 Photothermal therapy using AuNPs 26
2.2.4.2 Radiotherapy using AuNPs 29
2.2.4.2.1 Radiosensitization concept 29
2.2.4.2.2 Radiosensitization mechanisms by AuNPs 30
2.2.4.2.3 In vivo studies on AuNPs used as radiosensitization agents 32
2.2.4.3 Hyperthermia using AuNPs 36
2.2.4.4 Drug delivery using AuNPs 37
2.2.5 Toxicity of AuNPs 38
Chapter 3 Hollow gold nanoparticles as efficient radiosensitizing agents for radiation therapy of breast cancer 41
3.1 Introduction 41
3.2 In vitro analysis 43
3.2.1 Cell culture 43
3.2.2 Synthesis and characterization of HAuNPs 43
3.2.3 X-ray irradiation of cells 44
3.2.4 Clonogenic assay 45
3.2.5 Cytotoxicity study method 45
3.2.6 Uptake of HAuNPs by MDA-MB-231 cells 45
3.2.7 Evaluation of cytotoxicity of HAuNPs 46
3.2.8 Dose enhancement in cells irradiated with x-ray 48
3.3 In vivo analysis 49
3.3.1 Animal tumor model 49
3.3.2 Computed Tomography of Mice 50
3.3.3 X-ray irradiation of the tumor bearing mice 51

3.3.4 Radiosensitization effect of HAuNPs in mice bearing breast cancer tumors 53
3.3.4.1 Tumor growth delay study 53
3.3.4.2 Magnetic Resonance Imaging (MRI) of tumors 55
3.3.4.3 Survival study 55
3.3.5 Radiosensitization mechanisms by HAuNPs 57
3.3.6 Toxicological analysis after treatment with HAuNPs and radiation therapy 60
3.3.7 Ex vivo biodistribution analysis of HAuNPs 63
Chapter 4 Radioactive gold nanoparticles for efficacious brachytherapy of solid malignant tumors 65
4.1 Introduction 65
4.2 Synthesis of AuNP-based radioactive nanoseeds 67
4.2.1 Synthesis design of theranostic nanoseeds 67
4.2.2 Materials 68
4.2.3 Synthesis of hollow gold nanoparticles (HAuNPs) 69
4.2.4 Synthesis of Cu-coated HAuNPs 69
4.2.5 Synthesis of ^{103}Pd@Au nanoseeds 70
4.2.6 Synthesis of ^{198}Au@Au nanoseeds 72
4.3 Administration of nanoseeds into tumor xenografts and their in vivo biodistribution 75
4.3.1 Animal model 75
4.3.2 Intratumoral administration of cold nanoparticles and hot nanoseeds 75
4.3.3 SPECT imaging using the low energy emission of ^{103}Pd 76

4.3.4 SPECT analysis to monitor in vivo tumor retention of the nanoseeds 76
4.4 Therapeutic efficacy of ^{103}Pd@Au nanoseeds in brachytherapy of prostate cancer 78
4.4.1 Tumor growth study 78
4.4.2 FDG-PET/CT imaging analysis 80
4.5 In vivo toxicity studies 84
4.6 Ex vivo biodistribution study 88
4.6.1 Ex vivo biodistribution study methods 88
4.6.2 Ex vivo biodistribution measurement results 88
4.7 Prospective clinical applications and practical significance of nanoseeds 91
Chapter 5 Magnetic nanoseeds for MRI-guided brachytherapy 94
5.1 Introduction 94
5.2 Design and synthesis of magnetic nanoseeds 97
5.2.1 Electroless deposition of cobalt 97
5.2.2 Synthesis methods and materials 98
5.2.3 Chemical reactions of the cobalt electroless deposition 99
5.3 Morphological and structural characterization 102
5.3.1 Au@Pd@Co nanoparticles 102
5.3.2 Au@Pd@Co@Au nanoparticles 106
5.4 Magnetic properties of the magnetic nanoseeds 112
5.4.1 Magnetic anisotropy 112
5.4.2 Physical basis of superparamagnetism 113
5.4.3 Superparamagnetic nanoparticles 115

5.4.4 Magnetic properties measurement by VSM 115
5.4.5 Magnetic behavior of Au@Pd@Co and Au@Pd@Co@Au nanoparticles 116
5.5 Magnetic resonance imaging (MRI) preliminary study 121
Chapter 6 Summary 122
References 124
Biographical Information 144

List of Illustrations

Figure 2-1 10 leading cancer types for the estimated new cancer cases and deaths by sex, United States, 2016 [1]..... 5

Figure 2-2 (a) Intracavity[14] and (b) interstitial[13] brachytherapy techniques. 11

Figure 2-3 AuNPs with various size and morphologies with potential biomedical applications. Adapted with permission from [68]..... 24

Figure 2-4 Schematic illustration of ionizations caused by (a) Compton, and (b) Photoelectric effects{Butterworth, 2012 #268}..... 31

Figure 3-1 TEM and SEM images of HAuNPs..... 44

Figure 3-2 Microscopic images showing that (a) HAuNPs are internalized within the MDA-MB-231 cells after 24 hours of incubation. (b) control MDA-MB-231 without HAuNPs.... 46

Figure 3-3 Effects of HAuNPs on clonogenic survival rate. The cytotoxicity of HAuNPs following 10 days exposure to gold concentrations of 70, 105, 140 , 210, 280 and 350 µM. Surviving fractions were normalized to untreated control cells (Au 0 µM) in each of the experiments..... 47

Figure 3-4 Survival curves for MBA-MB-231 cells irradiated with (a) 225 kVp X-rays, in which cells were given a 2 Gy, 4Gy and 6 Gy doses, and (b) 6 MVp X-rays, in which cells were given a 4Gy and 6 Gy doses. In both curves, the blue line refers to control cells whereas the red line is for cells cultured in the presence of 140 µM HAuNPs. For the survival curves, each data point represents the average of three independent experiments each plated in quintuplicate..... 48

Figure 3-5 HAuNPs (2.8 mg/g tumor, 40 µL total volume) were injected at 5 to 6 sites on each tumor of mice in Group A and C. Coronal (left) and sagittal (right) planes of the CT image for one representative mouse are shown here. Yellow circle indicates the tumor with the injected HAuNPs, seen as bright white spots..... 51

Figure 3-6 Experimental set up for the X-ray irradiation of tumor-burdened mice in Treatment Groups A and B. 52
Figure 3-7 Tumor growth volume as measured by calipers (**a**) and MRI (**b**) and normalized to day 1 of radiotherapy. The data are represented as the Mean ± SEM for 7 mice at the start of the treatment. The animal number decreased as the result from the death or sacrificing of the animals over the course of the study. 54
Figure 3-8 Kaplan-Meier survival curves for treatments Groups A, B, C, and D. n = 7 in each group. 56
Figure 3-9 Normalized weight during the study period for Groups A, B, C, and D. 60
Figure 3-10 Toxicological analysis of blood samples collected from 4 study groups of mice. a) Hematological toxicity analysis; b) Hepatotoxicity analysis; c) Nephrotoxicity analysis. Each measurement is expressed as Mean ± SEM (n = 4). Statistical comparisons were performed using one-way ANOVA analysis followed by Tukey's post hoc test for multiple comparisons; * and ** for p-values < 0.05 and 0.01, respectively. RBC – red blood cells, WBC – white blood cells, ALT – alanine aminotransferase, AST – aspartate aminotransferase, SCr – serum creatinine, BUN – blood urea nitrogen. 62
Figure 4-1 Synthesis design of ^{103}Pd@Au nanoseeds**;** schematic of the process of incorporation of ^{103}Pd radioisotope onto HAuNPs. First, a Cu layer is deposited by an electroless deposition process. Then, the some Cu atoms are replaced by ^{103}Pd radioisotopes through galvanic exchange, and finally Pd atoms replace remaining Cu layer by the same reaction. The synthesized nanoseeds will emit Auger electrons and characteristic x-rays. 68
Figure 4-2 (a) HRTEM image of hollow gold nanoparticle before Pd coating, and (b) HRTEM image of Au@Pd core-shell nanoseeds with EDS spectrums of the Au core and

Pd shell of Au@Pd nanoseeds and high magnification HRTEM image of the outer Pd layers showing the lattice fringes of Pd. 71

Figure 4-3 High resolution TEM micrograph of Au@Au nanoparticles. The scale bar is 20 nm. 74

Figure 4-4 Retention of the injected ^{103}Pd@Au nanoseeds at tumor sites. (a) Serial SPECT/CT imaging performed 0, 1, 2, 4, 7, 14, 21, and 35 days post intratumoral injection of 1.51 mCi ^{103}Pd@Au nanoseeds in PC3 tumor bearing SCID mice. White arrows indicate tumors and the radioactivity coming from ^{103}Pd, (b) the quantitative SPECT analysis of radioactivity (quantified as percentage injected dose per gram, %ID/g) from tumor, liver and spleen. %ID/g associated with tumor increased progressively due to the reduction in tumor volume. 77

Figure 4-5 (a) Tumor volume and (b) body weight during the progression of therapy. 79

Figure 4-6 Assessment of the therapeutic efficacy of ^{103}Pd@Au nanoseeds in PC3 tumor bearing mice by PET/CT imaging**.** (a) Serial FDG-PET/CT images acquired at 0, 7, 21, and 35 days post intratumoral injection of PBS (upper panel), cold Au@Pd nanoparticles (middle panel), and hot ^{103}Pd@Au nanoseeds (lower panel). A significant tumor FDG uptake reduction was observed in the treatment group with ^{103}Pd@Au nanoseeds as compared to that in the PBS and cold Au@Pd nanoparticles treated groups. White arrows indicate tumor sites. (b) Quantitative PET analysis (SUV_{max} values versus time), (c) Comparative tumor volume changes determined by CT scan analysis (mean ± SEM). 82

Figure 4-7 (a) BUN, mg/dl, (b) creatining mg/dL, (c) AST, U/L, and (d) ALT, U/L levels in control, cold nanoparticle treated and nanoseeds treated mice. 86

Figure 4-8 (a) RBC m/µL, (b) WBC, K/ µL, (c) platelet count, K/ µL, (d) MCH. Pg, (e) reticulosites, K/ µL, (f) basophils, K/ µL, (g) Neutrophils, %, (h) Eosinophils, % in control, cold nanoparticles treated and nanoseeds treated mice. 87
Figure 4-9 Radioactivity of dissected organs measured by a gamma counter (means ± SEM). 89
Figure 4-10. Retention of (a) Au, and (b) Pd content measured by ICP-MS in different organs of the mice from 1 day to 5 weeks post-injection of the nanoseeds (means ± SEM). 90
Figure 5-1(a) Chemical structure of DMAB molecule, and (b) broken N-B bond in DMAB molecule and the resultant electron density over N and B atoms. 99
Figure 5-2 SEM images of APC NPs at low to high magnifications. 103
Figure 5-3 TEM images of APC NPs with (a) low, (b) high magnifications and (c) EDX spectrum of the nanoparticles. 104
Figure 5-4 HRTEM images of annealed APC NPs at 200 ^{o}C for 2 hours, showing the partial crystallization of amorphous cobalt layer. The crystalized parts can be noticed by the revealed lattice fringes. 106
Figure 5-5 (a) SEM image and (b-d) TEM images of APCA NPs. 107
Figure 5-6 (a) TEM, (b) STEM image of APCA NP and (c) their corresponding EDS line scan. 109
Figure 5-7 Magnetic hysteresis loop of Au-Pd-Co core-shell NPs (APC) at room temperature. 117
Figure 5-8 Magnetic hysteresis loop of Au-Pd-Co-Au core-shell NPs (APCA) at room temperature. 119
Figure 5-9 Magnetic properties of APC and APCA NPs measured by VSM at room temperature. 120

Figure 5-10 T_2-weighted image of MRI phantom scan of magnetic nanoseeds solution beside DI water. 121

List of Tables

Table 2-1 Different types of brachytherapy implants/techniques[15] 10

Table 2-2 Properties of common brachytherapy radioactive sources 13

Chapter 1 Introduction

Cancer is a major public health problem worldwide and is the second leading cause of death in the United States[1]. It is a group of diseases characterized by the uncontrolled growth and spread of abnormal cells. Cancer can generally have two forms; solid tumors (mass of cancerous tissue), and leukemia (blood spread and liquid cancer). For patients with solid malignant tumors, the surgical resection of the entire tumor with clear margins is the most effective treatment. However, many solid tumors are considered “unresectable” because they adhere to vital structures or the surgery would cause irreversible damages to the patients and severely impair their quality of life. Such solid tumors can arise from a variety of cancer types including lung, colon, pancreatic, liver, ovarian, head and neck, prostate and others[2-8]. Also, for patients with metastatic cancers, the resection may cause considerable morbidity since they have already been weakened by their metastatic diseases, chemotherapy, and/or radiation therapy.

In order to prevent the tumor growth or provide complete tumor resolution without surgery for such cancers, a variety of cytotoxic drugs and radiation therapies are currently in clinical practice. Unfortunately, severe adverse side effects are usually associated with these therapeutic modalities. Since these tumors are already locally advanced or have begun to metastasize, the outlook today for these cancer patients is bleak and survival rate remains very low.

The use of radiation therapy for the treatment of cancer dates back to the beginning of the 20th century, remarkably soon after Marie and Pierre Curie discovered radium in 1898[9]. Now, highly localized radiotherapy using advanced radiotherapy machines or radioisotopes has become a standard treatment option for many cancers. Radiotherapy has not only been used to cure tumors, but also to prevent the reoccurrence of cancer after surgery. For example, radiation therapy has been commonly used to treat breast cancer after breast-conserving surgery to help lower the recurrence. However, these benefits are restricted by the side effects

associated with radiotherapy. The fundamental goal of radiotherapy is to deliver high radiation doses to targets while simultaneously minimizing doses to critical structures and healthy normal tissues.

The objective of this study is to provide a safer and more efficient radiotherapy to treat malignant solid tumors, specifically the two most common non-skin types of cancer; breast and prostate cancers. Gold nanoparticles, with their unique physical and biological characteristics, are used to develop a new kind of nanomedicine for radiotherapy. First, a novel type of gold nanoparticle (HAuNPs) are studied in vitro and in vivo to investigate their effect as radiosensitizing agents to enhance the radiation dose during external radiotherapy. The radiation damage will be selectively enhanced only within tumors, which will lower the total radiation dosage while still achieving the same treatment effect as conventional high dose radiation therapy. The results showed the promising potential of using HAuNPs as radiosensitization agents for efficacious treatment of breast cancer. Second, a novel radiolabeling method is developed to incorporate medical radioisotopes to gold nanoparticles. We incorporate palladium-103 (^{103}Pd), a radioisotope currently in clinical brachytherapy, into a hollow gold nanoparticle. The resulting ^{103}Pd@Au nanoparticles in the form of a colloidal suspension can be administered by direct injection into tumors, serving as internal radiation sources (nanoseeds) for radiation therapy. The size of the nanoseed, ~150nm in diameter, is large enough to prevent nanoseeds from diffusing into other areas while still small enough to allow them to homogeneously distribute inside the tumor. The therapeutic efficacy of ^{103}Pd@Au nanoseeds have been tested when intratumorally injected into a prostate cancer xenograft model. Remarkably, we observed an averaged tumor burden reduction of 80% as compared to a control cohort administered with the corresponding intact Au nanoseeds (n = 12). In addition, we were able to develop a practical single-photon emission computed tomography (SPECT) imaging method using the low energy emission of ^{103}Pd to noninvasively monitor the tumor retention of ^{103}Pd@Au nanoseeds, which was found to be virtually 100% over the entire course

of our 5-week preliminary study. The findings showed that this nanoseed-based brachytherapy has the potential to provide a theranostic solution to unresectable solid tumors. Finally, to make real clinical application more plausible, multi-functional magnetic nanoseeds nanoparticles are synthesized for imaging-guided radiotherapy.

Chapter 2 Background information

2.1 Cancer Treatments

Cancer, defined as uncontrollable change and growth of cells in body, is the second leading cause of death in the United States, placed only after heart disease. In most types of cancer, the uncontrollable growth and proliferation of cancer cells would eventually lead to form a lump or mass of cells called malignant tumor. Malignant tumors are generally distinguished from Leukemia by using the term of “solid tumors”. Leukemia is a type of cancer that takes on the fluid properties of the organ it affects (like blood), while solid tumors are mass of tissue that usually does not contain cysts or liquid areas. Solid tumors can occur in several places of body, including bones, muscles, organs, and based on their forming cells, different types of solid tumors are named and classified (such as sarcomas, carcinomas, and lymphomas)[10].

It has been estimated that about 1,685,210 new cancer cases to be diagnosed in 2016, from which, about 595,690 Americans are expected to die of cancer in the same year[1]. This translates to about 1,630 people per day, and accounts for nearly 1 of every 4 deaths in the US. The maximum number among this cancer prevalence is related to solid tumors. Figure 2-1 demonstrates the rates of cancer incidence and death of common cancer types by sex in the United States for 2016. As can be seen, prostate and breast cancers are the most common types of cancer in American men and women, respectively. The increasing trend of cancer incidence has forced the human societies and governments to work more on the cancer prevention and treatments. The most commonly used treatment modalities for cancer include some combination of surgery, radiation therapy, and chemotherapy. Newer forms of treatment continue to emerge.

Estimated New Cases

Males			Females		
Prostate	180,890	21%	Breast	246,660	29%
Lung & bronchus	117,920	14%	Lung & bronchus	106,470	13%
Colon & rectum	70,820	8%	Colon & rectum	63,670	8%
Urinary bladder	58,950	7%	Uterine corpus	60,050	7%
Melanoma of the skin	46,870	6%	Thyroid	49,350	6%
Non-Hodgkin lymphoma	40,170	5%	Non-Hodgkin lymphoma	32,410	4%
Kidney & renal pelvis	39,650	5%	Melanoma of the skin	29,510	3%
Oral cavity & pharynx	34,780	4%	Leukemia	26,050	3%
Leukemia	34,090	4%	Pancreas	25,400	3%
Liver & intrahepatic bile duct	28,410	3%	Kidney & renal pelvis	23,050	3%
All Sites	**841,390**	**100%**	**All Sites**	**843,820**	**100%**

Estimated Deaths

Males			Females		
Lung & bronchus	85,920	27%	Lung & bronchus	72,160	26%
Prostate	26,120	8%	Breast	40,450	14%
Colon & rectum	26,020	8%	Colon & rectum	23,170	8%
Pancreas	21,450	7%	Pancreas	20,330	7%
Liver & intrahepatic bile duct	18,280	6%	Ovary	14,240	5%
Leukemia	14,130	4%	Uterine corpus	10,470	4%
Esophagus	12,720	4%	Leukemia	10,270	4%
Urinary bladder	11,820	4%	Liver & intrahepatic bile duct	8,890	3%
Non-Hodgkin lymphoma	11,520	4%	Non-Hodgkin lymphoma	8,630	3%
Brain & other nervous system	9,440	3%	Brain & other nervous system	6,610	2%
All Sites	**314,290**	**100%**	**All Sites**	**281,400**	**100%**

Figure 2-1 10 leading cancer types for the estimated new cancer cases and deaths by sex, United States, 2016 [1].

2.1.1 Surgery

The most frequently employed form of cancer treatment is the tumor excision. More patients are cured of cancer with surgery than any other treatment method. Nevertheless, surgery, like all other treatment modalities, suffers from a number of limitations; naturally, large and invasive tumors that adhere to vital body structures are unresectable. This is also true for metastatic diseases and hematological malignancies. Moreover, the tolerance of surgery is low or unbearable for some patients with co-existing systemic disease (like cardiovascular or diabetes). Most solid malignancies spread by way of lymphatic. Hence, removal of regional lymph nodes is often performed along with tumor resection to increase the chance of treatment

[10]. Extensive surgery, however, may affect surrounding normal tissues leading to significant deformation or organ dysfunction. Bleeding, blood clots, pain, drug reactions, and infection at the surgery site are some other possible side effects. Recently, combining surgery with other treatment modalities such as chemotherapy and radiation therapy has enhanced its effectiveness.

2.1.2 Chemotherapy

Cancer chemotherapy was initially emerged in 1960s as a means to treat systemic disease, as both surgery and radiotherapy had not been useful for metastatic cancers. The target of most chemotherapeutic agents is malignant cells that are actively replicating. Drug resistance (inherent and/or acquired) by cancer cells, toxicity to normal cells, and inadequate cytotoxic concentrations inside the solid tumors are major problems associated with chemotherapy. Most anticancer drugs have narrow therapeutic index, form multidrug resistance (MDR), and present non-specific biodistribution upon intravenous (IV) administration, leading to severe side effects to healthy tissues, especially tissues that contain fast-growing cells such as bone marrow and hair follicles. These limitations of conventional chemotherapeutic strategies commonly result in suboptimal dosing, treatment delay or discontinuance and reduced patient compliance to the therapy [11]. New approaches in the modern cancer chemotherapy to overcome these intrinsic limitations include molecularly-targeted drugs and combination chemotherapeutics.

2.1.3 Radiation Therapy

Radiation therapy (radiotherapy) is another primary cancer treatment modality, which is received by around half of all cancer patients as their primary treatment or in combination with other treatments. Radiotherapy is used to treat cancer in several cases; to cure or shrink early-stage malignant tumors, to stop cancer from recurring in the treated site or another area, and to

treat symptoms caused by an advanced cancer (palliative radiation). In general, radiotherapy uses ionizing radiation (high-energy photons or particle beams) to damage the DNA of cells by either directly breaking their strands or generating free radicals that subsequently attack DNAs. The DNA damage would result in apoptosis and cell death. However, the response of different types of cells to radiation (radiosensitivity) is different. Cancer cells tend to divide quickly and grow out of control. Radiotherapy kills cancer cells that are dividing, but it also affects dividing cells of normal tissues, which eventually causes unwanted side effects. The radiotherapy side effects can be acute and/or chronical, where tissues that grow quickly, such as skin, mucous membranes, bone marrow, and the lining of the intestines, are often subjected to immediate side effects, while nerve, breast, and bone tissue show later effects. Late effects are due to microvascular damages.

Since the beginning of widespread clinical application of radiotherapy to cure cancer back in 1960s, several forms and strategies of radiotherapy have been developed. Nonetheless, based on the type of radiation source, radiotherapy can be generally sorted into three major classes; external beam radiotherapy (teletherapy), internal radiotherapy (brachytherapy), and systemic radiation therapy. The type of prescribed radiotherapy depends on a number of factors, including type and size of cancer, the tumor location inside the body, the radiosensitivity of targeted tissues, and the general health and medical history of the patient.

2.1.3.1 External beam radiation therapy (EBRT)

In this type of radiotherapy the ionizing radiation is directed from a distance from body to tumor site, and it is the most widely used type of radiation therapy. The beam can be in the form of photons of electromagnetic x-ray or gamma rays generated by linear accelerators or cobalt-60 units, or alternatively in the form of high-energy charged particles, like electrons, protons, neurons and alpha particles. This method is mainly used for deep tumors, and patients usually receive the total required radiation dose in daily treatment sessions over a period of time

(several weeks, the process known as radiation dose fractions). Although in EBRT the radiation is aimed at the tumor, it still affects the normal tissue it passes through on its way into and out of the body. Since EBRT is a local treatment, side effects largely depend on the area of the body being treated. External beam radiotherapy itself includes different types, such as [12]:

- **3-dimentional conformal radiation therapy (3D-CRT):** 3D-CRT uses very sophisticated computer software and advanced imaging/treatment machines to deliver radiation to very precisely shaped target areas.
- **Intensity-modulated radiation therapy (IMRT):** IMRT uses hundreds of tiny radiation beam-shaping devices, called collimators (or multi-leaf collimators), to deliver a single dose of radiation. The collimators can be stationary or can move during treatment, allowing the intensity of the radiation beams to be adjusted during treatment sessions. This kind of dose modulation allows different areas of a tumor or nearby tissues to receive different doses of radiation.
- **Image-guided radiation therapy (IGRT):** In IGRT, repeated imaging scans (CT, MRI, or PET) are performed during treatment. Repeated imaging can increase the accuracy of radiation treatment and may allow reductions in the planned volume of tissue to be treated, thereby decreasing the total radiation dose to normal tissue.
- **TomoTherapy**: It is a type of IMRT. A tomotherapy machine is a hybrid between a CT imaging scanner and an external-beam radiation therapy machine.
- **Stereotactic radiosurgery (SRS):** SRS uses extremely accurate image-guided tumor targeting and patient positioning to deliver a large, precise dose of radiation to a small, well-defined tumor. Therefore, a high dose of radiation can be given without excess damage to normal tissue. It is most commonly used in the treatment of brain or spinal tumors and brain metastases from other cancer types.

2.1.3.2 Internal radiation therapy (Brachytherapy)

In brachytherapy, the source of radiation (radioactive materials, usually small, encapsulated radionuclides) is directly placed inside or near the area to be treated. Thus, in significant contrast to EBRT, the radiation beam does not need to cross through normal tissue to reach the targeted tumor cells. Radiation dose is inversely proportional to the square of the distance from the source. Therefore, brachytherapy allows for a very high dose to the tumor with relative sparing of the surrounding normal structures. The dose can be delivered for a short time (temporary implants) or a long period of time that is enough for complete decay of the radionuclides (permanent implants). Brachytherapy has a wide clinical applications and has been used for many different cancer types as a sole modality or in conjunction with EBRT[13] and chemotherapy. In addition, it has been used intraoperatively in situations where optimal surgical resection is not possible, as well as postoperatively to target potential regions of residual microscopic disease[14].

2.1.3.2.1 Brachytherapy techniques

Brachytherapy can be classified based on a number of parameters, such as the method of source placement, dose rate and/or duration of irradiation, and loading pattern. Radiation sources can be placed temporary or permanent and are available in varied forms, such as tubes, catheters, wires, needles, pellets, and seeds. Different types of brachytherapy based on the positioning of radiation source are summarized in Table 2-1. Brachytherapy can be generally classified in two major groups according to the approach of radiation source positioning; surgical and surface contact (superficial). Two common types of surgical brachytherapy are interstitial and intracavitary, shown in Figure 2-2.In interstitial brachytherapy, sealed radioactive sources are implanted within the tumor, whereas in intracavitary brachytherapy the radiation sources are placed inside body cavities close to the tumor. The choice of technique depends primarily on disease extent and anatomy. Intracavitary

brachytherapy has been the most commonly practiced form of brachytherapy for cervical cancer[13], while interstitial brachytherapy has been widely used for prostate cancer.

Episclar brachytherapy (or eye plaque brachytherapy) is another type of brachytherapy which is at the interface between surgical and surface methods. Episcleral eye plaque brachytherapy (also called ophthalmic brachytherapy) is intended as an eye-conserving procedure (replacing enucleation or the removal of the eye) in which a small metallic “plaque” containing sealed radioactive sources (seeds) is temporarily (around a week) placed on the wall of the eye adjacent to the tumor. In other words, the radiation source (plaque) is attached to the surface of the targeted area (eye) through a surgical process, and left in place until the required dose has been delivered.

Table 2-1 Different types of brachytherapy implants/techniques[15]

Type of implant	**Description**	**Clinical applications**
Intracavitary	Sources are placed into body cavities close to the tumor volume	Gynec.malign, nasopharynx
Interstitial	Sources are implanted surgically within the tumor volume	Prostate
Intraoperative	Sources are implanted into the target tissue during surgery	retroperitoneal, sarcoma, pancreatic, rectal, pediatric tumors, malignant thoracic
Intravascular	A single source is placed into small or large arteries	Coronaries, peripheral art. internal mammary
Intraluminal	Sources are placed in a lumen	Oesophagus, endobronchial, biliary
Surface	Sources are placed over the tissue to be treated	Hard palate, skin, ocular

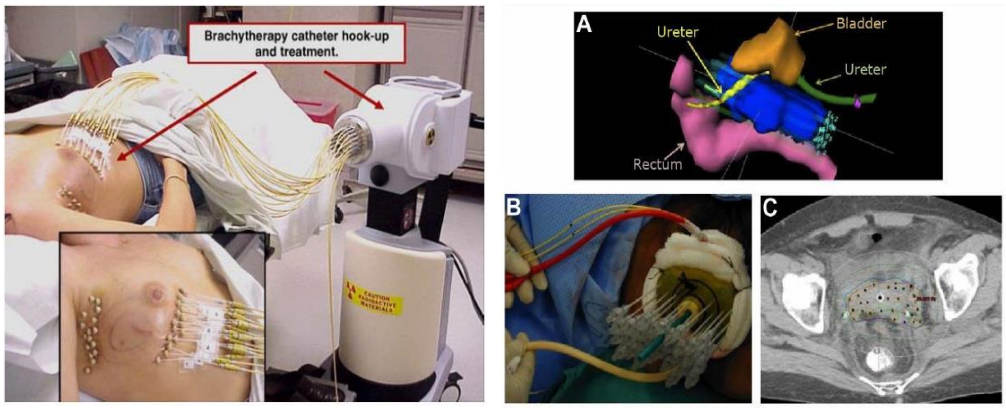

Figure 2-2 (a) Intracavity[14] and (b) interstitial[13] brachytherapy techniques.

2.1.3.2.2 Brachytherapy dose rates

Dose calculation in brachytherapy is based on the number of implants and their radioactivity, the location of each source with respect to dose calculation point, the type of isotope being used, and the energy filtration by encapsulation. Brachytherapy can be categorized in two classes of high and low dose rate regimen. High dose rate (HDR) brachytherapy is the rapid delivering of the radiation dose, typically at rates higher than 12 Gy/h, which is similar to the dose rate delivery of conventional EBRT using linear accelerators. The basic benefits of HDR brachytherapy include patient convenience and avoidance of radiation exposure for medical personnel thanks to computer-assisted remote afterloading techniques. In afterloading, the applicator is placed first into the target position and the radioactive sources are loaded later usually by an automatic robotic machine that is remotely controlled. HDR brachytherapy is commonly used for breast, prostate, gynecologic, and head and neck cancers.

On the other hand, low dose rate (LDR) brachytherapy is referred to radiation dose rates less than 2 Gy/h. It should be mentioned that the dose rates in the range of 2-12 Gy/h are defined as medium dose rate (MDR), which are not in common use due to poor treatment

outcomes. LDR brachytherapy may involve manual afterloading of brachytherapy catheters/devices or the surgical placement of sealed radiation sources (called brachytherapy seeds) directly in or near the volume being treated. These surgically implanted seeds uses very low-energy radioisotopes that do not exert hospitalization of the patient, as there is no radiation coming out of the body. The radioisotopes in permanently placed seeds decay completely and eventually become ineffective after a certain time depending on their half-life (usually several months). LDR brachytherapy is mostly used for prostate and cervix cancers.

2.1.3.2.3 Brachytherapy radioisotopes

The specific radioisotope used for each brachytherapy is based on several physical variables of the radioisotope including half-life (the time required for a radioactive isotope to lose half of its initial activity), half-value layer (HVL, the thickness of a specified substance that reduces the exposure rate of a radiation source after being imposed to the radiation path), specific activity, source energy, as well as the patient safety[15]. The common radioisotopes used as radiation sources in brachytherapy consist of ^{60}Co, ^{137}Cs, ^{192}Ir, ^{125}I, ^{103}Pd, ^{90}Sr/^{90}Y, ^{198}Au, ^{106}Ru and ^{252}Cf (Table 2-2), among which ^{125}I (Iodine-125) and ^{103}Pd (palladium-103) have been the most popular radioisotopes for permanent interstitial brachytherapy due to emitting low-energy photons[16]. ^{125}I has a half-life of 60 days, and emits photons with energy of 27 KeV, which results in a relatively low initial dose rate of 7-10 cGy/h at typical prescribed doses. ^{125}I was previously the most common radioisotope used for permanent prostate brachytherapy.

In 1986, ^{103}Pd was introduced as an alternative radioisotope being suitable for permanent interstitial implantation, and since then has gained increasing popularity. Similar to ^{125}I, ^{103}Pd emits a low-energy photon with an average energy of 21 KeV. However, it has some potential advantages over ^{125}I, including shorter half-life (17 days), higher initial dose rate (20-24 cGy/h, which is three times greater than that of ^{125}I), and increased dose heterogeneity within the target volume[17]. ^{103}Pd seeds deliver 90% of their dose in 56 days as opposed to 197 days

for ^{125}I implants. Furthermore, the shorter half-life allows for easier personnel protection and radiation safety[18]. ^{103}Pd is produced in nuclear reactors when stable ^{102}Pd isotope absorbs a neutron. ^{103}Pd decays through electron capture (EC) and produces ^{103}Ru. Certain radioactive atoms decay through EC or internal conversion (IC), which consequently form a vacancy in their atomic shells (most commonly in the K shell). Such vacancies are rapidly filled by electrons dropping in from higher shells. This process leads to a cascade of atomic electron transitions that move the vacancy toward the outermost shell. Each inner-shell electron transition results in the emission of a characteristic X-ray photon or an Auger electron[19], which are used for killing cancer cells.

Table 2-2 Properties of common brachytherapy radioactive sources

Element	**Radioisotope**	**E* (MeV)**	**T1/2****	**Source form**	**Clinical application**
Iridium	^{192}Ir	0.379	73.8 d	Wires, ribbons	LDR/HDR
Iodine	^{125}I	0.028	59.6 d	Seeds	Perm. Imp.
Cesium	^{131}Cs	0.030	9.69 d	Seeds	LDR Perm. Imp.
Cesium	^{137}Cs	0.662	30 y	Tubes, needles	LDR ICA & interstitial
Cobalt	^{60}Co	1.25	5.26 y	Sphere	HDR ICA
Palladium	^{103}Pd	0.020	17 d	Seeds	Perm. Imp.
Gold	^{198}Au	0.412	2.7 d	Seeds	Perm. Imp.
Californium	^{252}Cf	2.4 n	2.65 d	Tubes	LDR ICA
Ruthenium	^{106}Ru	3.54***	1.02 y	Plaque	LDR
Yttrium	^{90}Y/^{90}Sr	2.24 b	28.9 y	Plaque	Ocular
Ytterbium	^{169}Yb	0.093	32 d	Seeds	LDR interstitial

* Average photon energy (x/γ-rays), ** Half-life, *** β particles

2.1.3.2.4 Brachytherapy of prostate cancer

Prostate cancer is the most common type of cancer in men, which alone accounts for every 1 in 5 new diagnoses (21% of all diagnosed male cancers, estimated by the American Cancer Society for the United States in 2016). It is also the second most common cause of cancer death among men, consisting 8% of all male cancer deaths[1]. Brachytherapy is an increasingly popular treatment modality for prostate cancer, among both patients and oncologists, because of the treatment convenience and the perception of minimal long-term morbidity[16]. The radiobiological properties of prostate cancer cells demonstrate a low alpha/beta ratio; this suggests that hypofractionation (the delivery of larger radiation doses in a smaller number of treatment cycles) may offer the best chance of long term disease control for localized prostate cancer. Both permanent and temporary brachytherapy have been used to treat prostate cancer[20]. Permanent implant brachytherapy involves the permanent placement of sealed radioactive sources (seeds) within the interstitial space of the prostate gland. HDR brachytherapy, by comparison, involves the temporary implantation of hollow catheters into the prostate through which a highly radioactive source is remotely passed for a relatively short time, wherein the transit time of the source within the catheters determines the magnitude of the delivered dose[21]. Today, most treatment centers use permanent implants[22].

Although over the past few decades the percent of diagnosed cases of prostate cancer has increased, the related death rate has comparatively dropped. This declining mortality has been attributed to the public awareness along with earlier detection and treatment. In general, permanent brachytherapy is considered as a monotherapy for patients with low-risk prostate cancers (early stages). It has been reported that for intermediate-risk prostate cancers the combination of brachytherapy with EBRT (40-50 Gy) can be an effective treatment method. The intent of this combination is to treat periprostatic tissues, which may be beyond the reach of an implant alone[16]. It should be noted that low- or intermediate-risk diseases are approximately 70% of the diagnosed prostate cancers[23]. Although brachytherapy is not the primary choice of

the treatment for high-risk prostate cancers, it can still effectively incorporated as a therapy component to selected patients who are additionally treated with EBRT and androgen deprivation therapy (ADT, hormone therapy for prostate cancer). Patients with very large or very small prostates, symptoms of bladder outlet obstruction, or a previous transurethral resection of the prostate (TURP) are not suitable candidates for brachytherapy, as implantation may be more difficult for these patients, and they have an increased risk for side effects[22].

Recent studies has shown that EBRT causes more side effects and cost than prostatectomy and brachytherapy. EBRT treatment course can take 8 to 9 weeks, where up to 50% of patients have some temporary bladder or bowel symptoms during the treatment. Also, it is associated with a low yet definite risk for protracted rectal symptoms from radiation proctitis, and the increased risk for erectile dysfunction over time[22]. On the contrary, brachytherapy treatment is completed in 1 day with less time lost from normal activities, and it does not have the problems inherent in EBRT of dealing with variability in daily prostate position or reproducibility of setup over the course of treatment[24]. In appropriate patients, the control rates of cancer appear comparable to surgery (> 90%) for low-risk tumors. However, brachytherapy possess some disadvantages, including the requirement for general anesthesia and the risk for acute urinary retention. Frequently, irritative voiding symptoms may persist for as long as 1 year after implantation. Hence, brachytherapy moderately alters patients' quality of life, mainly by urinary urgency and significant pain increased after the therapy[25]. Although the cancer control by brachytherapy for localized prostate cancers has been comparable to that achieved by surgery (radical prostatectomy) and EBRT (IMRT), the claim of its better post-treatment quality of life is still debated. While principally survival is the chief goal of the treatment for prostate cancer, the nature of this malignancy compels clinical attention to the quality of the patient's life after treatment[26]. For example, as prostate is in close proximity to the neurovascular pedicles and other structures, which are related to penile erectile function, sexual potency can be affected by prostate cancer therapy[27]. Current brachytherapy techniques attempt to improve the

radioactive seed placement and radiation dose distribution[22] in order to enhance simultaneously the effectiveness of the treatment and the patient's quality of life.

2.1.3.2.5 Brachytherapy using nanotechnology

Radiosensitizers are materials in the form of chemical compounds or nanoparticles of high atomic number (Z) that can enhance the radiation effect to kill cancer cells[28]. They are commonly used in EBRT as a way to decrease the total dose which in turn would result in less damage to normal cells while achieving the same cancer control. Application of radiosensitizers to enhance radiation dose during brachytherapy were not primarily investigated, mainly due to its more localized nature than EBRT. However, several recent theoretical and in vitro studies have shown the enhancement of brachytherapy using high-Z nanoparticles such as gold nanoparticles (AuNPs). The dose enhancement by high-Z materials are based on photo-electric phenomenon, which is more dominant for photon energies in kilovoltage (kV) range (the mechanisms of dose enhancement will be discussed with more details in later sections). Interestingly, the common radiation sources utilized in interstitial brachytherapy (such as ^{125}I, ^{103}Pd, and ^{137}Cs) emit photons with kV energy. Thus, in comparison to EBRT with common megavoltage (MV) energy range, brachytherapy can potentially benefit more from radiosensitization by heavy elements. Amato et al. performed a Monte Carlo simulation study to compare the dose enhancement during EBRT and brachytherapy in tissues containing different concentrations of AuNPs. The obtained results indicated that radiosensitizing effects of AuNPs in brachytherapy were more pronounced than in external radiotherapy [29]. Another Monte Carlo simulation study on the dose enhancement effect of AuNPs for common photon-emitting brachytherapy radioisotopes (^{125}I, ^{169}Yb, ^{103}Pd, and ^{192}Ir) indicated that large AuNPs (diameter 100-200 nm) had higher dose enhancement effects[30].

Ngwa et al. conducted the first experimental (in vitro) study on the radiosensitization effect of AuNPs during continuous LDR gamma irradiation with low-energy brachytherapy

sources (^{125}I seeds). It was shown that the presence of 0.2 mg/ml concentration of AuNPs in HeLa cells could increase the biological effect of irradiation by 70-130% in comparison to that in the absence of AuNPs [31]. In another systemic study, Bi_2S_3 nanoparticles were embedded into biocompatibale poly(lactic-co-glycolic acid) (PLGA) to develop hybrid multifunctional capsules for ultrasound-guided brachytherapy of prostate cancer[32]. Bismuth (Bi) has a high atomic number of 83 (> Z_{Au} of 79), which gives it strong photoelectric absorption coefficient. The in vitro assessments on PC3 cells (human prostate carcinomas) along with in vivo investigations of nude mice prostate carcinomas xenograft revealed that the fabricated hybrid capsules of Bi_2S_3-PLGA could be used as both contrast agents (for ultrasound) and radiosensitizers for brachytherapy using ^{32}P (phosphorous-32) radioisotope.

A brachytherapy spacer is an encapsulater in form of generally cylindrical or elongated shape with interior regions to retain therapeutic loads, such as radiation sources, pharmaceutical therapeutic loads, and any other substances to treat a patient, such as drug liquids, powders or particles (micro or nano-size)[33]. It is implanted to control the spatial distribution and accuracy of radiation to the prostate[34]. It has been proposed that these brachytherapy spacers could be used for in situ delivering of radiosensitizers or cytotoxic drugs during radiotherapy. One suggested strategy to achieve this has been to coat brachytherapy spacers with biodegradable polymers that can release the bioactive drugs slowly in vivo[35]. Sinha et al.[36] conducted a modeling study to investigate the intratumor biodistribution and corresponding dose enhancement of AuNPs over time released from brachytherapy spacers coated with polymer films containing AuNPs. The results showed that the dose enhancement to tumor can be customized via the size of AuNPs and the type of applied radioisotope. Another approach has been to make biodegradable brachytherapy spacers which are loaded with chemo-radiation agents (drugs that can participate in both chemotherapy and radiosensitization process). Accordingly, Kumar et al. fabricated brachytherapy spacers using biocompatible polymer (poly(lactic-co-glycolic) acid (PLGA)) as the main matrix, and then loaded that

backbone with silica nanoparticles containing docetaxel (as therapeutic drug) and Cy7.5 fluorophore (for in vivo visualization). These fabricated brachytherapy spacers then were implanted in tumors in mice. The in vivo results showed the potential of this strategy for local delivery of radiosensitizers to combine brachytherapy with chemo-radiation therapy[34].

It has been claimed that a soluble precipitable reagent can be used as a nanoscale carrier of radionuclides within solid tumors for brachytherapy. This approach has been called "targeted molecular brachytherapy" or alternatively "selectively targeted amplified radiotherapy"[37]. In this method, a soluble reagent containing a cancer-targeting agent, an enzyme-binding moiety, and therapeutic radionuclides is administered through multiple steps, which subsequently form insoluble precipitates in cancerous cells by chemical conversion. Through this process, most of the radiation sources are localized and immobilized in the tumor by nano-precipitates, while the remaining soluble radiochemical is cleared from the body.

A group of researchers, in two parallel studies in 2010[38] and 2012[39], has reported the use of molecularly targeted radioactive ^{198}AuNPs for brachytherapy of prostate cancer in mice bearing human prostate tumors. ^{198}Au is the radioisotope of gold with 2.7 day half-life and emits β particles with maximum energy of 0.96 MeV, which can have a penetration range of 11 mm in biological tissues (roughly equals to 1100 cells diameter). Intratumoral administration of a single dose of gum arabic glycoprotein functionalized radioactive AuNPs (GA-^{198}AuNPs) to mice bearing human prostate tumor xenografts resulted in significant tumor regression and growth control over the 30-days study period[38]. At the end of the 3-week period, 19% of the initially administrated ^{198}Au still remained in the tumor. In the other study, epigallocatechin-gallate (EGCg) was used as both reducing agent to produce ^{198}AuNPs from H^{198}AuCl4 aqueous solution, and the functionalization group for surface conjugation of radioactive AuNPs[39]. EGCg is able to target Laminin receptor (Lam 67R), which is over expressed on human prostate cancer cells. Pharmacokinetic studies in PC-3 xenograft SCID mice showed almost 72% of ^{198}AuNP-EGCg retained in tumors 24 hours after intratumoral administration, while the

therapeutic studies demonstrated 80% reduction of tumor volumes after 28 days compared to control groups.

In addition to prostate cancer, nanotechnology has been exploited to treat other types of cancer by brachytherapy. Khan et al.[40] reported the use of intratumorally administered ^{198}Au dendrimer nanocomposite (d = 29 nm) in the treatment of a mouse melanoma (skin cancer) model. In a recent study, Yook et al.[41] described the use of intratumorally injected AuNPs labeled with β–emitting ^{177}Lu radioisotopes for treatment of locally advanced breast cancer. 30-nm PEGylated AuNPs were linked to DOTA and panitumumab for complexing ^{177}Lu and targeting epidermal growth factor receptors, respectively. The subsequent in vivo study using mice with MDA-MB-468 (human breast cancer) xenograft tumors indicated that both targeted and non-targeted ^{177}Lu-radiolabeled AuNPs were significantly effective to extend the survival of the treated mice.

Comparatively, functionalized ^{177}Lu-radiolabeled nanomaterials have also been studied for brachytherapy of brain tumor in a murine orthotopic xenograft model[42]. It is known that brain has a complex blood vessel structure, blood-brain barrier (BBB), which allows only the entry of essential nutrients while blocking other substances. This makes the systemic administration of therapeutic drugs for brain cancers inefficient. Convection-enhanced delivery (CED) is a local drug delivery method that bypasses BBB and enables transfer of large molecules and nanoparticles. CED includes continuous injection of therapeutic agents through one to several catheters placed stereotactically within the tumor mass, around the tumor, or the resection cavity[43]. The in vivo experiments on tumor brain (U87MG) brachytherapy using the functionalized ^{177}Lu-radiolabeled metallofullerene nanoparticles (^{177}Lu-DOTA-f-$Gd_3N@C_{80}$) delivered by CED showed that they could be used as theranostic agents for MRI imaging and increasing the survival of the treated animals. Similar results have been reported for brachytherapy of glioblastoma brain tumor (GBM) in an orthotopic U87 glioma rat model using CED-administrated ^{186}Re-radiolabled liposomes[44].

2.1.3.3 Systemic radiation therapy (Radiopharmaceutical)

Radiopharmaceuticals are basically drugs containing radioactive substances, like radiolabeled-antibodies which are monoclonal antibodies with radioactive particles attached. These antibodies are designed to attach themselves directly to specific cancer cells and damage them with small amounts of radiation. Radiopharmaceuticals are an effective and appropriate option for patients with widespread metastatic disease, particularly if they are no longer candidates for effective chemotherapy. In addition, certain cancers are treated by swallowing radioactive pills or receiving radioactive fluids intravenously, wherein the medicine goes to the entire body (systemic radiotherapy). One notable example is the radioactive iodine (radioiodine, ^{131}I) capsule that is used to treat some types of thyroid cancer, or after thyroid surgery to destroy any thyroid cancer cells left behind. Since thyroid naturally absorbs almost all iodine from body fluids, the administrated radioactive iodine would concentrate mostly inside the thyroid, with minimized systemic radiation damage.

Another example is the use of intravenous radioactive material to treat bone pain due to the spread of a cancer to the bone. Approximately 65% of patients with prostate or breast cancer and 35% of those with advanced lung, thyroid, and kidney cancers will have symptomatic skeletal metastases. In general oncological practice, breast and prostate cancers are responsible for more than 80% of cases with bone metastases[45]. Because many patients have multifocal bone pain, which can significantly decrease the patient quality of life, systemic targeted treatment of skeletal metastases provides the potential of pain relief with minimal side effects. Radiopharmaceuticals developed for the treatment of painful bone metastases (most commonly used for prostate cancer) include strontium-89 (^{89}Sr) and Samarium-153 (^{153}Sm) radioisotopes. On the contrary, these drugs can also lower blood cell counts, especially white blood cells and platelets (increasing the risk of infection, bruising, and bleeding).

2.1.3.4 Radiotherapy of breast cancer

Radiotherapy has an important role in treating all stages of breast cancer. It is a common treatment used after breast conserving surgery (cancer removed) or mastectomy (the whole breast removed). The reason to give radiotherapy after surgery is to reduce the risk of the cancer returning in the breast area (either breast tissue or nearby lymph nodes). It has also been reported that postoperative loco-regional radiotherapy improves survival in patients [46]. This adjuvant radiotherapy is particularly imperative to lower the chance of local reoccurrence of cancer in breast or near lymph nodes after breast conserving surgery with the involvements of positive margins of the resection [47]. Radiotherapy also is recommended after mastectomy for patients with high risk of reoccurrence, whose cancer has invaded either the lymph channels and blood vessels of breast or the skin. Usually after breast conserving surgery (lumpectomy or wide local excision) women are given radiotherapy to the whole of the remaining breast tissue, being called whole breast radiotherapy. In some trials, on the other hand, radiotherapy are given just to the area where the breast cancer was removed using IMRT. Other trials can involve giving different doses of radiation to particular areas of the breast.

EBRT is the most common type of radiation therapy for women with breast cancer. However, the external beam cannot discriminate between cancerous and normal cells. It also should be noted that cancer cells are usually more resistant to radiation than normal cells [48]. Thus, the required therapeutic dose is typically higher than the tolerance of the surrounding healthy tissues, which consequently might result in undesired adverse side effects, as have been routinely observed in the radiotherapy of different types of cancer. For women who had breast conserving surgery, brachytherapy can be used along with EBRT as a way to add an extra boost of radiation to the tumor site. This is more common for patients with close, positive or unknown margins, younger patients, and patients with deep tumor in a large breast. It may also be used as a sole modality instead of radiation to the whole breast[12], which is particularly a choice for patients who are not available for a 5-6 weeks EBRT treatment.

2.2 Gold nanoparticles in cancer diagnosis and treatment

2.2.1 Physical and biological properties of AuNPs

Biomedical applications of AuNPs originate mostly from their surface plasmon resonance (SPR) effect, a strong enhancement of absorption and scattering of light in resonant with the SPR frequency. This effect has been utilized for several applications such as surface enhanced Raman scattering (SERS)[49-51] , biomedical imaging contrast enhancement agents [52-55] and photothermal therapy[56-58].

SPR is a nanoscale effect of the interaction between the electromagnetic wave and the conduction electrons in a metal. When a metal is under the irradiation of light, the electromagnetic field drives the conduction electrons to oscillate. The collective motion of electrons has its own resonance frequency, plasma frequency, and the quantized plasma oscillations are called plasmons. For a nanoparticle which has the size much smaller than the wavelength of the light, this collective excitation mode of the plasma will be localized near the surface, and the resonance frequency will shift from the plasma frequency to surface plasmon resonance frequency. For some novel metals such as Au, Ag and Cu nanoparticles, the SPR peaks are located in the visible region [59].

The plasmonic properties of AuNPs are strongly dependent on their size and shape. Spherical AuNPs with 40-100 nm in diameter have SPR peaks at around 530-560 nm, while those with larger diameter (140 nm) are red-shifted to 650 nm. The SPR peak of AuNRs would split into two modes due to different orientations of the rod with respect to the electric field of incident light. A SPR peak around 530 nm corresponds to the transverse plasmon oscillation, and a stronger SPR peak at near-infrared (NIR) region arising from the plasmon oscillation along the longitudinal axis of the nanorod [60]. The SPR peaks of Au nanoshells could be conveniently tuned by controlling the ratio of shell thickness to particle diameter [61]. For Au nanocages, because the dimension and wall thickness are well controlled by the molar ratio of

Ag to $HAuCl_4$, their SPR peaks can be shifted to cover a spectral region from 400 nm to 1200 nm.

For *in vivo* biomedical applications, it required deeper penetration of near infrared (NIR) light. The reason is because the primary absorbers in tissue are water and blood (hemoglobin and oxyhemoglobin), and both are slightly ”transparent” in the NIR range [62]. Therefore, by designing AuNPs with SPR peaks in this NIR region, the NIR light is preferentially scattered and absorbed by AuNPs and will not be attenuated by the tissue.

2.2.2 Synthesis methods and different types of AuNPs

Since the introduction of colloidal AuNPs in 1857, several methods have been developed to synthesize AuNPs with different shapes and sizes (Figure 2-3), such as spherical AuNPs [63], Au nanorods [64], Au nanoshells [65], Au nanocages [66] and hollow AuNPs [67]. Among the conventional synthesis methods of spherical AuNPs by the reduction of Au^{3+} ions, the most popular one has been using citrate to reduce gold chloroaurate ($HAuCl_4$) in water, which was introduced by Turkevitch in 1951 [63].

Au nanorods, as one of the most primary anisotropic forms of AuNPs, have been the focus of numerous studies on the synthesis and application of AuNPs in recent years. Au nanorods are particularly appealing since their plasmonic properties can be tuned by changing their aspect ratio. Although several methods have been developed to synthesis Au nanorods, the solution-based methods have been more common and reliable. Accordingly, a number of groups have reported using spherical AuNPs as seeds to facilitate the formation of monodispersed Au nanorods, in which different reducing agents, such as hydroxylamine (NH_2OH), sodium citrate ($C_6H_5Na_3O_7$), and ascorbic acid ($C_6H_8O_6$), were employed. A systematic study on the synthesis of Au nanorods has been reported by Murphy et al. [64].

Another newly invented AuNPs with great potential biomedical applications are Au nanocages. The synthesis of Au nanocages were developed by Xia et al. [66]. In a typical

synthesis method, silver nanocubes suspended in solution were oxidized and replaced by $HAuCl_4$ according to a galvanic replacement reaction. Au nanoshells were first engineered by Halas et al. [65] with directly depositing Au onto silica colloidal spheres. The thickness of shell is controlled by the relative amounts of silica core and the gold salt solutions. A continuous Au shell generally has a thickness between 5 nm and 30 nm.

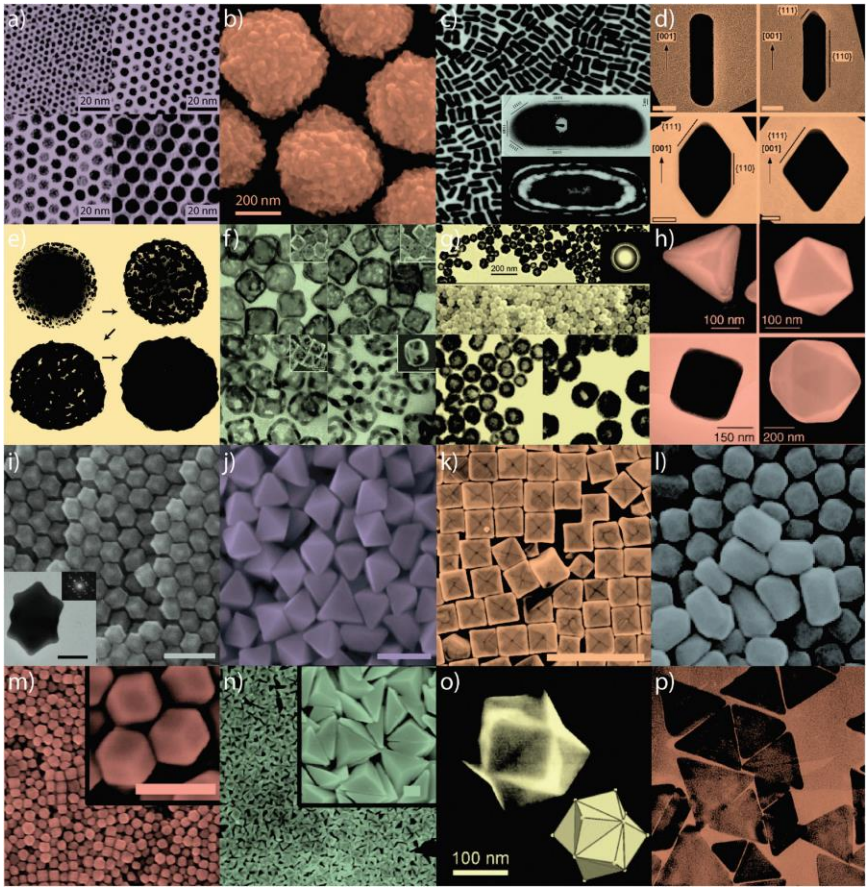

Figure 2-3 AuNPs with various size and morphologies with potential biomedical applications. Adapted with permission from [68].

2.2.3 AuNPs as diagnostic agents

Researchers have been seeking to improve the resolution of the conventional imaging techniques and developing new imaging modalities [69]. The performance of these platforms could be increased through integration appropriate contrast enhancement agents such as AuNPs. Studies on optical coherence tomography (OCT) [70], surface-enhanced Raman scattering (SERS) [49-51], photothermal imaging, photoacoustic imaging (PA), dark-field imaging, differential interference contrast (DIC) imaging [71], two-photon luminescence imaging (TPL), and computed tomography imaging (CT) [72-74] using AuNPs as contrast agents have shown promising results for diagnostic purposes [75-78]. The ability to manipulate size, shape, and surface function of AuNPs as well as tuning their plasmonic properties has made it possible to prepare suitable agents for each specific imaging method. Among different biomedical imaging methods, OCT, PA, and CT imaging have been the subject of more studies on using AuNPs as contrast agents. Nevertheless, some issues are still facing to broad application of AuNPs as contrast agents, such as efficient targeting, body clearance, and toxicity, to name a few. Since AuNPs can also be used for therapy, recent studies have increasingly focused on developing theranostic (therapy plus diagnostic) agents using AuNPs. Hence, expanding the biomedical imaging techniques using AuNPs as contrast agents has become even more crucial, as it can increase their therapeutic efficacy and widen their clinical applications [79].

Making multifunctional contrast agents has recently attracted a lot of attentions. Any given imaging contrast agent can only be useful in particular respects. Combining two or more imaging modalities using one single contrast agent may compensate its weakness with the strength of another. For example, MRI is a very powerful biomedical imaging modality in terms of image resolution. In MRI, contrast agents are generally introduced to enhance the tissue contrast. Complexes of Gd(III) in liposome or micelles are widely used as MRI contrast agents [80]. However, these systems suffer from drawbacks such as Gd(III) ion exchange with metals (e.g., Zn, Cu), and uptake of complexes in extravascular space. Recently, integrating

superparamagnetic iron oxide nanoparticles with AuNPs to form a composite multifunctional nanoparticles as contrast agents for both MRI and SERS imaging. For MRI to acquire high resolution image, the high dosages of iron oxide nanoparticles are usually required to obtain useful image contrast. SERS provides a very high sensitivity and the capability to identify single molecules. A combination of MRI and SERS could form a multimodal imaging with high resolution and multiplexed sensitivity.

2.2.4 AuNPs as therapeutic agents

AuNPs have also been explored as therapeutic agents to treat cancer. Utilizing their SPR effect, a strong enhancement of absorption of light in resonant with the SPR frequency in which the energy of light is converted into heat, AuNPs can be used as photothermal therapy agents. On the other side, due to a high atomic number (Z = 79) and biocompatibility, AuNPs have been suggested and investigated as novel radiosensitizing agents for radiation therapy.

2.2.4.1 Photothermal therapy using AuNPs

Since cancerous cells are generally more sensitive on heat damage than normal cells [81], heat induced cell death has been used as a noninvasive cancer treatment method. Several kinds of AuNPs have been demonstrated that they can be used as photothermal therapy agents, including spherical AuNPs, Au nanorods, Au nanocages, Au nanoshells and hollow AuNPs. All of them have shown their capability to generate localized heat to induce cancer cell death limited in the nearby area of the nanoparticles, while minimizing the damage to the surrounding healthy tissues.

AuNPs absorb electromagnetic radiation strongly around their SPR frequency [82, 83]. A consequence of the strong absorption of radiation associated with the SPR is heat generation. Three sequential processes are involved in heat generating [84]. First, electrons on the nanoparticles oscillate under the influence of the incident electromagnetic field. Second, the

photon energy is transferred to the electrons by inter-band transition. During this process, the internal electron energy redistribution by electron-electron scattering; the free carrier is easily heated up to thousands of Kelvin, while keeping the metal lattice temperature relatively low since its heat capacity is one to two orders of magnitude larger than the electron one. This strong electron temperature rise induces the modification of their Fermi-Dirac distribution and consequently creates the hot electron. In the relaxation process of electrons, the energy is transferred to the lattice via electron-phonon interaction. Finally, through phonon-phonon interactions, the heat from AuNPs is dissipated into vicinity leading the death of the cancer cells. Several works have been demonstrated that AuNPs can be used as heat generating agents to ablate the cancer cells [56, 83, 85-87]. However, for *in vivo* biomedical applications, there exists a principle problem; tissues scatter and absorb light in the visible region, and even NIR light can only penetrate several millimeter into the tissue. Due to this limitation, AuNPs with the SPR peaks in the NIR region are required for this application [62].

Spherical AuNPs have the SPR peak located at approximately 530 nm where chromaphores also have high absorbance at this wavelength [62]. Such overlapping greatly decreases the efficiency of induced heat to tumor sites. However, the red-shifted SPR peak can be achieved with aggregated spherical AuNPs. As the nanoparticles are accumulated on the cancer cells, the absorption peak can shift from 530 nm to as far as 1000 nm [88]. This ensures the NIR light can easily penetrate the tissue and the majority of light is absorbed by AuNPs, thereby heating the cancer cells. Unfortunately, the red shift is dependent on the concentration of the Au bound to each cell and may not be reproducible or controllable.

Unlike spherical AuNPs, the SPR peaks of Au nanorods, Au nanoshells and Au nanocages can be tuned to strongly absorb NIR by controlling the aspect ratios, shell thickness and porosity of the shells, respectively[65, 66, 89]. Nanoparticles with SPR peaks in the NIR region are accumulated at the tumor site. The SPR peak is in the NIR region where tissue absorption is minimal, permitting optimal penetration [62]. When the tumor site is exposed to NIR radiation,

the nanoparticles absorb intensely because of SPR effect, and then the absorbed energy is efficiently converted into heat leading to thermal destruction of the tumor.

El-Sayed et al. [90] have demonstrated that Au nanorods can be used as heat-generating agents for *in vivo* photothermal therapy. In their study, the PEGylated Au nanorods were conjugated to anti-EGFR antibodies enabling selective photothermal therapy due to their preferential binding onto human oral cancer cells. A NIR laser with a wavelength of 800 nm, overlapping with the SPR absorption maximum of the Au nanorods (aspect ratio of 3.9) was used for the photothermal ablation of cancer cells which binding to the Au nanorods. More recently, Bhatia et al. [91] further demonstrated the therapeutic efficiency of Au nanorods *in vivo*. They found that PEGylated Au nanorods accumulated at tumor sites in mouse models after a single intravenous injection, and indicated that a four-dimensional computational modeling supported by the biodistribution data derived via X-ray computed tomography imaging of Au nanorods could be used to predict photothermal heating during irradiation. This integrated method was shown to be effective for destructing all irradiated human xenografts tumors in mice.

Multiple *in vivo* studies have also demonstrated the efficiency of Au nanoshells for the non-invasive treatment of tumors through targeted photothermal ablation [92, 93]. O'Neal et al. have successfully treated mice inoculated with tumors using this technique [92]. In their experiments, mice were inoculated subcutaneously with colon cancer cells and PEGylated Au nanoshells solution was injected into mice via a tail vein. After certain time, Au nanoshells were accumulated on the tumor sites and was irradiated with 808nm light. The results show a complete destruction of tumors and all mice were healthy and free of tumors up to 90 days after the photothermal treatment.

Chen et al. used a BR-3 breast tumor mouse model to examine the efficacy of Au nanocages on the photothermal cancer treatment in vivo[94]. Tumor-bearing mice were administrated intravenously with PEGylated Au nanocages for passive targeting. After 72h post-

injection, the tumor on the right flank of each mouse was irradiated with an 808 nm diode laser for 10 minutes. The treatment response was evaluated using [^{18}F] fluorodeoxyglucose (^{18}F-FDG) positron emission tomography (PET) to monitor the changes in metabolic activity before and after photothermal therapy. The results have shown for mice injected with Au nanocages, there was a significant reduction in FDG uptake for tumor on the right flank at 24 h post-treatment compared with no treatment group. In contrast, the tumor on the left flank without laser treatment showed no significant difference for the FDG uptake at 0 and 24 h. After normalizing the signal of the right tumor to that of the left tumor, the values indicated a decrease in metabolic activity by around 70%.

2.2.4.2 Radiotherapy using AuNPs

2.2.4.2.1 Radiosensitization concept

Radiotherapy is one of the most common clinical treatment methods of cancer, in which an ionizing radiation is used to kill cancer cells by damaging their DNA. However, since high dose of radiation is required for effective treatment, severe adverse side effects are usually associated with radiotherapy. Thus, new ways of delivering radiation therapy to make it safer and more effective have been sought. Two applied methods have been radioprotection (decreasing the effective dose to normal cells) and radiosensitization (increasing the radiosensitivity of cancer cells).

Radioprotection can be done by decreasing the fraction size and improving the dose distribution (physical radioprotection), or using radioprotector drugs. Radioprotectors are substances that protect normal cells from radiation. These types of drugs are useful in areas where it is hard not to expose vital normal tissues to radiation when treating a tumor, such as the head and neck area. However, attempts to develop drugs to chemically protect cells have been largely unsuccessful [95].

Oxygen is a radiosensitizer because it extends the existence of free radicals by a factor of 3. Cells in a hypoxic environment are relatively radioresistant. Since oxygen is required for effective radiotherapy, and since tumors almost always contain hypoxic areas, improving delivery of oxygen to tumor cells may improve clinical outcomes. Although pressurized oxygen has not been demonstrated to improve the therapeutic ratio, randomized data suggests that raising depressed hemoglobin levels enhances tumor control [95]. Thus, radiosensitizers are drugs that make cancer cells more sensitive to radiation. Some chemotherapy drugs already in use (such as 5-fluorouracil) are known to be radiosensitizers.

Another approach to achieve radiosensitization has been to use heavy (high atomic number) materials in the targeted area. High-Z elements (such as iodine (Z = 53) and gadolinium (Z = 64)) have been proposed as radiosensitizing agents to enhance radiation dose in the targeted area through higher energy absorption of X-rays and conversion to photoelectrons. Among different available high-Z materials, gold nanoparticles (AuNPs) are emerging as the most promising candidate for radiosensitization, mainly because of their high photoelectric absorption, biocompatibility, and well-established synthesis and functionalization processes. Extensive computational and in vitro studies[96-116] have demonstrated the radiosensitization effect of AuNPs.

2.2.4.2.2 Radiosensitization mechanisms by AuNPs

Owning to a high Z of 79 and consequently a high energy absorption coefficient, AuNPs can interact strongly with the radiation beam when they are irradiated, and generate different products depending on the energy of the incident beam. At the range of low energy X-rays (few keV), the predominant interaction is known as photoelectric (Figure 2-4b), in which AuNPs absorb photons and subsequently emit cascades of short-range secondary electrons (Auger and photoelectrons) and characteristic X-rays. Due to higher mass energy absorption coefficient of AuNPs in comparison to that of soft tissue, they will absorb the radiation dose during

radiotherapy and deposit it in the target volume. In soft tissues, the primary mechanism by which photons lose energy is Compton scattering (Figure 2-4b). Thereby, AuNPs not only increase the local dose, but also prevent the heterogenic distribution of radiation caused by scattering events in soft tissue.

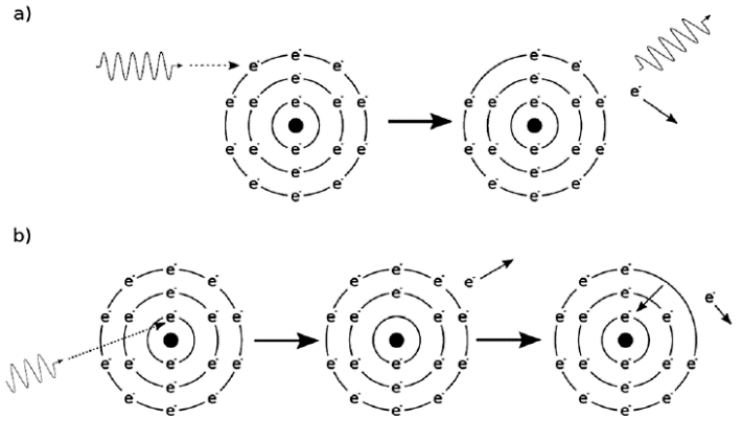

Figure 2-4 Schematic illustration of ionizations caused by (a) Compton, and (b) Photoelectric effects[117].

Several experimental investigations as well as theoretical modeling have indicated the dose enhancement effect of AuNPs [96-98, 101-113, 118, 119]. However, the observed enhancement effects have been usually higher than those were predicted based on the physical properties of AuNPs. Furthermore, it has been understood that the major radiosensitization contribution comes from kilo-voltage X-rays, while clinical linear accelerators mostly use mega-voltage X-rays. Nevertheless, it has been reported that AuNPs exhibit an unexpected significant

radiosensitization for practical megavoltage X-rays as well, which cannot be explained by simply considering the increased mass energy absorption coefficient of Au. Consequently, other enhancement mechanisms, such as increased production of reactive oxygen species due to AuNPs, have also been reported [120-122]. While this discrepancy has been mostly attributed to the biological aspects of the phenomenon, it has not been completely understood yet [117].

2.2.4.2.3 In vivo studies on AuNPs used as radiosensitization agents

In spite of plenty in vitro and theoretical studies on the X-ray radiosensitization by AuNPs, a limited number of in vivo investigations have been conducted in recent years [114, 123-129]. The pioneering in vivo experiments on the radiation enhancement using micro and nano Au particles were done by Herold and Hainfeld back in 2000 and 2004, respectively[130, 131]. Herold et al. [130] were the first group to intratumorally inject Au micro-particles (1.5 to 3 μm) into EMT-6 (murine breast cancer cells) tumors in mice, and then treat the tumors with 8 Gy irradiation of 200 kVp X-rays. Immediately after the treatment, the animals were sacrificed and their tumors were resected. Using in vivo/ in vitro assays of cell viability, it was observed that even the inhomogeneous distribution of microsize Au particles in the form of “isolated pockets” within the solid tumors were able to increase the killing of tumor cells.

The in vivo study by Hainfeld et al. [131] in 2004 on the use of small AuNPs (1.9 nm) to enhance x-rays radiation therapy in mice is generally considered as the breakthrough for the future investigations on the radiosensitization by AuNPs. In this ground-breaking study, after intravenous administration of AuNPs (up to 2.7 g Au/kg body weight) to the mice bearing subcutaneous EMT-6 breast carcinomas, the tumors were exposed to 250 kVp X-rays for several minutes. That single dose treatment caused the substantial difference among the one-year survival percent of AuNP + X-rays (86%), X-rays alone (20%), and AuNP alone (0%) mice groups, demonstrating the substantial potential of AuNPs for radiotherapy enhancement.

Radiation-induced apoptosis is a mechanism of cell death by radiation. Accordingly, Chang et al. [123] investigated the radiosensitizing effect and apoptotic response of AuNPs in combination with single dose clinical electron beams (6 MeV electrons using a linear accelerator to deliver a total dose of 25 Gy per mouse) on B16F10 melanoma tumor-bearing mice. Similar to the previous study, it was showed that the combination of AuNPs and radiation therapy hindered tumor growth and extended the survival of mice in comparison to radiation alone. It was pointed out that the accumulation of 13 nm AuNPs in endoplasmic reticulum (ER) and Golgi, rather than the nucleus of cells, could contribute to the increase of the radiation-induced apoptosis potential of cells.

Since the efficiency of radiation enhancement by AuNPs is assumed to be heavily dependent on their number and distribution within the tumor as well as their cellular uptake, which themselves are mostly regulated by size and surface coating of the AuNPs, Zhang et al. [132] decided to explore the radiosensitivity of PEG-coated AuNPs with different sizes. The mice bearing U14 tumors (cervical carcinoma) were treated with PEG-coated 4.8, 12.1, 27.3 and 46.6 nm AuNPs via intraperitoneal injection, which subsequently irradiated by 5 Gy gamma rays. It was found that 12.1 nm AuNPs had the most significant enhancement effect, while the 46.6 nm AuNPs showed the lowest enhancement, which were attributed to the highest accumulation of 12.1 nm and smallest content of 46.6 nm AuNPs in the tumors. In a similar study, Wolfe et al. [133] investigated the biodistribution and radiosensitization of gaserelin-targeted Au nanorods using megavoltage radiontherapy in mice with heterotopic prostate cancers. They demonstrated that the radiosensitization to megavoltage radiation was not observed with unconjugated Au nanorods, concluding that the radiosensitization is improved by active targeting that leads to cellular internalization of nanoparticles and the consequent increase in ionization density within the cytoplasm.

Similar to X-rays and gamma rays, when high energy charged particles collide with high-Z element nanoparticles, a variety of secondary radiation types, like Auger electrons and

characteristic x-rays, can be emitted by the inner shell ionization of the nanoparticle atoms. Thus, the therapeutic efficacy of cancer treatment by high-energy charged particles radiation, like proton therapy, can also be improved using AuNPs as dose-enhancer agents. Therefore, Kim et al. [125] investigated the treatment efficacy enhancement of 45 MeV proton beam radiation by delivering different radiation doses to the mice bearing CT26 tumors which received intravenously 100 or 300 mg kg^{-1} body weight AuNPs coated with DTPA-cysteine prior to radiation. The promotion of tumor regression at a given proton dose due to the presence of AuNPs suggested the compelling dose enhancement effect from high-Z nanoparticles for charged particle-induced therapy.

One of the hypothesized mechanisms for radiosensitization by AuNPs is their emission of secondary electrons (Auger and photoelectrons) through interactions with incident x-rays. Because those secondary electrons have inherent low energies and consequently short ranges in tissues (from few nm to less than 2 μm), it is expected that their lethal effect to kill cancer cells would be more pronounced at the close proximity to the DNA of cells. Hence, antibody-targeted AuNPs were explored in vivo to study the effect of tumor specificity and internalization by cancer cells on the radiation response [134]. Mice models bearing subcutaneous MDA-MB-361 tumors were treated with 11 Gy of 100 kVp X-rays 24 h after intratumoral injection of HER-2 targeted AuNPs (4.8 mg/g tumor). The results showed that the concurrent use of radiation and targeted AuNPs resulted in significantly slower tumor growth as compared to the mice treated with X-rays alone, which were attributed to the high enough accumulation of AuNPs in the tumor. On the other hand, Herbert et al. [135] reported no radiosensitization effect for MC7-L1 (murine mammary ductal carcinoma) tumor-bearing mice when treated with 10 Gy of 150 kVp X-rays after intravenous injection of 5 nm AuNPs, which was related to the low tumor uptake (almost 0.1 mg/g tumor) of the AuNPs. These studies revealed the importance of AuNPs concentration at the tumor site for effective radiosensitization, which is influenced by administration method and targeting strategy.

Because current brain tumor treatments are not sufficiently competent, more effective alternative treatments have been explored. Accordingly, to study the radiotherapy enhancement for brain cancer tumors, ~11 nm AuNPs were intravenously injected to mice bearing orthotopic brain gliomas and treated with 30 Gy of 100 kVp X-ray 15 h after injection [136]. The resulted long-term (>1 year) survival rate of mice treated with AuNPs plus 30 Gy radiation were found to be 50% as compared to 0% for radiation only. It was observed that AuNPs were distributed throughout the brain tumor instead of localizing primarily to the periphery of subcutaneous tumors, and the tumor to normal brain ratio of Au content were 19 to 1, which yields a calculated dose enhancement of approximately 300%. Therefore, it was shown that AuNPs had high tumor accumulation due to their ability to cross the blood tumor barriers, where on the other hand, they were largely blocked by the normal blood brain barriers, providing the specific dose enhancement at tumor site. More recently, a comparable research also reported the radiotherapy enhancement of brain tumors using AuNPs-based MRI contrast agent during micro-beam radiotherapy [129]. The MRI imaging revealed that the intravenously injected AuNPs into rats had higher density in the brain tumors due to further vasculature around the tumors and the disrupted blood brain barrier, which is in consistence with the results of the previous study. In addition, MRI was effectively used to determine the required delay between the intravenous injection of nanoparticles and irradiation to ensure the highest concentration of AuNPs in the tumor during radiotherapy. In another effort to use an imaging modality to optimize the radiation therapy, Joh et al. [127] used computed tomography (CT) to visualize the accumulation of intravenously injected AuNPs within the sarcoma tumors in mice, where AuNPs served as both CT contrast and radiosensitizing agents.

To develop ideal radiosensitizing agents, characterized by high radioenhancement potential, good tumor specificity, biocompatibility, and acceptable renal clearance, Zhang et al. recently investigated biomolecule-coated ultra-small AuNPs (sub-2 nm) and Au nanomolecules [137]. It was indicated that the ultra-small size and biocompatible coating of the AuNPs and

nanomolecules resulted in significant tumor uptake, while effectively assisted their renal clearance, providing the suitable condition for radiosensitization with very low side effects. Their subsequent in vivo studies using the developed agents to enhance radiotherapy showed promising results. Other recent studies have reported investigation of Au nanoclusters [138] and multifunctional AuNPs [139, 140] as promising radiosensitizing agents.

2.2.4.3 Hyperthermia using AuNPs

Hyperthermia is the use of heat (usually up to about 43 ^{o}C) to kill cancer cells, but when used alone it does not destroy enough cells to cure the cancer. Heat created by microwaves and ultrasound is being studied in combination with radiation and appears to improve the effect of the radiation. In other words, hyperthermia, either before or after irradiation, has been shown to radiosensitize tumor cells. This effect is not related to the presence of oxygen, indeed, cells in a hypoxic environment are more sensitive to hyperthermia and radiation. However, delivering and maintaining heat homogenously has been challenging [95]. AuNPs not only can act as radiosensitizing agents, but also they can absorb light and generate local heat, making them useful for both hyperthermia and radiotherapy.

The combination of radiation therapy with hyperthermia and AuNPs has been investigated by Hainfeld et al. [114]. It was shown that hyperthermia (heating up to 44 °C for 20 min) alone and hyperthermia plus AuNPs (without radiation) had no effect on the squamous carcinoma tumor growth in mice as compared to untreated tumors. In contrast, using 23 Gy alone, 23 Gy plus hyperthermia (for 15 min), and 23 Gy plus hyperthermia in addition to AuNPs (1.9 nm), the median tumor doubling time increased from 7.5 to 38.5 to 66 days and long-term survival similarly increased from 0% to 43% to 50%, respectively. It has been known that hyperthermia can synergize radiation therapy. One explanation is that radiation is most effective with rapidly growing cells, while hypoxic cells with poor circulation are relatively resistant to radiation. Nevertheless, heat can damage tumor blood vessels and reduce tumor blood flow,

leading to diminish hypoxia and kill the already malnourished hypoxic cells. Therefore, the combination of those two modalities with AuNPs can have dramatic synergistic effect and results in significant reduction in the required radiation dose.

In a novel approach, instead of using AuNPs to directly enhance radiation dose through photon-electron interactions, Diagaradjane et al. [124] used Au nanoshells (with 120 nm silicon core and 12-15 nm Au shell) to improve the efficacy of radiation therapy by utilizing mild-temperature hyperthermia and tumor vasculature disrupting. The mice with human colorectal cancer tumors received 8×10^8 nanoshells/g body weight intravenously followed by a localized illumination with a laser to generate a mild temperature increase in the range of 10 ± 1.5 and 8 ± 0.5 ^oC in the tumor core and base, respectively. After Au nanoshell-mediated hyperthermia, the tumors were treated with a single 10 Gy dose of radiation therapy using 125 kV X-rays, and then monitored for regrowth delay versus control groups. Their results suggested that Au nanoshell-mediated hyperthermia enhances the efficacy of radiation therapy by two mechanisms: (a) an early increase in perfusion that reduces the fraction of hypoxic cells that contribute to radiation resistance and (b) a following induction of tumor-specific localized vascular disruption and extensive necrosis that complements radiation-induced cell death.

2.2.4.4 Drug delivery using AuNPs

Nanoparticles have been shown to be capable platforms for carrying drugs to the targeted site inside the body because of their high surface area for drug loading, the functionalization ability, and enhanced pharmacokinetics and tumor accumulation (through passive and/or active targeting) [68]. Among different nanoparticles, AuNPs are distinctive due to their photothermal properties which can be used for controlled drug release. Drugs can be loaded to the surface of AuNPs or the interior of hollow Au nanostructures, such as Au nanocages. A variety of methods have been developed for loading different types of drugs onto the surface of Au nanostructures, including direct conjugation via the Au−S or Au−N bonds,

anchoring to the capping ligand, and adsorption by means of electrostatic interactions, van der Waals forces, or hydrogen bonding [141].

2.2.5 Toxicity of AuNPs

Colloidal Au has been safely used to treat rheumatoid arthritis for half a century with minimal-to-no side effects [142]. In the last two decades, many in vitro and in vivo studies have been performed to assess the toxicity of AuNPs and have yielded wildly variable results. This is potentially due to too many variations of AuNPs and experimental conditions, including synthesis method, particle size, size distribution, particle shape, surface modification, dose concentrations, and particle concentration inside cells or organs. The in vitro or in vivo toxicity observed for AuNPs is essentially the net effect influenced by interplay of different determinants. Currently the arena of AuNP cytotoxicity on cell panels is unclear as well as contradictory in some instances[79].

Particle size is an important parameter influencing cytotoxicity. Extremely small sized AuNPs (1 – 5 nm) were found to be significantly cytotoxic due to that fact that they can penetrate both the cell and nuclear membranes with more ease than the larger NPs and attach to DNA molecules, resulting in their interference with DNA architecture, or production of reactive oxygen species (ROS) leading to potential cell/tissue damage or necrosis [143-146]. Surface modification with biocompatible agents like PEG [147], poly-L-lysine [148], glutathione [149], other polymers [150, 151] and specific targeting peptides [152] may aid in decreasing the non-specific toxicity of these NPs .

Surface coating of AuNPs has also considerable effect on the resultant toxicity seen in the studied cell and animal models. Most studies have shown that AuNPs modified with nontoxic stabilizers, such as PEG, PAH, PAA, GA, are generally regarded as biocompatible [153, 154]. Meanwhile, there has been sufficient evidence that CTAB-stabilized AuNPs possesses significant cytotoxicity, potentially owing to the free CTAB in the treatment solutions[155-157]. Therefore, planning a suitable replacement of the CTAB coating on AuNPs during their design

would be beneficial in decreasing any anticipated toxicity. Along with surface coating, it has been shown that AuNPs possessing a cationic surface charge could potentially result in higher toxicity than negatively charged AuNPs, because of enhanced electrostatic binding of cationic NPs to the negatively charged cell membranes [158].

In addition to affecting cell-membrane interactions, the surface charge and chemical structures of the coating material conjugated to or stabilizing the AuNPs have been shown to modulate gene expression [145]. Thus, depending on the chemical structures of the coating materials used, in vivo kinetics and toxicity may differ to result in a variable response. Aspects such as the surface of the metal core have also been shown to affect the degree of resultant embryotoxicity, which again is possibly due to changes in vivo uptake and elimination kinetics, or specific molecular-level mechanisms associated with the physiological inertness provided by gold surface [159].

Experimental AuNP concentrations [144, 160, 161] and time-points of analysis [162] may considerably control the resultant cytotoxic effects of AuNPs. In many studies, exposure of AuNPs at higher concentrations or for extended durations has demonstrated higher toxicity. Higher incubation concentrations have demonstrated disruption of cell membrane structures, resulting in morphological abnormalities and/or cell death [152]. In addition, a concentration-dependent effect of AuNP on embryotoxicity has also been demonstrated using zebrafish embryos [145].

Finally, the biological system used for investigation has been found to have a substantial effect on the cytotoxicity. Some studies demonstrated a variation in response of different cell lines to the same AuNPs concentrations post-exposure[163, 164], suggesting that a careful selection of the biological system is needed for the correct evaluation of the expected cytotoxicity of the AuNPs.

The size and surface modification have been found to have a profound effect on the degree of in vivo bioaccumulation of the studied AuNPs. Smal AuNPs (less than ~ 50 nm) were

able to bypass the blood-brain barrier, while the larger AuNPs (≥ 50 nm) were essentially found to have lower brain concentrations, but with reasonably high accumulation in the mononuclear phagocyte system (MPS) organs such as the liver and spleen, and even in the kidneys, owing to their size being larger than the pores of glomerular capsules (5.5 nm)[165-169]. Accumulation of AuNPs in such organs could potentially result in organ toxicity and even death, hence necessitating a critical evaluation of the in vivo pharmacokinetics and toxicology of newly designed AuNPs.

Chapter 3 Hollow gold nanoparticles as efficient radiosensitizing agents for radiation therapy of breast cancer

3.1 Introduction

Breast cancer is the most common cancer and the second leading cause of cancer-related deaths in women[170]. Triple negative breast cancer (TNBC) is known to constitute 10 – 20% of breast cancer cases and occurs more frequently in younger patients and women of African American descent. TNBC tumors are heterogeneous in nature, and normally larger in size. With lymph node involvement upon diagnosis, TNBC is more aggressive and resistant to common therapeutics[171]. Due to the lack of expression of estrogen receptor (ER), progesterone receptor (PR), and human epidermal growth factor receptor 2 (HER 2), therapies targeting these biomarkers have been ineffective. Given that local recurrence of micro-metastases presents a common problem associated with TNBC, early eradication of the primary tumors is essential to patient survival[172].

In conjunction with breast conservation therapy (BCT), adjuvant radiotherapy can potentially reduce recurrences of primary tumors after surgical resection of the tumor [46, 47, 173, 174]. Despite being widely used in clinic, EBRT is limited by being non-discriminatory between normal and cancerous tissues. With cancer cells being more resistant to radiotherapy than normal tissue, significant toxicity may occur to surrounding organs before effective doses being delivered to the tumors. As discussed earlier, one method to alleviate this side effect is to introduce radiosensitizing agents composed of high-Z materials[130, 175-177] (such as AuNPs) which can enhance the absorbance of ionizing radiations in tumor tissues.

The studies on AuNPs as radiosensitizers for radiotherapy of cancer have yielded some results that are beyond the predictions of the widely-accepted physical theories[96-98, 101-113, 118, 119]. This implies the fact that the biological aspects of radiosensitization by AuNPs should also be considered along with their physical characteristics[117]. In this regard, a number of in vivo

investigations have reported the role of physicochemical properties of AuNPs in their biological effects on radiosensitization[114, 123-129]. To overcome the poor bioavailability of AuNPs in vivo, intratumoral injection of AuNPs has become an effective and practical method to alleviate the systemic toxicity associated with higher intravenous doses required to attain a similar high local concentration in the tumor microenvironment[114, 126, 130, 131, 134, 178]. Herein, the effect of a novel type of AuNPs, hollow AuNPs (HAuNPs), on the radiation response of MDA-MB-231 breast cancer cells and tumor xenografts are assessed in vitro and in vivo.

3.2 In vitro analysis

3.2.1 Cell culture

MDA-MB-231 breast cancer cell line was obtained from the American Type Culture Collection (ATCC, Manassas, VA). MDA-MB-231 cells were cultured in RPMI 1640 (Roswell Park Memorial Institute 1640) medium supplemented with 5% fetal bovine serum (FBS) at 37 ^{0}C in an atmosphere of 5% CO_2 and were passage at 75% confluence in P150 plates. The cultured MDA-MB-231 cells were harvested from monolayer using PBS pH 7.4 and trypsin/EDTA, and suspended in RPMI 1640 with 5% FBS. The number of cells per milliliter in this suspension was then counted using a hemocytometer. Finally pre-determined number of cells were plated in 35 mm dishes.

3.2.2 Synthesis and characterization of HAuNPs

Hollow gold nanoparticles (HAuNPs) were synthesized using hydrogen-bubble template synthesis method which was previously developed by our group at University of Texas at Arlington [179]. Briefly, in this method, electrochemically evolved hydrogen nanobubbles serve as templates. The high concentration of hydrogen molecules in the bubble boundary reduces the Au^+ ion to form Au clusters. Subsequently, the metal clusters act as catalysts to trigger the autocatalytic disproportionation reaction of $Na_3Au(SO_3)_2$, which leads to the formation of a gold shell around the hydrogen bubble. The metal Au gradually grows from clusters or particles to a porous network resulting in the formation of a gold shell around the hydrogen bubble. The metal Au gradually grew from clusters or particles to a porous network. Using this synthesis method, monodispersed HAuNPs (Figure 3-1) were produced with a diameter larger than 100 nm (sub-25 nm shell with a 50–70 nm hollow core).

For in vitro study, the HAuNPs were further PEGylated with mPEG-SH (MW 5kDa) by adding 20 µM mPEG-SH solution into HAuNPs suspension and stirred for overnight at room temperature. For in vivo study, HAuNPs were used without further PEGylation. As determined

by TEM (Figure 3-1), the synthesized HAuNPs had a diameter of approximately 120 nm (50 nm core/35 nm shell thickness), as shown in Figure 1a. Such HAuNPs are ideal radiosensitizers due to their larger surface area in combination with a thin gold shell.[180]

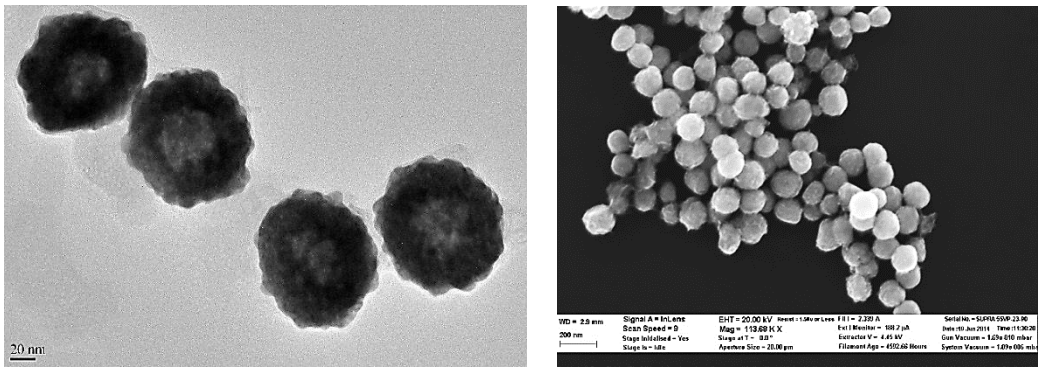

Figure 3-1 TEM and SEM images of HAuNPs.

3.2.3 X-ray irradiation of cells

A commercial X-ray device (XRAD 320, Precision X-ray, Inc.) was applied to irradiate cells. Briefly, X-ray beam of 225 kVp and 13 mA was used, which delivered a radiation dose of 3.9 Gy/Minute from a distance of 30.5 cm. A clinical Truebeam linear accelerator (Varian, Palo Alto, CA) was also used to irradiate samples. The flattening-filter-free (FFF) mode was used and 6 MV beam was delivered at a dose rate of 1400 MU/Min.

3.2.4 Clonogenic assay

Cells with pre-determined numbers (100-4000 cells) were plated for survival analysis using the clonogenic assay technique described by Puck and Marcus[181]. Culture medium was removed and replaced with HAuNPs-loaded medium 24 hours prior to irradiation. After the irradiation, cell cultures were incubated for 8 days at 37 ^{0}C in a 5% CO_2 incubator. During this period, the culture medium was replaced with fresh culture medium every 4 days. The colonies were fixed with 10% formalin and stained with crystal violet. Colonies exceeding 50 cells were scored as surviving cells. The plating efficiency and surviving fraction for a given treatment were calculated based on the survival of non-irradiated cells treated with HAuNPs alone.

3.2.5 Cytotoxicity study method

Approximately, 100 MDA-MB-231 cells were plated in 35 mm dish in culture medium supplemented with 5% FBS at 37 ^{o}C in a 5% CO_2 incubator. The HAuNPs were prepared by suspending nanoparticles in culture medium with the concentrations varying from 70 to 350 µM, which were determined by inductively coupled plasma mass spectrometry (ICP-MS, Perkin Elmer ELAN DRC II). After 24 hours, the HAuNPs suspension in culture medium was added to the dishes and incubated for 9 days. During the culture period, the culture medium was replaced with fresh culture medium every 4 days. Finally, the cytotoxicity of HAuNPs to MBA-MB 231 cells line was evaluated by clonogenic assay.

3.2.6 Uptake of HAuNPs by MDA-MB-231 cells

The localization of HAuNPs inside cultured cells was revealed by confocal microscopy (Figure 3-2) showing that the HAuNPs were clustered in the cytoplasm. No significant difference was observed between the images of different HAuNPs concentrations because the HAuNPs always clustered together inside the cells. Observation using this technique showed that HAuNPs were fully internalized after 24 hours of exposure.

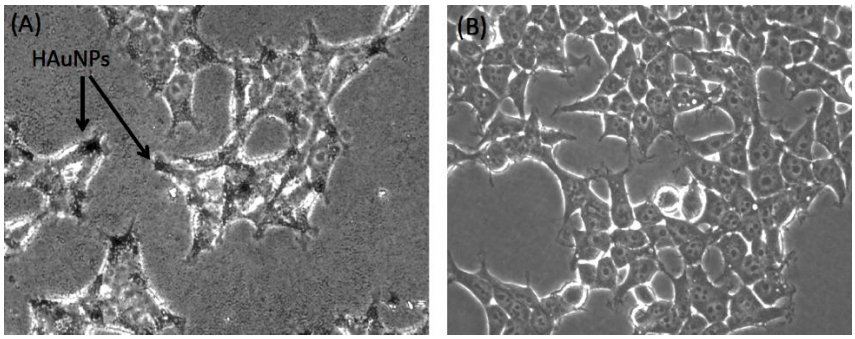

Figure 3-2 Microscopic images showing that (a) HAuNPs are internalized within the MDA-MB-231 cells after 24 hours of incubation. (b) control MDA-MB-231 without HAuNPs.

3.2.7 Evaluation of cytotoxicity of HAuNPs

The cytotoxicity studies were performed with clonogenic cell survival assay technique to determine the highest concentration of HAuNPs that can be used without causing the damage to MDA-MB-231 cells. MDA-MB-231 cells were incubated with HAuNPs for 9 days at concentrations of 70, 105, 140, 210, 280 and 350 µM (Au atomic weight). Surviving fractions were normalized to untreated control cells (0 µM Au) in each of the experiments. The numbers of colonies were counted manually as shown in Figure 3-3. The HAuNPs showed no cytotoxicity to MDA-MB-231 cells at Au concentration up to 350 µM.

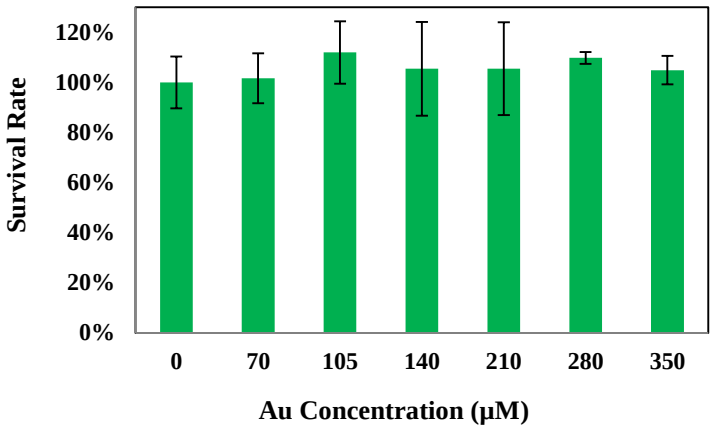

Figure 3-3 Effects of HAuNPs on clonogenic survival rate. The cytotoxicity of HAuNPs following 10 days exposure to gold concentrations of 70, 105, 140 , 210, 280 and 350 μM. Surviving fractions were normalized to untreated control cells (Au 0 μM) in each of the experiments.

Due to their small size, gold nanoparticles have been found to easily enter cells. Early studies with cytotoxicity data were focused on utilizing this property for unclear transfection and targeting. However, while the reported cytotoxicity studies of gold nanoparticles are conflicting, the cytotoxicity has been attributed to a variety of factors, including surface coating, nanoparticles charge, and size. It was found that 1.2 and 1.4 nm gold clusters had higher cytotoxicity than 15 nm nanoparticles as observed by cell necrosis and apoptosis and the cytotoxicity of surface modified gold nanoparticle seem more relevant to the particle size. Interestingly, while 18 nm gold nanoparticles were found nontoxic and the cytotoxicity was determined by surface modifier introduced, 33 nm gold nanoparticles exhibited low toxicity in different cell lines[155, 182-185]. This cytotoxicity could be related to the electrostatic absorption between the cationic nanoparticles and the negatively charged cell membranes. After modification of synthesized HAuNPs by mPEG-SH (MW 5kDa), lower cytotoxicity and higher cell uptake was observed. The PEG-coated HAuNPs are nontoxic to MDA-MB-231 cells within the gold concerntration range tested.

3.2.8 Dose enhancement in cells irradiated with x-ray

The enhancement of radiation effects by HAuNPs was measured using clonogenic cell survival assay technique. The initially plated cell number was varied with the radiation dose. Survival curves displayed in Figure 3-4 (a) show that the effects of HAuNPs on cell surviving fractions at a series of radiation doses of X-ray beams of 225 kVp energy with and without HAuNPs. Cells were incubated with 140 μM HAuNPs-loaded culture medium for 24 hours prior to the radiation. MDA-MB-231 cells treated with 140 μM HAuNPs were more sensitive to 2 Gy X-rays than control cells, increasing the therapeutic efficacy by 48%. After irradiation dosing of 4 and 6 Gy, the survival rate was decreased to 18.6 and 17.3% for cells exposed to HAuNPs, respectively. Similar trends were observed for MDA-MB-231 irradiated by a linear accelerator. HAuNPs enhanced the death rate of cells when irradiated with 6 MeV (Figure 3-4 (b)). The survival rate decreased by 60% in the presence of HAuNPs.

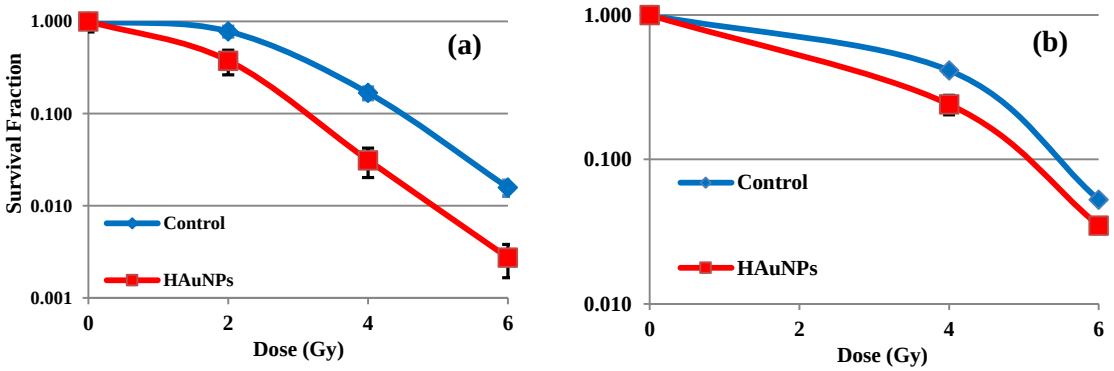

Figure 3-4 Survival curves for MBA-MB-231 cells irradiated with (a) 225 kVp X-rays, in which cells were given a 2 Gy, 4Gy and 6 Gy doses, and (b) 6 MVp X-rays, in which cells were given a 4Gy and 6 Gy doses. In both curves, the blue line refers to control cells whereas the red line is for cells cultured in the presence of 140 μM HAuNPs. For the survival curves, each data point represents the average of three independent experiments each plated in quintuplicate.

3.3 In vivo analysis

3.3.1 Animal tumor model

MDA-MB-231 human breast cancer cells were cultured in RPMI 1640 containing 10% fetal bovine serum, 1% penicillin-streptomycin antibiotics and L-glutamine (all from ThermoFisher Scientific, Waltham MA). 6-8 weeks old female SCID/NOD mice (average weight 21.8 ± 0.3 g) were obtained from the University of Texas Southwestern Medical Center (UTSW) core breeding facility. These mice were subcutaneously injected on both shoulder flanks with 3 x 10^6 MDA-MB-231 cells suspended in 100 µL of 1X PBS. The tumors were treated when they reached a size of 6 – 8 mm in diameter. All experiments were approved by the UTSW Institutional Animal Care and Use Committee in compliance with the United States Public Health Service Standards and National Institute of Health guidelines.

Mice bearing MDA-MB-231 tumors were subjected to a tumor growth delay assay wherein they were divided into 4 study groups (n = 7). Group **A**: A single fraction 10 Gy radiation + 2.8 mg HAuNPs per gram of tumor (intratumorally injected 12 h prior to irradiation); Group **B**: A single fraction 10 Gy radiation + saline injection; Group **C**: No irradiation + 2.8 mg/g of HAuNPs in tumor; Group **D**: No irradiation + saline injection.

The mice were monitored on a regular basis from the day of tumor implanting (pre-treatment) until the end of the entire course of study. The tumor-bearing mice were sacrificed based on the IACUC criteria, when the tumor volume exceeded 15 mm diameter (either length or width) or the tumor mass exceeded 10% of the body weight or > 20% loss of the original body weight. The weight of the mice was recorded every 2 days. Some mice were also sacrificed pre-term in case of any signs of toxicity or signs of animal discomfort (such as loss of limb function, loss of appetite, low body conditioning score).

3.3.2 Computed Tomography of Mice

Mice were scanned using computed tomography (CT) to validate the presence of HAuNPs in the injected tumors on a Siemens Inveon PET/CT Multi-Modality system (Siemens Medical Solutions, Knoxville, TN) with the effective spatial resolution of 1.4 mm at the center of FOV. Images were acquired post-injection of HAuNPs (2.8 mg/g tumor, 40 µL total volume) with animals (Groups **A** and **C**) under 1.5% isoflurane. CT images were acquired with the FOV centered at the shoulder of the mouse. CT projections (360 steps/rotation) were acquired with a power of 80 kVp, current of 500 µA, exposure time of 165 ms, binning of 4, and effective pixel size of 102 µm. Using a downsample factor of 2 and a Shepp-Logan filter, the CT reconstruction protocol was set to interpolate bilinearly. The CT images were analyzed using the manufacturer's software.

CT scan images revealed that the HAuNPs retained in the tumors after being injected at 5 – 6 locations, as shown in Figure 3-5. AuNPs, due to their higher x-ray attenuation, can be seen as brighter white spots in the tumor area (indicated by yellow circle). This retention could be due to the larger size of the HAuNPs, preventing their diffusion into the surrounding blood vessels and tissues, as evidenced by earlier studies as well[130, 134].

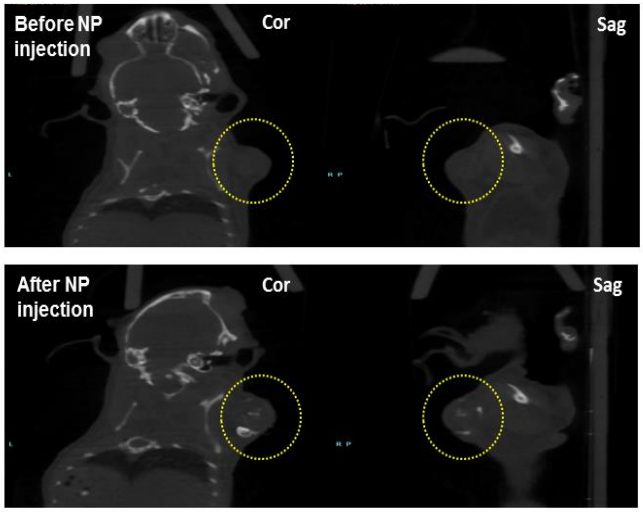

Figure 3-5 HAuNPs (2.8 mg/g tumor, 40 µL total volume) were injected at 5 to 6 sites on each tumor of mice in Group A and C. Coronal (left) and sagittal (right) planes of the CT image for one representative mouse are shown here. Yellow circle indicates the tumor with the injected HAuNPs, seen as bright white spots.

3.3.3 X-ray irradiation of the tumor bearing mice

The MDA-MB-231 breast cancer tumor bearing SCID/NOD female mice were irradiated using a small animal X-ray irradiator (XRAD 225, Precision X-ray Inc., North Branford, CT). The small animal irradiator provided X-ray beam energies of up to 225 keV at a dose rate of 3.9 Gy/min at distance of 30.5 cm. The beam size were shaped by brass cones with a variety of diameters projected to the iso-center. For the experiments, the mice were initially anesthetized by 2% of isoflurane in O_2 prior to irradiation, and then immobilized to a bed designed for irradiation in a position exposing the tumors in their shoulder region (setup shown in Figure 3-6). Before irradiation, cone-beam CT scans were acquired to reconstruct 3D images. Tumors were

accurately located in the volumetric images and the 3D moving platform positioned every target tumor at the irradiation iso-center for treatment. Cone collimators were mounted to shape beams sizes with diameters between 15 mm and 20 mm based on the individual target tumor size plus an isotropic margin of 5 mm. A single fraction radiation dose of 10 Gy was delivered to every target tumor.

One day prior to radiation therapy, all the treatment groups were scanned with magnetic resonance imaging (MRI), followed by intratumoral administration of ~ 40 µL volume of 2.8 mg/g HAuNPs or saline, which was carried out by 5 – 6 randomized injections into each tumor. At 12 h post-injection of HAuNPs, the mice of Groups **A** and **B** received a single fraction of 10 Gy radiation therapy.

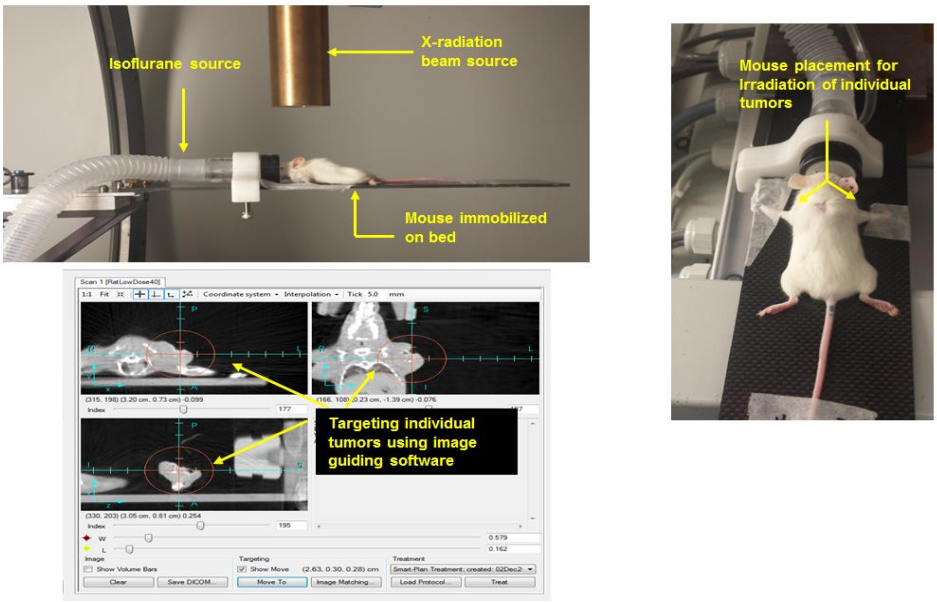

Figure 3-6 Experimental set up for the X-ray irradiation of tumor-burdened mice in Treatment Groups A and B.

3.3.4 Radiosensitization effect of HAuNPs in mice bearing breast cancer tumors

3.3.4.1 Tumor growth delay study

A tumor growth delay assay was used to assess the treatment efficacy of HAuNPs in mouse models with subcutaneous MDA-MB-231 tumors. The tumor growth delay was expressed as a normalized growth delay in tumor volume. Accordingly, the tumor growth delay is measured as the prolonged time of tumor growth from the original size to the endpoint size in a group treated with a combined regimen as compared to the other groups[186].

From day 2 to the end of the study when all the survived mice were sacrificed, the sizes of tumors in each study group were measured by a Vernier caliper every 2 – 3 days, in addition to the weekly MRI scanning. The tumor volume was calculated using the ellipsoidal formula of $\frac{1}{2} \times L \times W^2$ assuming the value of π to be 3[187].

Among the 4 studied groups, Groups C and D exhibited significantly higher tumor growth rates than Groups A and B, starting from Day 6 post-treatment until the end of the observation period for Groups C and D, *i.e.*, 25 and 28 days, respectively (Figure 3-7). After 30 days post-treatment, it can be seen that the slope of the growth rate curve for Group A was less than that for Group B, signifying delayed tumor growth. On Day 56, Group B average tumor volume was about 2.4-fold higher than that of Group A mice. Overall, the tumor growth rates for Groups A and B mice were not statistically different for the entire observation period of 56 days. However, it should be noted that many of the Group B mice had to be sacrificed pre-term, owing to their clinical conditions such as loss of limb function and limb swelling. Such conditions were attributed to the aggressive tumor growth pattern, despite the radiation treatment. In these instances, the radiation treatment potentially resulted in higher cell death and necrosis in initial stages of the study, causing a visible scab formation around the tumors. The scab formed around the growing tumors could gradually decrease the surrounding muscle blood flow, resulting in swelling of the fore-limb/s and even loss of limb function in specific instances. Interestingly, in comparison, such conditions were not seen in the Group A mice which survived

for an additional 32 days (Figure 3-7). A similar comparison between the tumor growth rates for Groups C and D mice showed no statistically significant difference. This suggested that the HAuNPs by themselves did not cause any therapeutic effect nor significant toxicity to the animals compared to saline only group (Figure 3-7 a).

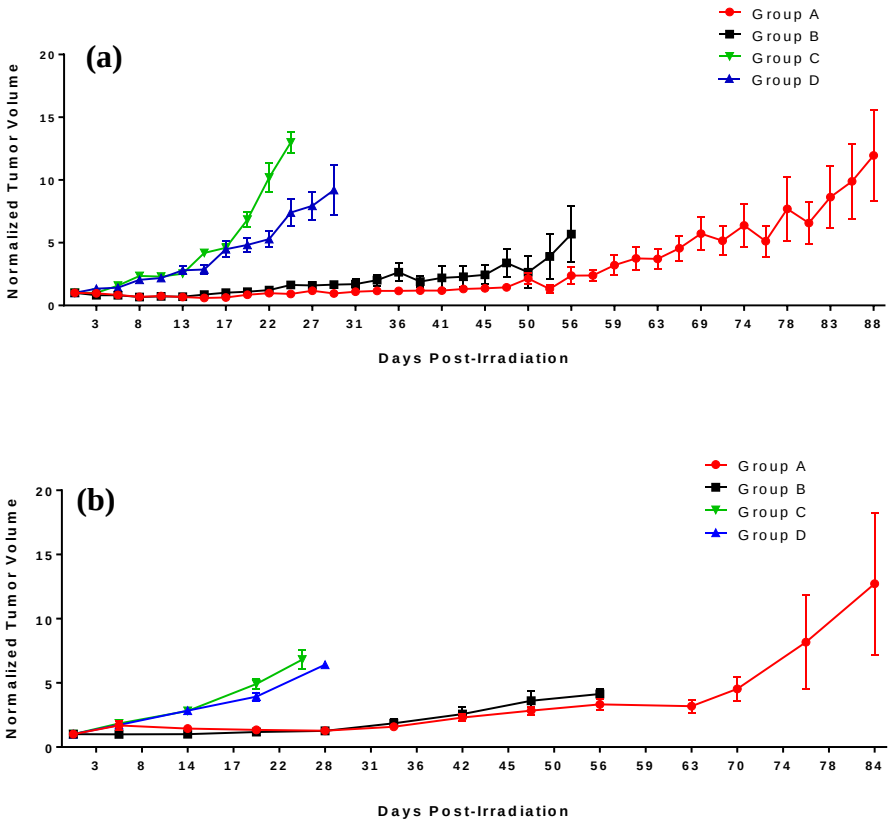

Figure 3-7 Tumor growth volume as measured by calipers (**a**) and MRI (**b**) and normalized to day 1 of radiotherapy. The data are represented as the Mean ± SEM for 7 mice at the start of the treatment. The animal number decreased as the result from the death or sacrificing of the animals over the course of the study.

3.3.4.2 Magnetic Resonance Imaging (MRI) of tumors

T_1 and T_2-weighted MR images were collected on an Aspect Imaging M2TM 1.0 T System using a 43.5−45 MHz, 35 mm diameter RF mouse coil. T_2-weighted Fast Spin Echo Sequence was performed with the following parameters: repetition time TR = 4000 ms; effective echo time (TE) = 73.8 ms; FOV 80 × 100 mm^2, data matrix = 256 × 230, averaging = 2, slice thickness = 1 mm. T_1-weighted Gradient Echo Spoiled sequence was performed using these parameters: TR = 15 ms; TE = 3 ms; FOV 80 × 100 mm^2, data matrix = 256 × 256, averaging = 3, slice = 1 mm. The field of view (FOV) was centered at the tumor. Each mouse was sedated during the imaging acquisition using 2% isoflurane. Tumor volume measurements were performed using the Invicro's Vivoquant 2.0 software package (Mediso, Boston, MA). After fusing T_1 and T_2-weighted images, a cylindrical region of interest (ROI) was drawn encompassing the tumor in all planes.

To obtain more accurate measurements for tumor growth, tumor volumes were also measured by MRI scans, as it is a clinically relevant modality which is commonly used in tumor delineation. This method is essential in determining actual (three-dimensional) tumor volume, which can be under or over estimated by calculated volumes from two-dimensional measurements using calipers. Nonetheless, it was found that the tumor growth rates determined by MRI for each of the groups showed trends similar to those seen with manual caliper measurements (Figure 3-7).

3.3.4.3 Survival study

Treatment with HAuNPs in combination with radiotherapy was found to facilitate the survival of tumor-burdened mice, as compared to the single-modality study groups B and C and untreated group D. Median survival of Group A (66 days) was approximately 2.6-fold longer than Groups C (25 days) and D (26 days) and 1.5-fold longer than Group B (40 days) (Figure 3-8). The individual survival curves were statistically compared using the Log-rank

(Mantel-Cox) test. As depicted in Figure 3-8, mice from Group A had prolonged survival which was significantly longer (p-value < 0.05) than that of the other groups (B, C and D). Moreover, the median survival time was significantly longer compared to that for Group B (40 days, p-value 0.0241), C (25 days, p-value 0.0090) and D (26 days, p-value 0.0047). From these findings, it can be inferred that the combination of radiotherapy and HAuNPs as radiosensitizers is a more effective treatment regimen than radiotherapy alone. Moreover, the HAuNPs can also be determined non-toxic, as there was no statistical difference between Groups C and D.

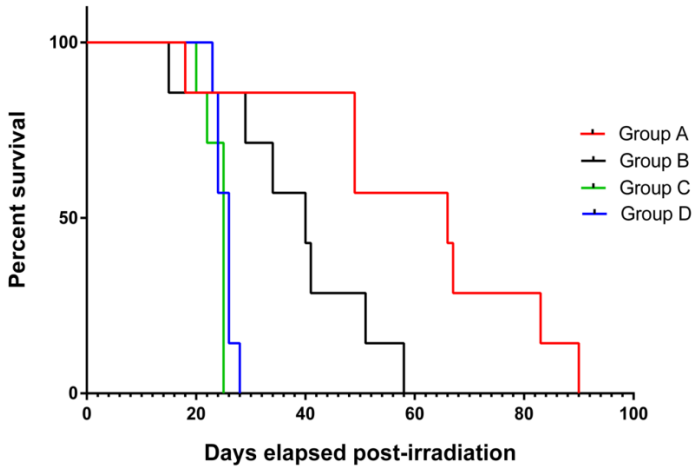

Figure 3-8 Kaplan-Meier survival curves for treatments Groups A, B, C, and D. n = 7 in each group.

3.3.5 Radiosensitization mechanisms by HAuNPs

To date, two major mechanisms have been proposed for the radiosensitization effect of AuNPs. As discussed earlier, large differences exist in the mass energy absorption coefficients between heavy (high Z) elements such as gold and soft tissue. Due to these physical differences, many theoretical studies used the possible interactions between X-ray and the heavy elements atoms to predict the dose distribution and enhancement around them. A main conclusion was that the high-Z materials will enhance the radiation dose at lower energy X-rays by photoelectric effect in which the conversion of the radiation photons to many highly localized Auger electrons would potentially cause cellular DNA damage.[117]

In the absence of high-Z materials, the primary mechanism by which X-ray photons lose their energy in the soft tissue is Compton scattering, which is an inelastic interaction between photons and the weakly-bonded electrons in an atom. Due to its inelastic nature, the amount of transferred energy is very low and it would result in a very sparse distribution of dose. However, as the emitted Auger electrons have very low energies and consequently short ranges in the biological tissue, they would only be able to cause DNA strand breaks and cellular damage within few tens of nanometers in the vicinity of the NPs.[117] Conversely, many experimental studies, including ours, have found higher radiosensitization effects than what could be predicted based on only the physical model.[117] In case of our study, not only the Auger electrons were far away from the nucleus of the cells to make any DNA damage, but also their number were significantly smaller than the previous studies due to the relatively large size of the utilized HAuNPs. Hence, other biological and chemical radiation enhancement mechanisms have been hypothesized, which mostly attribute the resultant cellular damage to AuNP-mediated increase in production of reactive oxygen species (ROS)[117].

It should be noted that the cellular damage by ionizing radiations can be through either direct or indirect interactions. In direct interaction, photon directly ionize the DNA molecules, whereas in indirect interaction, the radiation ionize the water molecules (radiolysis) and produce

free radicals, which subsequently react with DNA macromolecules and cause the damage. Since around 80% of soft tissue is water, it is widely accepted that the major fraction of radiation damage is caused through indirect interactions. The produced free radicals, also known as ROS, such as hydroxide free radicals ($OH^{\cdot}$), can be generated more in the presence of AuNPs, and can react with the surrounding biological molecules and DNA in the tumor microenvironment to generate additional ROS through a chain of chemical reactions[117, 188]. In addition to hydroxide free radicals, ROS include species such as superoxide radical (O_2^{-}), and hydrogen peroxide (H_2O_2) which could cause lipid oxidation, DNA and protein damage, and eventually would lead to necrotic cell death due to mitochondrial dysfunction[117, 189].

A recent study by Cheng et al. on the radiosensitization mechanism by different metal-based nanoparticles (platinum, gold, gold-silica core-shell) has reported a chemical mechanism to explain the radiation enhancement effect.[189] Based on their results, it can be hypothesized that the electronegative surfaces of the AuNPs in the presence of superoxides (formed due to AuNP-mediated radiolysis of water and biomolecules in presence of radiation) could generate additional OH radical-adduct intermediates.[189] These altered radical-adduct intermediates could then diffuse into cells and result in a cascade of events, causing cell damage, and eventually cellular death [117, 189]. Such enhancement could increase by the increase in the surface area and diameter of the NPs, as well as with increase of X-radiation dose.[189] Based on the obtained results of radiosensitization and intratumoral localization of the HAuNPs, the in vivo occurrence of this 'chemical enhancement' mechanism seems also probable. However, this hypothesis would still need to be further tested by additional experiments.

It should be noted that both the above-mentioned physical and chemical mechanisms have essentially assumed that AuNPs must possess close proximity to the cell nuclei[189, 190]. However, this assumption would clearly not apply in the case of our study, based on the CT images of the HAuNPs in the mice tumors (Figure 3-5). Similar observations were obtained by Herold et al., wherein Au microspheres (1.5 – 3 μm size) were intratumorally injected (1%

solution) in EMT-6 tumor-bearing mice, followed by irradiation with 8 Gy of 200 kVp X-rays. Resection of tumors conducted immediately after Au particle treatment demonstrated that even in the presence of the inhomogeneous distribution of Au particles (in the form of isolated pockets) within the solid tumors, these Au microspheres were still able to induce moderate cellular death [130]. These results in fact strongly suggest that the radiosensitization by AuNPs, including HAuNPs, isnot a much localized effect, in contrast to the most available physical predictions.

Indeed, this is particularly very important, as it eliminates the requirement of delivering AuNPs to every individual cells, which is practically very hard to achieve. It has been reported that biologically tumors are heterogeneous, and targeting schemes based on receptors or antibodies, or almost anything would result in heterogeneous distribution of the high-Z material[191]. Furthermore, higher cellular uptake requires smaller AuNPs, which in turn compromise their tumor retention. This can highlight further the importance of our results, which demonstrated that HAuNPs at a realistic concentration and without any extra surface functionalization and molecular targeting had very high tumor retention and significant radiosensitization effect. The overall conclusion is that the role of AuNPs should not be explained by a sole physical or chemical event, especially considering the complex microenvironment of tumors. In other words, AuNPs by a combination of physical enhancement (photoelectrons and low energy fluorescent photons) and chemical phenomena (chain reactions of free radicals) would cause biological events (producing toxic molecules which can also diffuse), excreting their effects to not only their close vicinity, but also to several cells away from them.

3.3.6 Toxicological analysis after treatment with HAuNPs and radiation therapy

At the end of the observation period for each treatment group, blood samples were collected from the heart as a terminal procedure. The toxicity was assessed by complete blood count (CBC) differential analysis. The hepatic function was analyzed by the changes of serum alanine aminotransferase (ALT) and aspartate aminotransferase (AST) levels; and the renal function by the assessment of the serum creatinine and blood urea nitrogen (BUN) levels. The ALT, AST, BUN and serum creatinine levels were analyzed in the UTSW metabolic phenotyping core using the Ortho Clinical Vitros 250 Chemistry System (Johnson and Johnson, United Kingdom). The CBC differential analyses were performed using Procyte Dx® Hematology Analyzer (IDEXX Laboratories, Westbrook, ME).

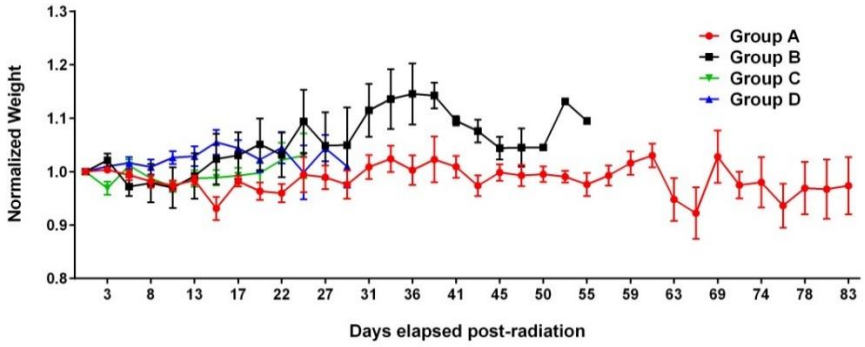

Figure 3-9 Normalized weight during the study period for Groups A, B, C, and D.

The chronic and acute toxicity after treatment using HAuNPs was evaluated to be negligible by weight assessment, blood chemistries, and vital organ (liver and kidney) function. For all the study groups, the average weight deviated only slightly from the starting weight (Figure 3-9). Toxicological and blood biochemistry assays were performed using whole blood

and plasma samples from all treatment groups at the end of the observation period, as shown in Figure 3-10. Statistical analyses showed that the red blood cells (RBC) and hemoglobin (HGB) values of Group D were significantly lower than those for Group B, while the hematocrit (HCT) values of Group D mice were significantly lower than those for Group A and B mice.

The progression of cancer has been associated with conditions such as decreased RBC counts, anemia, and a resultant decrease in hematocrit in patients pre-treatment, compared to healthy individuals.[192] Hence, in the Group D mice undergoing no treatment, the drop in the RBC, HGB and HCT values could be associated with the advancement of the cancer itself. These values were in the normal range for Groups A and B, and were slightly on the lower end for Groups C and D [Figure 3-10, normal ranges in SCID mice can be seen here: RBC (8.2 - 10.5 M/µL), HGB (12.1 – 17.6 g/dL) and HCT (44.6 – 58.3%)][193]. A slight reduction in the platelet counts (normal range: 651 – 1878 K/µL in SCID mice[193]) was observed in the mice from Groups A and B compared to the other 2 groups. Thrombocytopenia, although mild in this case, is usually a side-effect seen with radiation therapy, wherein there is a gradual decrease in platelet count[194]. An increase in the WBC levels was observed for the groups compared to the normal range (0.96 – 4.68 K/µL seen in healthy SCID mice[193]), which again is potentially due to body's response to pre-existent disease condition in this tumor growth delay study[192].

The hepatic function of the mice was analyzed by evaluating the alanine aminotransferase (ALT) and aspartate aminotransferase (AST) values from the plasma samples (Figure 4b). These enzymes levels are sensitive indicators measured to identify any hepatic stress, toxicity or disease affecting the liver function[195]. The values for these enzymes in healthy SCID mice range from 29 – 80 U/L for ALT and 63 – 227 U/L for AST[193]. There were no significant differences between the ALT and AST values for all the groups and these values were found to be within the normal range, indicating normal hepatic function of the mice throughout the study (Figure 4b). Similarly, the serum creatinine (SCr) and blood urea nitrogen (BUN) values are used to measure the glomerular function and hence are efficient measures of

kidney condition.[196] On evaluation of these values in mice plasma from the treatment groups, no significant difference was observed between them (Figure 3-10). These values were reported to be 16 – 28 mg/dL for BUN, and 0.2 - 0.5 mg/dL for SCr levels in SCID female mice according to recent literature.[193] Once more, the BUN and SCr values in the treatment groups were found to be within the normal range, suggesting normal renal function of the mice throughout the study period.

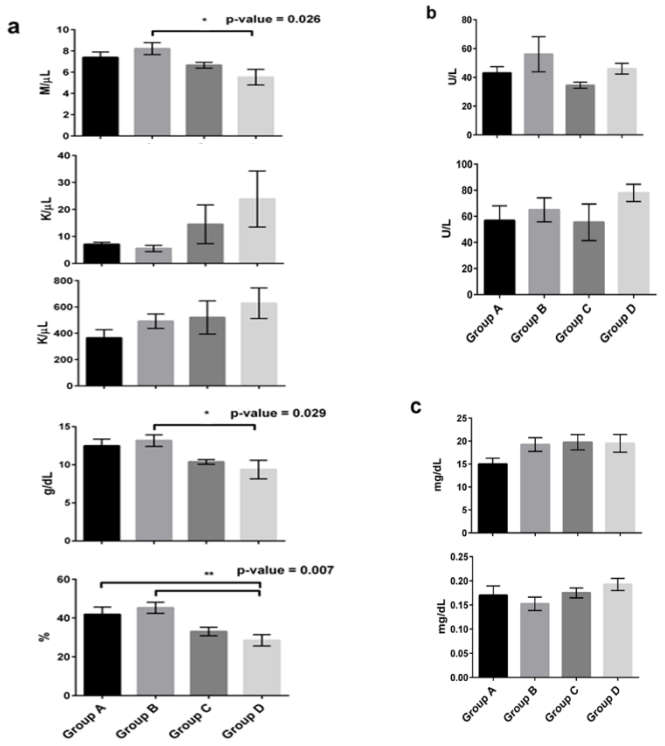

Figure 3-10 Toxicological analysis of blood samples collected from 4 study groups of mice. a) Hematological toxicity analysis; b) Hepatotoxicity analysis; c) Nephrotoxicity analysis. Each measurement is expressed as Mean ± SEM (n = 4). Statistical comparisons were performed using one-way ANOVA analysis followed by Tukey's post hoc test for multiple comparisons; * and ** for p-values < 0.05 and 0.01, respectively. RBC – red blood cells, WBC – white blood cells, ALT – alanine aminotransferase, AST – aspartate aminotransferase, SCr – serum creatinine, BUN – blood urea nitrogen.

3.3.7 Ex vivo biodistribution analysis of HAuNPs

At the end of the study, after all mice died or were sacrificed, ex vivo biodistribution analysis was performed on the mice from Groups A and C using ICP-MS. Upon sacrificing mice, tumors and other organs of interest (blood, heart, lungs, muscle, bone, fat, liver, spleen, kidneys, stomach, small intestine, large intestine, and brain) were excised and collected in pre-weighed glass vials. After being weighed, the tissues were digested using freshly prepared aqua-regia. Two days were allowed to ensure the complete digestion of the tissues and subsequent dissolution of the HAuNPs. After evaporation in a chemical hood by heating in an oil-bath at 150°C, the remaining matter in each vial was re-dissolved in 10 mL of 1% nitric acid and further sonicated for 30 min to ensure a homogeneous dispersion of gold. The solution was then centrifuged at 4000g for 10 min to remove any particulates and the supernatant was analyzed for gold by inductively coupled plasma mass spectrometry (ICP-MS, Agilent 7700X). The measurement was repeated at least 3 times for each sample.

Along with the CT images (Figure 3-5), the mass spectrometry analysis further validated the significantly high retention of the HAuNPs inside the tumors. Biodistribution data of Groups A and C (the two groups that received HAuNPs by injection) indicated that 97.4 ± 3.71% of the gold remained in the tumors, while only 1.3 ± 0.58% and 0.2 ± 0.08% gold accumulation were observed in the liver and spleen, respectively. Other tissues showed negligible uptake of the gold. High retention in the tumors facilitates reduced accumulation of the HAuNPs in vital organs, potentially reducing chronic toxicity.

In this in vivo study, HAuNPs were used without any surface modification, in contrast to other earlier in vivo reports demonstrating radiosensitization effects of targeted AuNPs.[134, 197, 198] Surface functionalization of AuNPs using target-specific molecules (such as peptide, antibodies etc.) has shown improved intracellular uptake and resultant radiosensitization[134, 197, 198]. However, surface modification would be an essential consideration for tumor-targeting, during intravenous administration of nanoparticles. As mentioned earlier, intravenous administration

could result in poor bioavailability for accumulation in the tumors. To overcome this, higher nanoparticle doses are generally administered, which could potentially be associated with systemic toxicities. The applied methodology of intratumoral injections of HAuNP in this study would aid in achieving higher local concentrations of the nanoparticles in the tumor microenvironment with minimal (if any) systemic effects[114, 126, 130, 131, 134, 178]. Owing to intratumoral administration of the as-synthesized HAuNPs and their high tumoral retention, a reasonable radiosensitization was observed with significantly improved survival of the mice, despite the absence of any surface modification. Moreover, this retention enabled utilization of a much lower dose of the HAuNPs in this study as compared to previous reports [130, 134]. Additionally, the physical structure of the HAuNPs, *i.e.*, the hollow core itself as well as the arrangement of the gold atoms within the nanoparticles, may possibly hold an advantage towards an improved radiosensitization effect.

Chapter 4 Radioactive gold nanoparticles for efficacious brachytherapy of solid malignant tumors

4.1 Introduction

Highly-localized Internal radiation therapy (brachytherapy) has been widely used in the control of inoperable (or unresectable) solid tumors, in which the radioactive sources are sealed in a metallic (titanium etc.) container with the size about one rice, namely the brachytherapy seeds [199]. To confine the radiation to tumor sites, two approaches are currently in clinical practice; systemic radioisotope therapy using targeted radiopharmaceuticals, and brachytherapy using sealed radioactive sources. In brachytherapy, radioactive sources are surgically placed into or next to the tumor volume, whereby the radiation dose is delivered continuously, either over a short period of time (temporary implants) or over the lifetime of the source to a complete decay (permanent implants). The seeds for permanent implants are usually prepared by sealing a low dose radioactive source such as ^{103}Pd (t1/2 = 17 d; 100% EC; E X-ray = 21 keV) and ^{125}I (t1/2 = 59.4 d; 100% EC; EX-ray = 35 keV) in a metallic (e.g. titanium) container with the size about one rice.

Brachytherapy effectively confines the therapeutic radiation dose to the tumor region while sparing normal tissues. However, the surgical implantation of millimeter size brachytherapy seeds, commonly used for the treatment of prostate cancer1–5, causes many adverse side effects and greatly limits its applications. Moreover, due to the millimeter size of the seeds, following the surgical implantation a majority of patients would experience post-treatment symptoms ranging from adverse side effects to severe clinical complications. For instance, PCa patients commonly experience problems with urination for a few months and suffer other clinical complications such as pelvic pain due to the heterogeneity of implanted seeds, loose and frequent stools from rectal mucosal irritation, and reduction in ejaculate

volume with time as the prostate gland becomes more fibrous. Many of these side effects are caused by the millimeter size of the seeds[200-208].

With the rapid development of nanoscience and nanotechnology, it becomes appealing to make injectable nano-scale brachytherapy seeds. Because much smaller needles can be used for injection of nanoseed colloidal solution, nanoseed-based internal radiation therapy can reduce the trauma caused by surgical implantation. Reducing the seed size to nanoscale and making it injectable would avoid most adverse side effects and also greatly expand the applications of internal radiotherapy to treat much smaller tumors and other diseases, to be intraoperatively applied in situations where optimal surgical resection is not possible, and to be used postoperatively to target potential regions of residual microscopic disease.

However, there exist some major challenges which are severely hindering the development of nanoscale brachytherapy seeds. Radioactive chemicals with medical isotopes (precursors) are usually prepared in solution with trace level concentration (~10^{-8}M). Thus, an efficient nanoparticles-radiolabeling method is required to incorporate sufficient radioactive dose in reasonable number of nanoparticles for therapeutic use. On the other side, the size of nanoseeds needs to be large enough to prevent these radioactive particles from diffusing into other areas, which is again a common problem in nanomedicine using nanoparticles. Therefore, here in this chapter, the method to develop a radiolabeling process to incorporate therapeutic radioisotopes into monodispersed large AuNPs to produce nanoseeds for more efficient treatment of inoperable solid tumor cancers with significant reduction of adverse side effects has been studied. After developing nanoscale brachytherapy seeds, their in vivo therapeutic efficacy and biodistribution are studied in prostate xenografts. Finally, through the entire chapter, the practical significance and the potential clinical applications of the synthesized nanoseeds will be discussed.

4.2 Synthesis of AuNP-based radioactive nanoseeds

4.2.1 Synthesis design of theranostic nanoseeds

To incorporate the therapeutic radioisotopes onto AuNPs, a two-step process was developed as illustrated schematically for ^{103}Pd in Figure 4-1. The hollow Au nanoparticles were first coated with Cu by an electroless deposition process. Then, the Cu layer is replaced by an inerter metallic precursor (Pd) through a galvanic reaction. This Cu-mediated process provides a facile way to incorporate radioisotopes onto Au nanoparticles from solutions with a trace level concentration.

The electroless deposition of Cu on Au surface is a simple and robust process. Cu can be readily replaced by less reactive metals through simple galvanic exchange reactions using aqueous solution containing metal ions without any other additives. Using this synthesis method, several therapeutic radioisotopes less reactive than Cu such as ^{192}Ir, ^{198}Au, ^{199}Au, ^{105}Rh, ^{195}mPt, ^{109}Pd, and ^{103}Pd can be incorporated onto Au nanoparticles. Here we applied this method to incorporate a commonly used radioisotope in brachytherapy seeds, ^{103}Pd, onto hollow gold nanoparticles to form ^{103}Pd@Au nanoseeds. ^{103}Pd decays by electron capture with the emission of characteristic x-rays in the energy range of 20 to 23 keV (average 20.9 keV) and Auger electrons with a half-life of 17 days. ^{103}Pd brachytherapy sources are being used for interstitial brachytherapy implants in various tumor sites and particularly for prostatic carcinomas. ^{103}Pd may have advantages over other commonly used brachytherapy radioisotopes (like ^{125}I) because of its shorter half-life, higher initial dose rate, and increased dose heterogeneity within the target volume.

Medical radionuclides are usually prepared in solutions with trace levels. The developed Cu-mediated radiolabeling process provides a facile way to efficiently incorporate radioisotopes onto AuNP surface from such dilute solutions. The main advantage of this process in its simplicity and high proficiency. The electroless deposition of Cu on Au surface is a simple and

robust process. Successively, Cu can be readily replaced by less reactive metals through a single displacement reaction in an aqueous solution containing metal ions without any other additives.

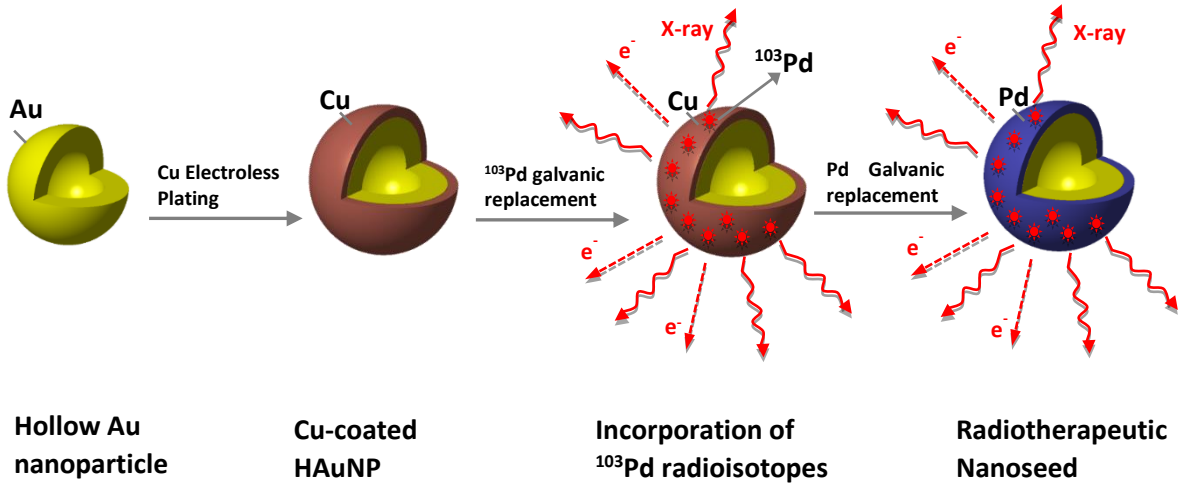

Figure 4-1 Synthesis design of ^{103}Pd@Au nanoseeds**;** schematic of the process of incorporation of ^{103}Pd radioisotope onto HAuNPs. First, a Cu layer is deposited by an electroless deposition process. Then, the some Cu atoms are replaced by ^{103}Pd radioisotopes through galvanic exchange, and finally Pd atoms replace remaining Cu layer by the same reaction. The synthesized nanoseeds will emit Auger electrons and characteristic x-rays.

4.2.2 Materials

$PdCl_2$ and $CuSO_4.5H_2O$ were obtained from Sigma-Aldrich (St. Louis, MO) and Alfa Aesar (Ward Hill, MA), respectively. Radioactive ^{103}Pd was purchased from Nordion (Ontario, Canada). PBS was purchased from Invitrogen Corporation (Carlsbad, CA). All other solvents

and reagents were of analytical purity grade and were purchased from VWR (Brisbane, CA). All aqueous solutions were prepared in Millipore Milli-Q water (18 MΩ-cm) that was obtained from a Millipore Gradient Milli-Q water system (Billerica, MA).

4.2.3 Synthesis of hollow gold nanoparticles (HAuNPs)

HAuNPs were synthesized using bubble template synthesis developed by our group at the University of Texas at Arlington [179]. Briefly, in this method, electrochemically evolved hydrogen nano-bubbles captured inside AAO channels serve as templates. Commercial AAO membranes () with channel size of 200 nm were used in the process. The high concentration of hydrogen molecules in the bubble boundary reduces the Au^{+3} ion to form Au clusters. Subsequently, the metal clusters act as catalysts to trigger the autocatalytic disproportionation reaction of $Na_3Au(SO_3)_2$, which leads to the formation of a gold shell around the hydrogen bubble. The metal Au gradually grows from clusters or particles to a porous network. The synthesized HAuNPs typically feature a sub-25 nm shell with a 50-70 nm hollow core.

4.2.4 Synthesis of Cu-coated HAuNPs

Electroless copper deposition was conducted at room temperature. The electroless copper plating bath consisted of 0.4 M copper sulfate ($CuSO_4.5H2O$), 0.17 M ethylenediaminetetraacetic acid (EDTA) and 37 % formaldehyde (HCHO). The pH level was adjusted to 10 by the addition of 1 M sodium hydroxide (NaOH). The above aqueous Cu plating solution was first delivered into the nanochannels of the AAO membranes, with HAuNPs entrapped inside, using a vacuum filtration setup. Then, the membranes were immersed in the same solution bath for 20 min without disturbance.

4.2.5 Synthesis of ^{103}Pd@Au nanoseeds

After electroless Cu deposition, the membranes containing Cu-plated HAuNPs were washed with water three times. The washed AAO membranes containing Cu-coated AuNPs then were drained with 0.4 M citric acid solution using a vacuum filtration setup to completely soak the nanochannels of the membranes with citric acid. Then they were immersed in 3 ml of 0.4 M citric acid solution containing the desired radioactivity amount of ^{103}Pd radioisotopes (4.37 mCi ^{103}Pd). The exchange reaction between Pd^{2+} ions and metallic Cu would occur due to the difference between the reduction potentials of Pd ions and Cu atoms. Plating of ^{103}Pd onto HAuNPs was then continued for 24 h, followed by addition of cold Pd plating solution (2.5 mM palladium chloride ($PdCl_2$) in 0.4 M citric acid solution) to replace all remained Cu layer. After 1 h, 2 M NaOH solution was added to dissolve the membrane and the resultant ^{103}Pd@Au nanoseed suspension was washed three times with water by centrifugation at 14000 rpm for 10 min with ultrasound-dispersion after each centrifugation run. The resultant pellet of ^{103}Pd@Au nanoseeds was then dispersed by sonication in required quantity of PBS 7.4.

The overall process yielded ^{103}Pd@Au nanoseeds with > 80 % radiolabeling efficiency as determined by dose calibrator (Capintech Inc, PA, USA). Dynamic light scattering (DLS) assessment confirmed the synthesized ^{103}Pd@Au nanoseeds to be monodisperse with mean particle size of 140.5 ± 7.6 nm. The total synthesis time of ^{103}Pd@Au nanoseeds was approximately 26 h. The ^{103}Pd@Au nanoseeds were found to be extremely stable and retain their original size even after being shelved for 2 months at 8 ± 2 °C. Although the caking of ^{103}Pd@Au nanoseeds was observed during the storage, it can be reconstituted with phosphate-buffered saline (PBS) uniformly. The TEM images of HAuNPs and nanoseeds are presented in Figure 4-2. As can be seen, after palladium coating, a Pd shell (confirmed by EDS) of about 15 nm would cover the HAuNPs. The contrast between the Au core and Pd shell is due to the difference between their atomic numbers.

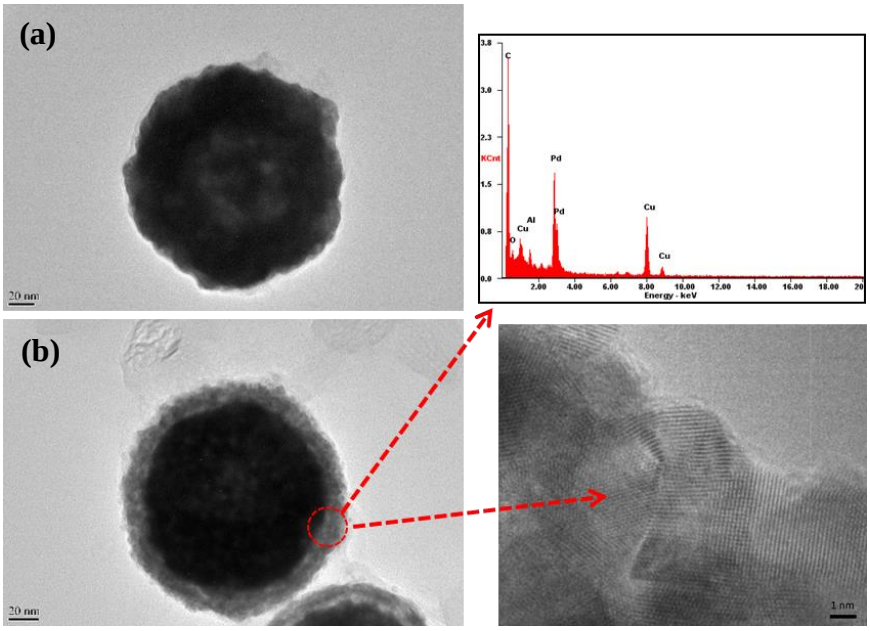

Figure 4-2 (a) HRTEM image of hollow gold nanoparticle before Pd coating, and (b) HRTEM image of Au@Pd core-shell nanoseeds with EDS spectrums of the Au core and Pd shell of Au@Pd nanoseeds and high magnification HRTEM image of the outer Pd layers showing the lattice fringes of Pd.

Galvanic replacement reaction is an electrochemical process that involves the oxidation of one metal, sacrificial template, by the ions of another metal (deposited metal) having a higher reduction potential. Upon contact in a solution phase, the template will be oxidized and dissolved into the solution while the ions of the second metal will be reduced and plated onto the outer surface of the template. This simple reaction can be employed to generate a wide variety of metal nanostructures (sometime with very complex morphologies), and only requires

a favorable difference in the reduction potentials of the two metals. Different aspects of metallic nanostructures made by means of galvanic replacement, such as elemental composition, internal structure, and morphology, have been studied in the last decade [209].

It has been generally accepted that the galvanic replacement reaction at nanoscale involves several sequential major steps, including simple replacement, small-hole generation, alloying, and dealloying. Each of those steps are governed by their own mechanisms, which in turn are influenced by experimental condition (like precursor concentration, reaction temperature, additive agents), and intrinsic materials properties (such as crystal structure, surface energy, stacking fault, and diffusion coefficient). Despite the interesting results found on the impacts of determining parameters on the galvanic replacement mechanisms, there are yet unknown factors (facet selectivity, capping agents effect, and so forth) to be systematically investigated [210].

4.2.6 Synthesis of ^{198}Au@Au nanoseeds

Internal radiotherapy involves the administration of a radioactive dose that either ablates or damages the diseased tissue through the emission of energetic particles and/or electromagnetic rays. The high energy particle can be a β particle, an α particle, or an Auger electron. Several factors must be considered in choosing a particular radioisotope for therapeutic applications, such as physical half-life, energy of the particle emission, type of particle emission, specific activity, and the cost and availability of the radioisotope. The choice of type and energy of the particle emission is largely determined by the size of the tumor being treated, site of delivery, whether the tumor is homogeneous, and whether the dose can be delivered uniformly to the targeted area. To expand the application of the invented radioactive nanoseeds, it is crucial to prove that different types of therapeutic radioisotopes, including particle emitters, can also be incorporated into AuNPs by the developed Cu-mediated radiolabeling process. As mentioned earlier, therapeutic radioisotopes that are less reactive

than Cu (such as ^{192}Ir, ^{198}Au, ^{199}Au, ^{105}Rh, ^{195}mPt, and ^{109}Pd) can be incorporated into AuNPs using Cu-mediated radiolabeling method. ^{198}Au and ^{105}Rh are two β-emitter radioisotopes which are getting more attractions as suitable radionuclides for brachytherapy.

^{198}Au is a reactor-produced radionuclide with a half-life of 2.7 days. It emits a β particle with a maximum energy of 0.96 MeV (99%) suitable for therapeutic applications and a 412 keV (95.6%) γ-ray that can be used for imaging and localization in biodistribution studies. Recently, there has been widespread interest in designing and developing well-defined ^{198}AuNPs for tumor therapy applications, and the therapeutic efficacies of these nanoparticles in animal models have been studied (see chapter 1). Here, we report using our Cu-mediated radiolabeling method to produce ^{198}Au@Au nanoseeds.

The procedure utilized to synthesis ^{198}Au@Au nanoseeds is quite identical to that of Au@^{103}Pd nanoseeds, except that ^{103}Pd and PdCl2 were replaced by ^{198}Au and HAuCl4, respectively. Similarly, the HAuNPs attached to the inside of AAO nanochannels were put inside the copper electroless plating bath consisting of 0.4 M $CuSO_4$ for 20 min. Then, the Cu-coated AuNPs were transferred to a bowl containing tracer ^{198}Au dissolved in 0.4 M citric acid. ^{198}Au atoms would oxidize and replace the Cu atoms through a galvanic reaction. After leaving the bowl undisturbed for 3 hours to make sure the coating of maximum number of ^{198}Au atoms, the nanoparticles were added to an aqueous solution of 2.5 mM $HAuCl_4$ to totally replace all the Cu layer with Au atoms and yield only a gold shell on the outer surface of the nanoparticles. The radiolabeling efficiency through this 3-hours process was ~35%. Regarding the shorter half-life of ^{198}Au, versus 17 days of ^{103}Pd, continuing the coating process for longer times would cause considerable loss in the final radioactivity. The HRTEM image of Au@Au core-shell NPs is shown in Figure 4-3, demonstrating similar morphology to Au@Pd core-shell NPs.

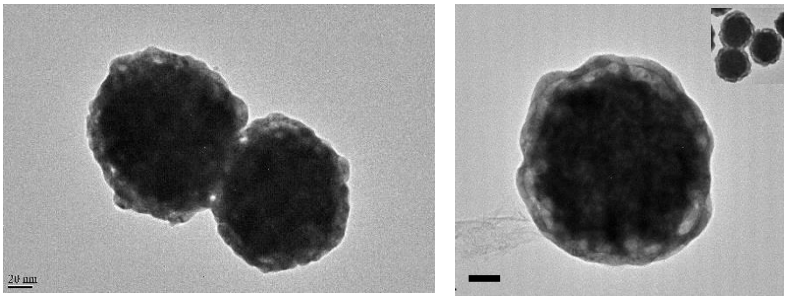

Figure 4-3 High resolution TEM micrograph of Au@Au nanoparticles. The scale bar is 20 nm.

Thereby, in addition to ^{103}Pd, we were able to synthesize nanoseeds with other therapeutic radioisotopes that are chemically less reactive than Cu, such as ^{198}Au and ^{105}Rh. Therapeutic Cu isotopes (e.g. ^{64}Cu and ^{67}Cu) can also be incorporated. To date, β-emitters have not been utilized for brachytherapy because radioactive sources are encapsulated and only gamma/X-ray can penetrate the capsule. In our nanoseeds-based approach, encapsulation is no longer needed, therefore, it opens up the possibility using β-emitters for brachytherapy.

These isotopes are β-emitters. Compared with photon (gamma/X-ray) emissions, β−particles have much shorter radiation ranges, and are used in systemic radioisotope therapy. To date, β-emitters have not been normally utilized for brachytherapy as radioactive sources are encapsulated and only gamma/X-ray can penetrate the capsules. Given that the encapsulation is no longer needed, our nanoseed-based approach opens up the possibility to use β -emitters for brachytherapy.

4.3 Administration of nanoseeds into tumor xenografts and their in vivo biodistribution

4.3.1 Animal model

All animal care and experimental procedures were approved by the University of Texas Southwestern Medical Center Institutional Animal Care and Use Committee in compliance with the United States Public Health Service Standards and National Institutes of Health guidelines. All experiments were performed on SCID mice (Male, 27 ± 2 g, Age 6–8 weeks). Throughout the experiment, the animals were housed in laminar flow cages maintained at 22 ± 2 °C, 50–60% relative humidity, under a 12-hr light:12-hr dark cycle. Four mice per plastic cage were housed and allowed to acclimatize in standard conditions for one week. The mice were permitted free access to tap water and commercialized food (Jae Il Chow, Korea), throughout the experiment. Severe combined immunodeficiency (SCID) mice bearing human prostate cancer tumors were used for in vivo evaluation of the nanoseeds, including their retention in tumor sites, toxicity, and therapeutic efficacy. Tumor induction was done by following methods reported earlier with slight modifications. The cell suspension containing 3×10^6 PC3 cells was implanted subcutaneously into both shoulders of SCID mice. Tumors were allowed to grow for 4 weeks to reach a palpable size (~181.7 ± 62.1 mm3). Animals were randomized at day 0 into three groups (n = 6) to be treated with PBS solution only, cold Au@Pd nanoparticles in PBS, and hot (radioactive) nanoseeds in PBS suspension, respectively.

4.3.2 Intratumoral administration of cold nanoparticles and hot nanoseeds

The injection was performed intratumorally at 6 to 9 locations on each tumor so as to achieve an even distribution of the radiation dose in the whole tumor mass. The injected radioactivity of ^{103}Pd@Au nanoseeds was ~1.5 mCi per tumor. The injected volume was maintained under 40 µL for all three groups: PBS only (control), cold Au@Pd nanoparticles, and

nanoseeds. The gold nanoparticle concentration in each injection was maintained at 2.03×10^{10} nanoparticles/mL.

4.3.3 SPECT imaging using the low energy emission of ^{103}Pd

A SPECT imaging method with ^{103}Pd was developed in a NanoSPECT/CT Plus System (Bioscan, Washington, DC, USA). ^{103}Pd isotope was added to the NanoSPECT/CT Plus isotope library by setting the energy peak and width to 18 keV and 60%, respectively. Quantification calibration was performed subsequently using a 3mL syringe and 1.2mCi of ^{103}Pd. After injection, small animal imaging was performed using NanoSPECT/CT Plus System. After the intratumor injection of each dose, SPECT and CT images were acquired at 0, 1, 2, 4, 7, 14, 21 and 35 days post injection (d.p.i.). The field of view (FOV) of the SPECT/CT was centered at the shoulders of the mouse. The CT imaging was performed using 360 projections per rotation with 55kVp, 1000 ms exposure, and the binning factor of 1:1. The SPECT data were collected with 4 detector arrays collimated with multi-pinhole apertures giving a post-reconstruction resolution of 0.73mm. The SPECT image reconstruction was carried out using HiSPECT NG (Scivis wissenschaftliche Bildverarbeitung GmbH, Germany) with 35% smoothing, 100% resolution, and 3x3 iterations (Standard mode). The quantification of the tumor activity was performed using the InVivoScope 2.0 software package (Bioscan, Washington, DC, USA). After co-registration of the CT and SPECT images, a cylindrical region of interest (ROI) was drawn, encompassing the tumor and liver in all planes containing the organs.

4.3.4 SPECT analysis to monitor in vivo tumor retention of the nanoseeds

For nanoseeds-treated group, after the intratumoral injection, SPECT/CT imaging was conducted in a longitudinal manner to noninvasively monitor the retention of the nanoseeds by acquisition of the low energy X-ray emissions of ^{103}Pd on a small animal SPECT/CT scanner. The quantitative SPECT analysis performed at 1 d.p.i. (Figure 4-4) clearly showed the injected

dose stayed at the site of administration (101.50 ± 23.72 % ID/g) with negligible amounts of radioactivity observed in the liver (0.11 ± 0.06 % ID/g) and spleen (0.14 ± 0.01 % ID/g), which are the major sites for uptake and deposition of Au nanoparticles [211]. As the study was progressing, the uptake level in tumor determined by quantitative SPECT analysis increased gradually to 274.48 ± 77.62 % ID/g at 5 w.p.i, as the tumor volume shrunk due to the radiotherapeutic effect of the nanoseeds.

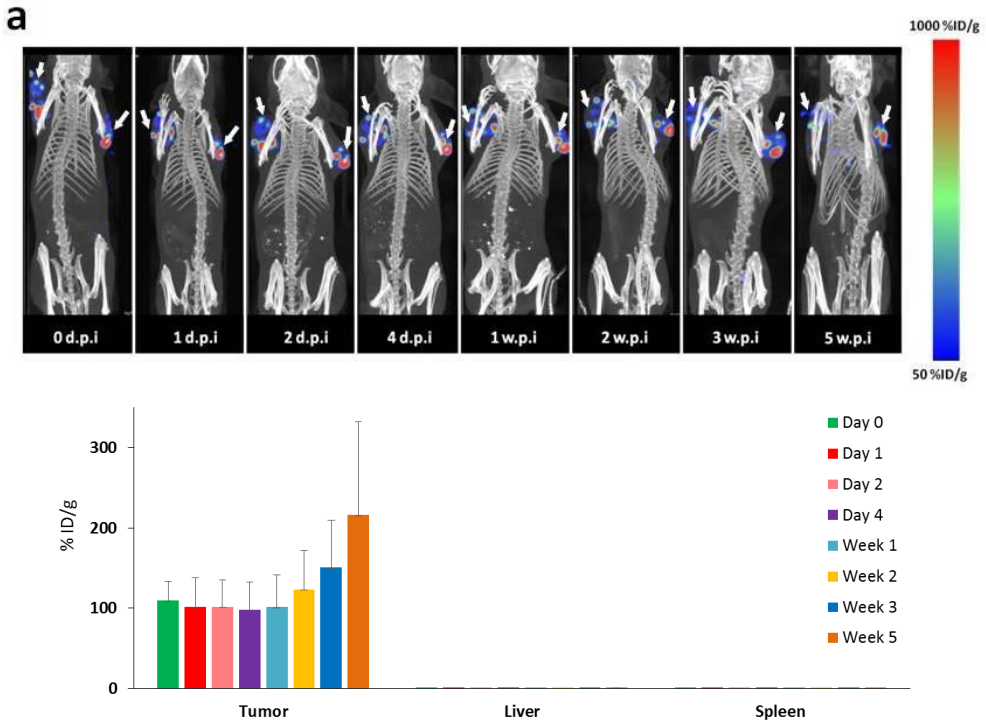

Figure 4-4 Retention of the injected ^{103}Pd@Au nanoseeds at tumor sites. (a) Serial SPECT/CT imaging performed 0, 1, 2, 4, 7, 14, 21, and 35 days post intratumoral injection of 1.51 mCi ^{103}Pd@Au nanoseeds in PC3 tumor bearing SCID mice. White arrows indicate tumors and the radioactivity coming from ^{103}Pd, (b) the quantitative SPECT analysis of radioactivity (quantified as percentage injected dose per gram, %ID/g) from tumor, liver and spleen. %ID/g associated with tumor increased progressively due to the reduction in tumor volume.

4.4 Therapeutic efficacy of ^{103}Pd@Au nanoseeds in brachytherapy of prostate cancer

4.4.1 Tumor growth study

Tumor volumes in the three groups of tumor-bearing mice were measured using a caliper every other day in a double-blinded manner. Quantitative data were expressed as mean ± standard errors of mean (SEM). Comparison among the means and the significance evaluation were performed by one-way ANOVA, where P values of <0.05 were considered statistically significant. The data from different groups and within each individual group at different time points were compared to determine whether they are statistically distinguishable. All data analysis was carried out using SPSS Ver. 16.0 software (IBM SPSS Statistics).

The tumor volumes (Figure 4-5) in the three groups of tumor-bearing mice were measured using a caliper every other day in a double-blinded manner. After 15 d.p.i, a clear separation of tumor growth trend was seen ($p < 0.0001$). As expected, over the 5-week treatment period, a prominent reduction in tumor volume growth was noted in ^{103}Pd@Au nanoseeds treated subjects, while progressive increment in tumor volume was observed in both PBS and cold Au@Pd nanoparticle treated groups. It is noteworthy that the volume of two tumors in two mice in nanoseeds treated group shrank so much that they cannot be found after 35 d.p.i. The average tumor size in the control and cold Au@Pd nanoparticle treated groups increased from 67.08 ± 30.96 mm^3 and 58.75 ± 35.29 mm^3 to 187 ± 80.11 mm^3 and 122.14 ± 4.082 mm^3, respectively. On the other hand, in the ^{103}Pd@Au nanoseeds treated group, a significant tumor size reduction was observed: 82.75 ± 46.25 mm^3 to 19.83 ± 20.12 mm^3 ($p < 0.001$) after 35 days of treatment. It is noteworthy that two mice in the nanoseeds-treated group were found virtually tumor free after 35 d.p.i.

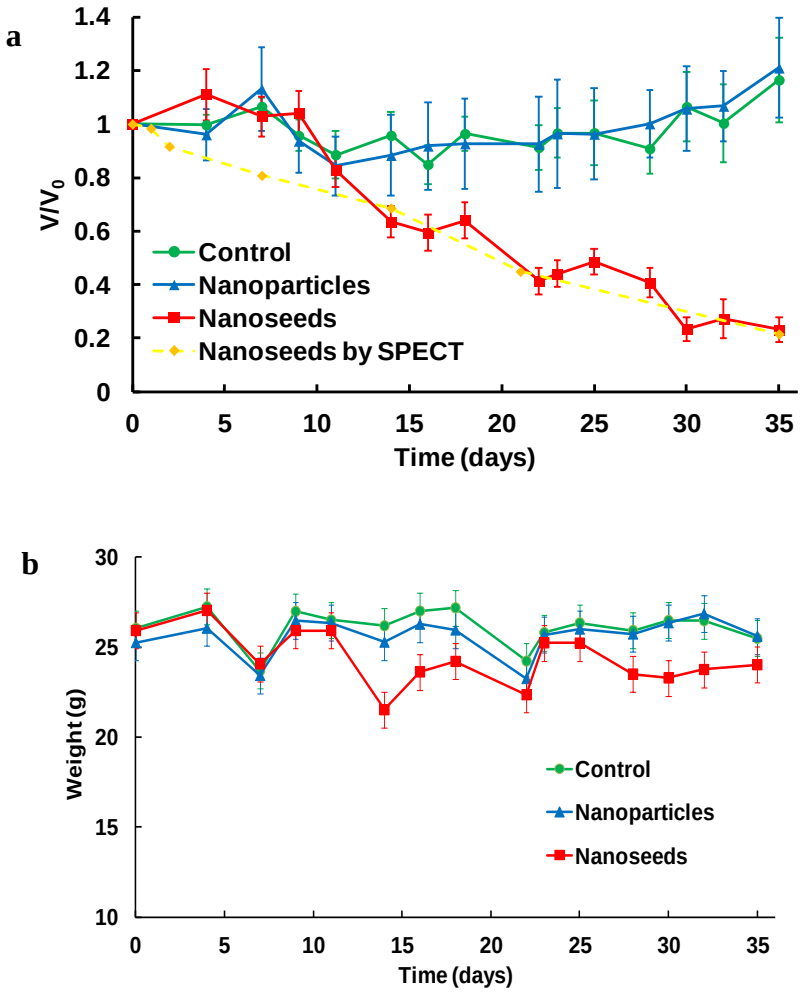

Figure 4-5 (a) Tumor volume and (b) body weight during the progression of therapy.

4.4.2 FDG-PET/CT imaging analysis

[F18]FDG (2-[^{18}F]Fluoro-2-deoxyglucose) positron emission tomography (PET) imaging was also employed for assessing therapeutic efficacy of the nanoseeds. FDG-PET imaging is widely used in oncology clinics to noninvasively assess the therapy response[212-214]. Unlike anatomical and morphological assessment, FDG-PET imaging can give functional and metabolic information of the tumor by monitoring the FDG (a glucose analog) consumption of cells, and therefore provide a direct measuring of the cell viability.

Mouse PET/CT imaging was performed using Siemens Inveon PET/CT multimodality system (Siemens Medical Solutions, Knoxville, TN) with effective spatial resolution of 1.4mm at the center of field of view (FOV). All animals were fasted for 12 hours prior to PET imaging. Each mouse received 150uCi of FDG in 150uL in saline intravenously via tail vein injection. The mice were placed on a heat pad before and during image acquisition. PET images were acquired one hour post-injection (P.I.), for 15 minutes, with animals under 2.5% Isoflurane. PET images were reconstructed into a single frame using the 3D Ordered Subsets Expectation Maximization (OSEM3D/MAP) algorithm. CT images were acquired immediately after PET with the FOV centered at the shoulder of the mouse. CT projections (360 steps/rotation) were acquired with a power of 80 kVp, current of 500 μA, exposure time of 145 ms, binning of 4, and effective pixel size of 102 μm. The CT reconstruction protocol used a downsample factor of 2, was set to interpolate bilinearly, and used a Shepp-Logan filter. PET and CT images were co-registered in Inveon Acquisition Workplace (Siemens Medical Solutions, Knoxville, TN) for analysis. Regions of interest (ROI) were drawn manually, encompassing the tumor in all planes containing the tissue. The target activity was calculated as percentage injected dose per gram.

Figure 4-6(a) shows typical FDG-PET/CT scan images for the three studied groups of mice at different time points. It can be seen that at Day 0, the mice from all the three groups had roughly the same tumor sizes with similar FDG uptakes, while as the study progressed for 35 days, a significant tumor FDG uptake reduction was observed in the nanoseeds treated group

(upper panel) as compared to that in the PBS (lower panel) and cold Au@Pd nanoparticles (middle panel) treated groups. The quantitative PET analysis is illustrated in Figure 4-6(b) as the maximum standardized uptake value (SUV_{max}) versus time. The SUV represents the concentration of radioactivity in the tumor, normalized to the injected FDG dose and the body weight. It shows that SUV_{max} for the mice treated with the nanoseeds decreased 62% from day 0 to day 35 ($p = 0.00041$), and at day 35 it is 65% ($p = 0.00019$) and 66.5% ($p = 0.00028$) less than that in PBS and cold nanoparticles treated groups, respectively. The decrease in the SUV_{max} of nanoseed-treated group to such a low level is a clear evidence on the pathological responses of the tumors to the radiation therapy by the nanoseeds. CT images obtained were also utilized to determine the tumor volume, as shown in Figure 4-6(c), which further validates the volume change result measured using the caliper.

This remarkable high therapeutic efficacy can be attributed to a more homogeneous dispersion of radioactive sources and therefore more effective delivery of therapeutic payload to cancer cells. It may also come from the fact that AuNPs in the synthesized ^{103}Pd@Au nanoseeds can act as radiosensitizer to enhance the DNA damage by X-ray emitted from ^{103}Pd. In recent years, AuNPs have been proposed as novel radiosensitizing agents[121, 191, 215-218], as it was discussed earlier. The main mechanism of radiation induced cell death is DNA damage mediated by reactive oxygen species (ROS) formed from the radiolysis of water.

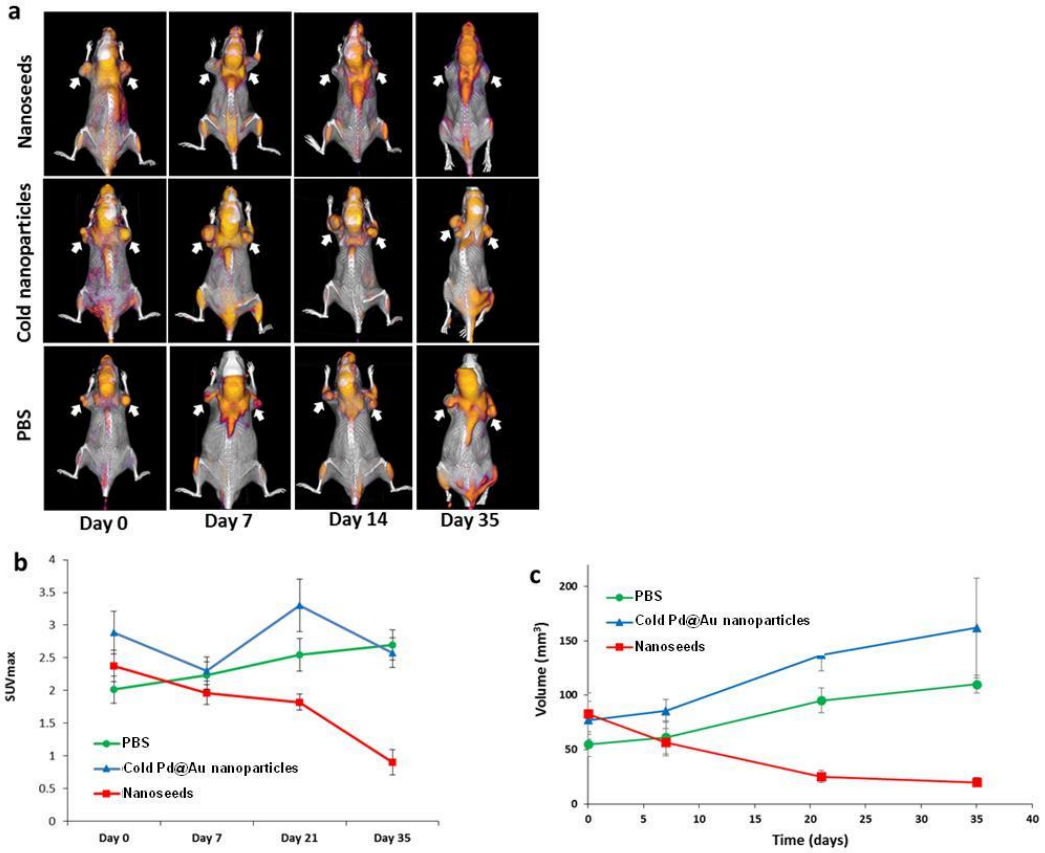

Figure 4-6 Assessment of the therapeutic efficacy of ^{103}Pd@Au nanoseeds in PC3 tumor bearing mice by PET/CT imaging**.** (a) Serial FDG-PET/CT images acquired at 0, 7, 21, and 35 days post intratumoral injection of PBS (upper panel), cold Au@Pd nanoparticles (middle panel), and hot ^{103}Pd@Au nanoseeds (lower panel). A significant tumor FDG uptake reduction was observed in the treatment group with ^{103}Pd@Au nanoseeds as compared to that in the PBS and cold Au@Pd nanoparticles treated groups. White arrows indicate tumor sites. (b) Quantitative PET analysis (SUV_{max} values versus time), (c) Comparative tumor volume changes determined by CT scan analysis (mean ± SEM).

Computational studies have previously demonstrated that AuNPs, at concentrations considered achievable in vivo (7 mg/gram of tumor tissue) can enhance the radiation dose significantly at both macroscopic and microscopic levels throughout brachytherapy using low energy photon sources[115, 219]. Correspondingly, Roeske et al. [220]has done a thorough modeling investigation on the combinations of different nanoparticles (with atomic numbers ranging from 25 to 90) and radiation sources (external radiation sources in the kilovoltage range of 50-140 KVp and megavoltage range of 6-25 MV, and internal brachytherapy sources of ^{125}I, ^{103}Pd, ^{198}Au, and ^{192}Ir) to find the optimal dose enhancement condition. They have concluded that low energy X-rays (5-140 KVp) and LDR brachytherapy (^{125}I and ^{103}Pd) sources would provide the highest degree of dose enhancement when coupled with high atomic number (z>70) nanoparticles.

The more pronounced dose enhancement by low energy brachytherapy sources, particularly ^{103}Pd in comparison to ^{125}I and ^{169}Yb, has also been reported in a theoretical work on the application of AuNPs as vasculature disrupting agents during brachytherapy[221]. Besides, a recent comparative Monte Carlo study on the dose enhancement during external beam radiotherapy and brachytherapy in tissues loaded with different AuNPs concentrations indicated more significant radiosensitizing effects of AuNPs for brachytherapy than for external radiotherapy[29]. In addition, the results of another Monte Carlo simulation study on the dose enhancement effect of AuNPs for photon-emitting brachytherapy sources of ^{125}I, ^{169}Yb, ^{103}Pd, and ^{192}Ir have shown that larger AuNPs (diameter 100-200 nm) have a larger dose enhancement effect[30].

In overall, the recent theoretical and experimental works have indicated the high promising potential of AuNPs as radiosensitizing agents during brachytherapy. It has been addressed that because the common permanent brachytherapy sources deliver their dose in a lingering fashion, the nanoparticles would be required to be localized within the tumor for a significant period of time to achieve the calculated dose enhancements. This in turn would

bring about a demand of continued release or multiple injections of the nanoparticles, which can cause technical challenges. However, in nanoseeds-based brachytherapy, since the radioactive sources are attached onto the AuNPs dwelling at the targeted site, this concern will be eliminated. Moreover, the radiosensitizing effect of Au core of the nanoseeds provides a possibility to combine nanoseeds-based brachytherapy with EBRT to achieve optimum therapeutic outcome. If the internal radiation therapy cannot eradicate the tumor with the radiation from the nanoseeds, the AuNPs that have still remained inside the tumor whit significantly reduced volume can serve as radiosensitizers for the subsequent EBRT at much lower doses to completely eliminate the tumor.

4.5 In vivo toxicity studies

Liver and kidney are two key organs that are involved in uptake and localization of gold nanoparticles based delivery systems, and hence are first line of vital organs that may be affected by the ^{103}Pd@Au nanoseeds radiotherapy. Biocompatibility is a vital function that must be completely established to tag Generally Regarded as Safe (GRAS) tag for the successful transformation of any developed therapeutics to clinic.

Toxicity of ^{103}Pd@Au nanoseeds based radiotherapy was assessed and compared with control as well as cold nanoparticles treated groups. Briefly, PC3 tumor-bearing mice were divided in three groups (n=5). Group-I was treated with PBS pH 7.4, while group-II and II comprised of animal subjects treated with cold Au@Pd nanoparticles and nanoseeds treated animals. Following treatments, complete blood analysis**,** Alanine transaminase (ALT)**,** Aspartate transaminase (AST), Blood urea nitrogen (BUN) and creatinine levels were monitored at 10 and 30 d.p.i.

BUN is a common blood test to reveal how well kidneys and liver are working. A BUN test measures the amount of urea nitrogen in the blood. A higher BUN level indicated

abnormality in kidneys or liver. BUN test performed on control, cold nanoparticles treated group as well as nanoseeds treated groups showed an insignificant change (Figure 4-7a) in blood associated nitrogen suggesting the therapy to be eliciting no side effects on liver or kidney.

Creatinine is removed from the body entirely by the kidneys and determination of creatinine levels in blood can clearly reveal how well kidneys are working. If kidney functions abnormally then creatinine level increases in the blood due to less release of creatinine through urine. Hence, kidney function as additionally assessed by determining the creatinine levels in the blood. Creatinine levels in nanoseeds treated animal subjects was found to be of similar to that of control subjects. This outcome is in agreement with BUN assay that confirms that nanoseeds based radiotherapy elicits no kidney related toxicity.

AST is an enzyme that helps metabolize alanine, an amino acid. An increase in AST levels may indicate liver damage or disease. AST levels in nanoseeds treated groups increased 10 d.p.i and 30 d.p.i. (Figure 4-7); however, this increase was found to be age related as similar trend of AST levels was found in both control, cold nanoparticles treated groups. To further confirm liver functioning ALT assay was also performed.

ALT is an enzyme found in the liver that helps the body metabolizes protein. When the liver is damaged, ALT is released into the bloodstream and levels increase. No notable change in ALT level was found in nanoseeds treated groups 10 d.p.i and 30 d.p.i., and the levels were found to be similar to that of untreated control groups at all assessed time points (Figure 4-7d). 10 d.p.i, no significant alternation in ALT level was found in nanoseeds treated group (25.17±3.90 U/L) compared to control (26.0±6.71 U/L) and cold nanoparticles treated group (28.27±9.6 U/L) treated subjects. Furthermore, similar ALT levels were observed in nanoseeds treated groups 30 d.p.i that confirmed that no immediate or delayed liver toxicity is associated with nanoseeds based radiotherapy.

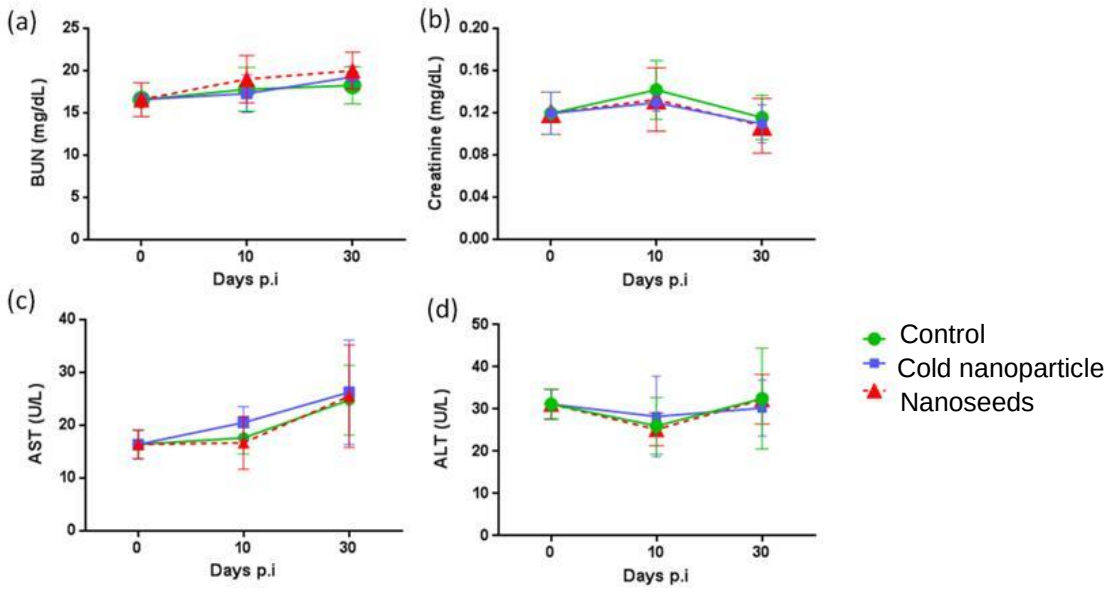

Figure 4-7 (a) BUN, mg/dl, (b) creatining mg/dL, (c) AST, U/L, and (d) ALT, U/L levels in control, cold nanoparticle treated and nanoseeds treated mice.

The complete blood count (CBC) is serving as a major tool to aid diagnosis and monitor disease progression as well as therapy related toxicity. CBC analysis was done on control, cold nanoparticles and nanoseeds treated groups. Red blood cell (RBC) count as well as mean hemoglobin volume per RBC (MCH) remains unaffected throughout the study suggesting that the therapy is not resulting into any hemolytic effect.

Notably, in ^{103}Pd@Au nanoseeds treated group initially reduced the white blood cell (WBC) count 10 d.p.i. (Figure 4-8), which is common to all radiotherapies. However, the effect was found to be reversible, while recovering the normal WBC count to normal 30 d.p.i. Similar effect was observed in case of platelet counts, which also decreased following the nanoseeds implantation and recovered to same level that of control 30 d.p.i (Figure 4-8). Basophil count in control and nanoseeds treated group was found to be insignificantly differing from each other at

0, 10 and 30 d.p.i., indicating that the fluctuation is related to the cancer and not the therapy. After nanoseeds implantation, neutrophil count increased, while eosinophil count decreased initially after 10 d.p.i compared to control, which is an inherent side effect of radiotherapy. However, this was found to be temporary and started to regain to original value when measure 30 d.p.i.

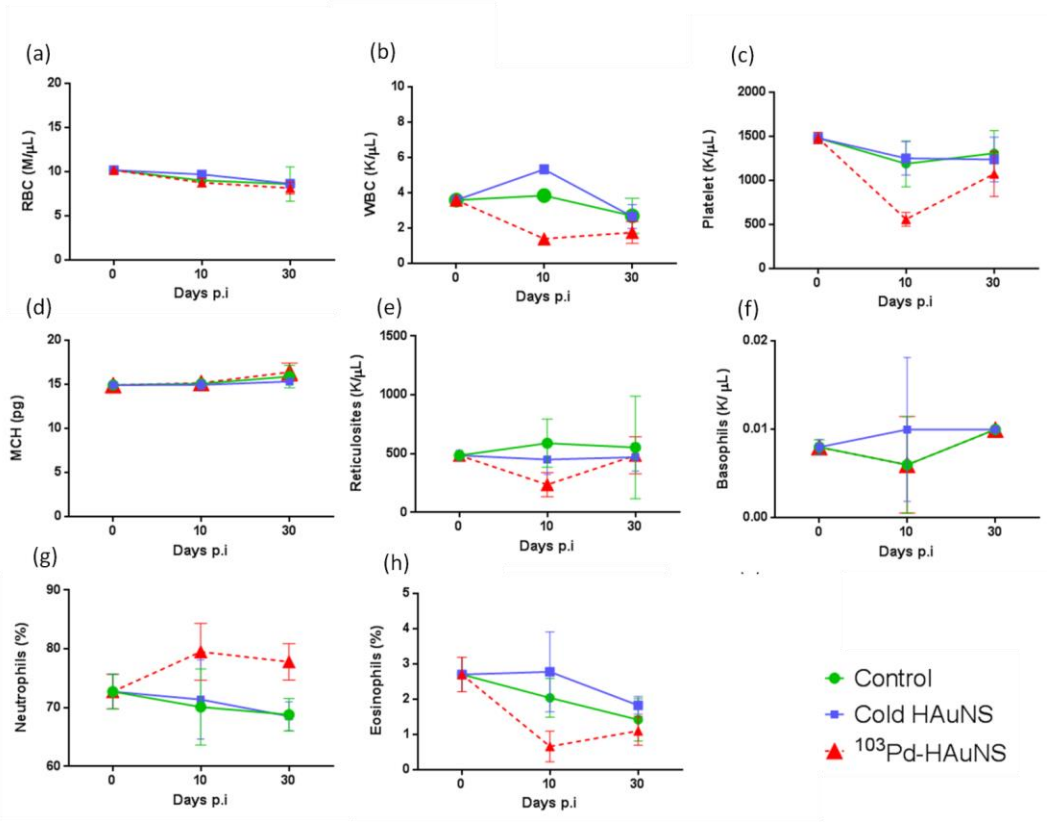

Figure 4-8 (a) RBC m/µL, (b) WBC, K/ µL, (c) platelet count, K/ µL, (d) MCH. Pg, (e) reticulosites, K/ µL, (f) basophils, K/ µL, (g) Neutrophils, %, (h) Eosinophils, % in control, cold nanoparticles treated and nanoseeds treated mice.

4.6 Ex vivo biodistribution study

4.6.1 Ex vivo biodistribution study methods

The biodistribution of the nanoseeds were further investigated by a parallel *ex vivo* assay. At 1 day, 1 week, 2 weeks, 3 weeks, and 5 weeks after the injection of ^{103}Pd@Au nanoseeds, three mice were sacrificed and the desired organs including blood, heart, lung, muscle, bone, fat, liver, spleen, kidney, stomach, small intestine, large intestine, brain, tail, and tumor were collected, weighed and transferred to 20 ml vials. To measure the radioactivity associated with each organ, the activity of each vial was measured in a γ-counter (Perkin Elmer 2480 Wizard) and recorded as counts per minute. Then, aqua regia was added to the vials and left overnight to digest the organs. After 24 h, the aqua regia is boiled off at 150^{0}C. After boiling, 10 ml of 1% HCL solution was added to vials, in which they were then sonicated for 30 minutes. The Au and Pd concentration were then measured in an inductively coupled plasma mass spectrometer (ICP-MS, Agilent 7700x). The measurement was repeated at least three times for each sample.

4.6.2 Ex vivo biodistribution measurement results

At different time points during our study, three mice treated with nanoseeds were sacrificed and the organs of interest were excised, weighed, and then measured for radioactivity by a γ-counter. Thereafter, the tissues were dissolved using aqua regia and processed with ICP-MS to measure their Au and Pd content. Figure 4-9 shows the radioactivity of the resected organs measured by the γ-counter. There is a good consistency between the γ-counter and ICP-MS results (Figure 4-10, no statistically significant difference, $p = 0.88$), indicating that the radioactive isotopes of ^{103}Pd stayed with the nanoseeds during the five weeks of the therapeutic study. The *ex vivo* biodistribution study demonstrated that 95.19 ± 0.94 % of the nanoseeds remained inside the tumor, while 3.31 ± 1.11 % and 0.39 ± 0.24 % went to the liver and spleen,

respectively. No meaningful uptake was observed in other tissues. It is clear that the tumor uptake was maintained essentially the same (p = 0.35) over the five weeks of the study.

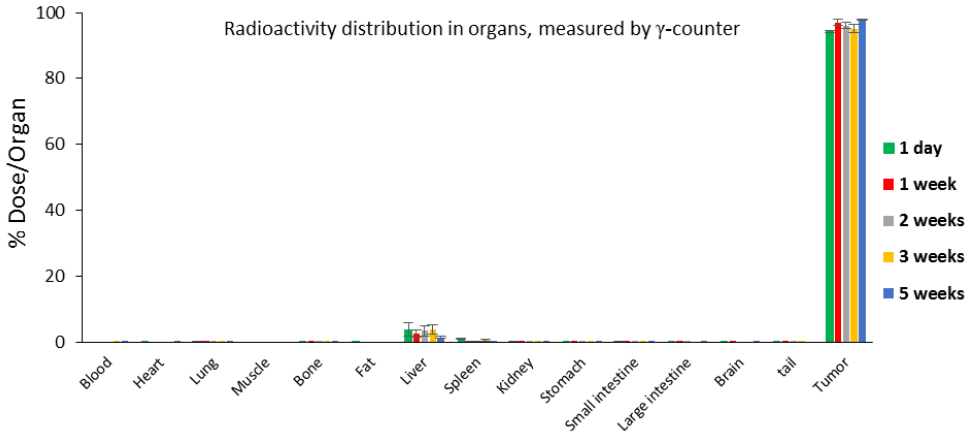

Figure 4-9 Radioactivity of dissected organs measured by a gamma counter (means ± SEM).

The radioactive nature of brachytherapy requires a close to 100% retention rate of the administered dose inside diseased sites. The observed high retention of nanoseeds in tumor sites meets this essential requirement, showing a promising potential for the clinical translation of this approach. Because these nanoseeds are not functionalized, such remarkable high retention rate likely results from their relatively large size (~150 nm). It has been well documented that a majority of gold nanoparticles after intravenous injection accumulate in liver and spleen if their size is bigger than 10 nm[222]. In this work, very small amount of nanoseeds with negligible radioactivity was found in liver and spleen, indicating that the diffusion of nanoseeds into the blood stream is mostly prevented. Of note, a retention rate of 71% in tumor

sites was reported for functionalized ^{198}AuNPs with a diameter of 50 nm after intratumoral injection[223]. It might not be surprising that >95% retention rate was achieved for gold nanoparticles with the size larger than 150 nm. In this regard, a narrow size distribution could have played a crucial role as well. The unique bubble template synthesis method used in this study can produce monodispersed nanoparticles with a >100nm diameter, which is another important advantage of our fabrication process.

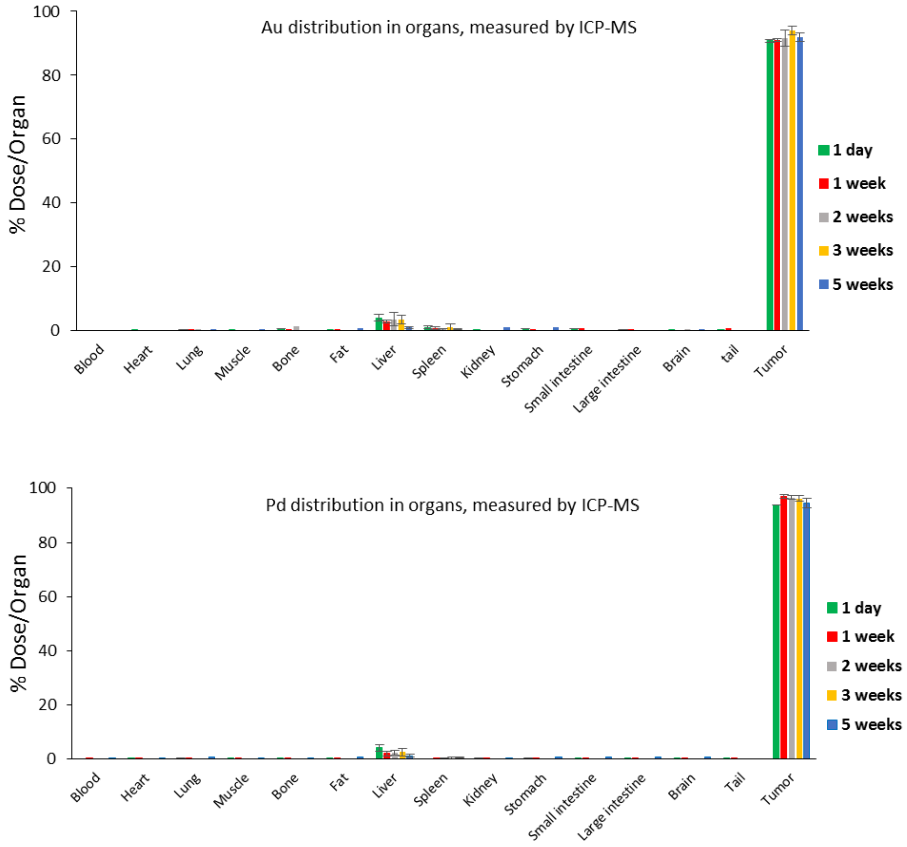

Figure 4-10. Retention of (a) Au, and (b) Pd content measured by ICP-MS in different organs of the mice from 1 day to 5 weeks post-injection of the nanoseeds (means ± SEM).

4.7 Prospective clinical applications and practical significance of nanoseeds

Nanoseeds-brachytherapy can provide an easy way to differentiate the radiation dosage by inject different amount of the nanoseeds solution. Currently, the differentiation is only achieved by controlling the distance from the implant. More importantly, nanoseeds-brachytherapy could dramatically expand its applications. It would enable the treatment of much smaller tumors and the procedure can be performed intraoperatively when optimal surgical resection is not possible. It was discussed that the size of nanoseeds should be maintained reasonably large so as to prevent these radioactive particles from diffusing off the target. This is well achieved by our invented nanoseeds. The tumor retention of radioactive AuNPs in a similar study[39] was only around 70% at one day after intratumoral injection, whereas the nature of brachytherapy requires near 100% retention of radioactive source in its entire activation process.

The other two relative studies[39, 41] on radioactive AuNPs for internal radiotherapy of prostate and breast cancers used targeting AuNPs as a general strategy to increase their retention in the injection site to decrease the systemic toxicity, and their attachment to cancer cells to increase the therapeutic outcome. However, one might wonder whether there has been any benefit in using targeted AuNPs for this specific type of treatment. As a matter of fact, the results of Yook et al. have indicated that there was no difference between the therapeutic efficacy of the targeted and non-targeted ^{177}Lu-AuNPs for brachytherapy of breast cancer. Indeed, they stated that the increased diffusivity of the non-targeted ^{177}Lu-AuNPs may allow for smoothing of the dose distribution, theoretically improving long-term impacts. Moreover, the authors concluded that “non-targeted gold nanoseeds would broaden the approach to tumors expressing many different phenotypes”. In addition, generally speaking, non-targeted agents are much easier to implement in the clinic, as some complex steps in the process will be eliminated[224].

It is worth noting the targeting of radioactive nanoparticles from a big-picture point of view. Brachytherapy intrinsically does not require the close proximity of the radiation source to the nucleus of cancer cells. As of now, the clinically available permanent brachytherapy seeds have millimeter size-range, and are implanted within the tumor discreet from each other at predefined distances. The radiation source is therefore strong enough to kill cancer cells within a micro and macro scale distance. On the other hand, targeting radioactive AuNPs to enhance their attachment to cancer cells and increase their cellular internalization would basically alter the nature of this internal radiotherapy from “brachytherapy” to “systemic radiotherapy”. It must be considered that targeting is an essential part of systemic radiotherapy as the individual radiopharmaceuticals usually do not have high loads of radioactive substances. In contrast, AuNPs with high surface area can be loaded with such amount of radioactive materials that give them enough lethal effect for a large number of cells in their vicinity. In addition, the radioisotopes commonly used in radiopharmaceuticals are particle-emitters rather than photon-emitters. In contrast to photons, particles usually have very short distance in biological tissues so they have to be close to cells to be effective. Thus, targeting AuNPs for brachytherapy purpose might be perceived as a “strategic” misconception.

To evaluate the therapeutic response to the treatment, the other studies used precision caliper measurement. However, this is not a feasible technique in clinical trials, and consequently other methods should also be used in real application to monitor the treatment outcome. Here, in our study, we used ^{18}F-FDG PET/CT imaging to monitor the tumor metabolism, which provided a more reliable and accurate picture of the disease status. While the applications of CT and MRI in breast cancer have been limited to date, they are commonly in clinical use for prostate cancer treatment. The intratumoral injection of radiotherapeutic agents, in theory, should have big promise in many cancer sites. Anywhere that traditional brachytherapy is performed should also be accessed for intratumorally injection of brachytherapy nanoseeds as well. However, it should be noted that the relative simplicity of

intratumoral injection in a xenograft model may not copied in the clinical setting[224]. For this reason, image guidance will likely be required for proper injections to be performed, because clinical tumors are normally not as superficial. CT, MRI, ultrasound, and PET are the common imaging modalities that used during clinical radiotherapy in oncology centers. Hence, imaging-guided brachytherapy may be needed for real clinical applications of nanoseeds, which derived us to add MRI-visibility to our synthesized nanoseeds (next chapter).

Chapter 5 Magnetic nanoseeds for MRI-guided brachytherapy

5.1 Introduction

The term “theranostics” was coined to define ongoing efforts in clinics to develop more specific, individualized therapies for various diseases, and to combine diagnostic and therapeutic capabilities into a single agent. Thus, theranostic nanomedicine is emerging as a promising therapeutic paradigm. It takes advantage of the high capacity of nano-platforms for both imaging and therapeutic functions [225].

Magnetic resonance imaging (MRI) is an ideal imaging modality for image-guided brachytherapy, as it provides outstanding visualization of pelvic and prostate anatomy. Image-guided brachytherapy may provide better dose distribution to the target tumor and reduced dose volumes to surrounding healthy tissues when compared with image-guided IMRT and IMPT. Also, the use of imaging techniques, such as ultrasound, CT and MRI for treatment planning, has led to improved visualization of the tumor and surrounding organs.

Regions within the prostate that have initial tumor visible on imaging may be the most likely site of local recurrence after standard external beam radiotherapy. Therefore, an intra-prostatic tumor-targeted dose escalation approach may improve the therapeutic ratio and minimize normal tissue toxicity, while improving local tumor control. MRI has the potential to better distinguish macroscopic cancer within the prostate compared to other imaging modalities. Using MRI to direct brachytherapy may allow dose escalation, normal tissue avoidance, and represents a novel imaging and radiotherapeutic approach to personalized medicine. Hence, the development of magnetic nanoseeds detectable by MRI can provide excellent opportunity to establish highly efficacies theranostic nanoseeds for image-guided brachytherapy.

The recent development of molecular and cellular imaging, which enables visualization of the disease-specific biomarkers at the molecular and cellular levels, has led to increased recognition of nanoparticles as MRI contrast agents, where iron oxide nanoparticles, with T_2

MRI contrast, has been the prevailing and only clinically used nanoparticle agents. However, as a result of the tremendous progress in nanotechnology, many researchers have recently developed new nanoparticulate MRI contrast agents that have further improved contrasting abilities and have extra functions. To produce efficient T_2 contrast agents, the magnetic properties of the nanoparticles have to be controlled through the designed control of the intrinsic and extrinsic material properties. Magnetic nanoparticles with high magnetization, such as Co-based nanoparticles, have recently been synthesized to develop new MRI contrast agents with improved relaxation properties and biocompatibility [226].

Meanwhile, magnetic multi-components nanostructures (also called nanocomposites) have been fabricated by physical (e.g. spray drying, co-evaporation) and wet-chemical methods. For wet-chemical synthesis, there are three different strategies; namely separate step synthesis, sequential step synthesis, and simultaneous synthesis. In the sequential synthesis strategy, one component of the magnetic nanostructures is synthesized first, and then the second component is directly synthesized in the presence of the first component. This strategy is often employed to fabricate metallic core–shell NPs as well as magnetic-core@polymer NPs [227]. Several wet-chemical methods have been used to synthesize cobalt crystals with different morphologies, including pyrolysis, solvothermal and hydrothermal decomposition, microfluidic synthesis, modified polyol processes, and template-based methods. It has been reported that liquid-phase reduction methods are relatively simple, inexpensive, quick to implement, not requiring special equipment, and yield controllable morphologies and sizes, all of which being desirable qualities for large-scale production [228]. A synthesis method called “redox-transmetalation” has been used to produce superparamagnetic core-shell NPs with Co at the core and an outer shell of Au, Pd, Pt, or Cu [229]. Although the transmetalation strategy has the capability of making versatile core-shell NPs, it needs special condition and equipment (like argon gas atmosphere), high temperature, and long time (several hours). Moreover, as organic

compounds are essentially used in this method, producing NPs with clean surface and free of by-products for biomedical applications by transmetalation impose extra effort and cost.

Electroless cobalt deposition has been mostly used in the industry as a method for bulk production of cobalt thin films used in microelectronic devices. Since the crystallinity and microstructure of the deposited cobalt would greatly affect its magnetic and mechanical properties, which are in turn crucial for its functionality, extensive research has been conducted on the electroless deposition process to yield cobalt thin films with desired qualities. However, the use of electroless cobalt deposition to make nanoparticles has been limited as aggregation of them encountered as a restricting issue. Interestingly, because the HAuNPs and nanoseeds are produced while they are anchored to the inside of the AAO nanochannels, electroless cobalt deposition can be used to coat them in a similar fashion to thin film production.

Due to the magnetic susceptibility of cobalt, co-coated Au@Pd[103] nanoseeds and their accumulation at the therapeutic site can be easily monitored by applying an external magnetic field, opening up the possibility of a precise MRI-guided nanoseeds-brachytherapy. On the other side, because cobalt is a reactive metal that can cause toxicity in the body, we further added another layer of Au to make magnetic nanoseeds with inert biocompatible surface. The last Au layer was added through a galvanic replacement reaction between the cobalt coating and an aqueous solution containing Au ions. The success of this process will prove that this strategy can also be used to incorporate the medical radioisotopes that their reduction potential are higher than cobalt. Thus, our nanoparticle radiolabeling strategy (explained in the previous chapter) through galvanic exchange can be applied to a larger number of radioisotopes, as the reduction potential of cobalt is less than that of copper. This makes it even possible to incorporate of Cu radioisotopes, such as ^{64}Cu, into nanoseeds, which can make them traceable by PET imaging.

5.2 Design and synthesis of magnetic nanoseeds

5.2.1 Electroless deposition of cobalt

Electroless metal depositions are electrochemical processes that can be considered as the combination of two partial electrochemical reactions; the cathodic reduction of metal ions and the anodic oxidation of the reducing agent. The oxidation of a substance is identified as the loss of electrons, while the reduction is recognized by a gain of electrons. Both cathodic and anodic partial reactions involve at least two elementary steps; formation of electroactive species and then the charge transfer from the catalytic surface to the electroactive species. Thus, catalytic surface generally plays essential role to start any electroless reaction. However, electroless deposition can proceed by autocatalytic mechanism, which means that the deposited metal itself can act as the catalytic surface for the electrochemical reactions to continue. The overall reaction must be conducted in such a way that a homogenous reaction between the metal ions and reducing agents, in the bulk of the solution, is suppressed. Therefore, a complexing agent (stabilizing agent) is usually used in the electroless deposition process.

As such, electroless cobalt deposition process is consisting of anodic oxidation of proper reducing agent and cathodic reduction of Co^{2+} ions occurring simultaneously on the same cobalt surface. The electrons in anodic oxidation of reducing agent are transferred through the metallic surface to adsorbed Co^{2+} ions, and the autocatalytic deposition of Co takes place. Again, since the deposit catalyzes the reduction reaction, the term “autocatalytic” is used to describe the plating process. In addition to being catalyzed by the forming solid cobalt, the reduction reactions in electroless deposition of cobalt can be catalyzed by some noble metals. For example, the reduction reactions by boron hydride are catalyzed by palladium, platinum and to a lesser degree by gold, silver, and copper [230]. It should be noted that pure cobalt coatings are rarely obtained by this process, as some elements from the electroless plating bath (usually

provided by the reducing agent itself) would co-deposit with cobalt, which in turn would affect the properties of the final deposited product.

There are four reducing agents that have been widely used for cobalt electroless deposition; hypophosphite, Boranes/borohydrides, hydrazine, and formaldehyde. All these reducing agents have similar structure by containing reactive hydrogens. In other words, the reduction of cobalt is a result of the catalytic dehydrogenation of the reducing agents. Boranes amine (e.g. DMAB) and borohydrides (e.g. NaBH4) have an advantage over the most widely used alternative reducing agent, hypophosphite, of being catalytically oxidized at technologically important substrates such as copper without the requirement for substrate palladium activation, which reduces the number of processing steps and can aid selectivity. Furthermore, the boron content in deposits is significantly lower than the phosphorus co-deposited from hypophosphite-based baths, leading to purer deposits of the desired material. Boranes and borohydrides are also a nontoxic alternative to formaldehyde and hydrazine [231]. Hence, in this study we used DMAB as reducing agent to reduce cobalt ions from an electroless plating solution.

5.2.2 Synthesis methods and materials

All chemicals used in this experiment were analytical grade and used without futher purification. A typical electroless plating bath consisted of an aqueous solution of 0.089 M cobalt sulfate heptahydrate ($CoSO_4.7H_2O$), 0.21 M dimethylamine borane (DMAB), and 0.085 M sodium citrate ($Na_3C_6H_5O_7$). The chemical were mixed under vigorous stirring, and then heated to 45 ^oC and maintained at that temperature by keeping the solution on a hot plate. Before starting the deposition, the pH was adjusted to 9.5 by dropwise addition of 5 M NH_4OH. The solution pH was monitored throughout the entire deposition process by a pH-meter and readjusted to 9.5 whenever it fell off 9.45. After the solution became ready, the stirring was stopped, and an AAO membrane containing Au@Pd NPs was dropped in the solution. The membrane was left in the solution for a certain time (5 - 60 min), depending on the desired

cobalt coating thickness. The synthesis progress can be visibly monitored by the evolution of gas microbubbles from the membrane.

After electroless cobalt coating, the membrane was removed from the solution and washed with DI water. Using a vacuum setup, 0.0025 M $HAuCl_4$ solution was forced to pass through the membrane channels. Then, the membrane was immersed and left submerged in 5 ml of 0.0025 M $HAuCl_4$ for 20 min. Finally, the membrane was washed and dissolved with 2M NaOH solution. The released NPs were washed at least three times with cycles of centrifuge and ultrasound-dispersion.

5.2.3 Chemical reactions of the cobalt electroless deposition

In this study, DMAB was used as the reducing agent to deposit cobalt from cobalt ions from an aqueous solution. The DMAB is a covalent compound (in contrast to borohydrides such as $NaBH_4$ that are ionic), so it would not ionize. However, the boron atom has a greater affinity for the electrons than the nitrogen and the bond between them is therefore polar. This polarity makes DMAB soluble in water, and plays an important role in the reactions of this covalent compound. As can be seen from Figure 5-1(a), the electrons are displaced toward boron atom due to its higher electronegativity. The three active hydrogens bonded to the boron atom theoretically can reduce three cobalt ions for each DMAB molecule consumed [232].

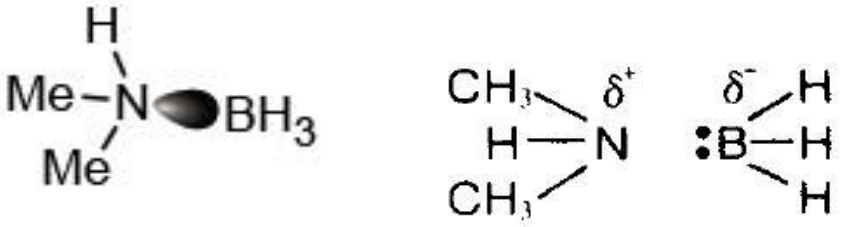

Figure 5-1(a) Chemical structure of DMAB molecule, and (b) broken N-B bond in DMAB molecule and the resultant electron density over N and B atoms.

When DMAB is added to the plating bath, it can be either consumed by hydrolysis with water, or participate in the reduction reaction of cobalt ions, through both of which hydrogen gas will evolve. The role of DMAB can significantly be altered by the pH of the electroless plating solution. It has been suggested that in strong alkaline solutions, DMAB will exist as hydroxytrihydroborate ion ($BH_3(OH)^-$), which may undergo oxidation with maximum coulombic efficiency on a noble metal surface in base according to the reaction [231].

$$BH_3(OH)^- + 6OH^- \rightarrow B(OH)4^- + 3H_2O + 6e^- \qquad 5\text{-}1)$$

In addition to the above useful reaction, DMAB can be consumed by a wasteful hydrolysis in an alkaline solution as follows:

$$(CH_3)_2NHBH_3 + OH^- + H_2O \rightarrow (CH_3)_2NH + BO_2^- + 3H_2 \qquad (5\text{-}2)$$

Some theoretical expressions have been proposed for the reduction of nickel ions with DMAB, which can be also described by the following possible chemical reactions for the reduction of cobalt ions:

$$3Co^{+2} + (CH_3)_2NHBH_3 + 3H_2O \rightarrow 3Co^0 + B + (CH_3)_2NH_2^+ + B(OH)_3 + 3H^+ \qquad (5\text{-}3)$$

or alternatively :

$$[CoL_m^{-(n-2)}] \leftrightarrow [Co^{+2} + mL^{-n}] \quad 5\text{-}4)$$

$$2[(CH_3)_2NHBH_3] + 4[Co^{+2} + mL^{-n}] + 3H_2O \rightarrow Co_2B + 2Co^0 + B(OH)_3 + 2[(CH_3)_2NH_2^+] + 6H^+ + 1/2H_2$$

where $[CoL_m^{-(n-2)}]$ and mL^{-n} denotes the cobalt complex and the "free" complexing agent, respectively. Sodium citrate has the role of complexing (stabilizing) agents in the used plating bath. However, the reaction mechanism needs to match with the experimental observations. During the electroless deposition, it was observed that remarkable amounts of hydrogen gas were evolved. Moreover, the pH of the plating solution would slightly decrease as the deposition proceeded. The evolution of hydrogen gas is only included in the reaction 4-2.

On the contrary, the reported experimental results for reduction of nickel ions by DMAB did not support the theoretical equations. Consequently, it was suggested that nickel deposition with DMAB is dependent on the adsorption of the reducing media on the catalyst surface, followed by cleavage of the N-B bond of the adsorbed amine borane [232]. The adsorption step is consistent with the polar nature of the DMAB molecule, and emphasizes the catalyzing role of the palladium shell during the electroless cobalt deposition in the present experiment. Accordingly, it can be supposed that first the N-B bond cleavage occurs on the Pd surface, and then the hydrolyzed cobalt ions would react with the adsorbed hydrogens. The overall chemical reaction can be expressed as follows:

$$3Co^{+2} + 3R_2NHBH_3 + 6H_2O \rightarrow 3Co^0 + B + 3R_2NH_2^+ + 2B(OH)_3 + 9/2H_2 + 3H^+ \qquad 5\text{-}5)$$

This reaction is more consistent with the experimental observations, wherein significant amount of hydrogen gas were evolved during the reaction while the pH decreased slightly. It also should be noted that during the electroless cobalt deposition, boron is also reduced which co-deposit with cobalt. The co-deposited boron during electroless deposition of cobalt using DMBA as reducing agent (and co-deposited phosphor using hypophosphate as reducing agent) has important effects on the crystal structure, mechanical properties, and magnetic characteristic of the deposited cobalt.

5.3 Morphological and structural characterization

5.3.1 Au@Pd@Co nanoparticles

The SEM images of the synthesized Au@Pd@Co (APC) core-shell NPs are presented in Figure 5-2. The NPs are roughly ~250 nm in size. As can be observed, the cobalt coating has some kind of fractal morphology with a radial distribution over the spherical core-shell NPs. Nanoparticles with similar morphology have been described as "urchin-shaped" [209]. This particular morphology of the deposited cobalt layer can be elucidated by the chemical reactions during the electroless deposition process. As can be seen from the electroless chemical reaction shown in the previous section, hydrogen is formed when iron, nickel, and cobalt metals are reduced by DMAB, boron hydride, and hypophosphite due to simultaneously proceeding the catalytic reaction of reducing agent ion decomposition. The nonequilibrium condition of the reaction involves the rapid reduction of cobalt ions on the catalytic surface of Pd and producing considerable amount of hydrogen gas bubbles. The cobalt reduction reaction continues in the radial direction through the autocatalytic effect of the deposited cobalt and consume the cobalt ions but the release of hydrogen bubbles limit the access of cobalt ions to the sides of the deposited part, and hence, inhibit the lateral growth. It has been stated that the hydrogen generation may be detrimental for the quality of metallic coatings due to nanopores formation [230]. Here, it can be assumed that the overall reaction was stopped before the pores formation become complete.

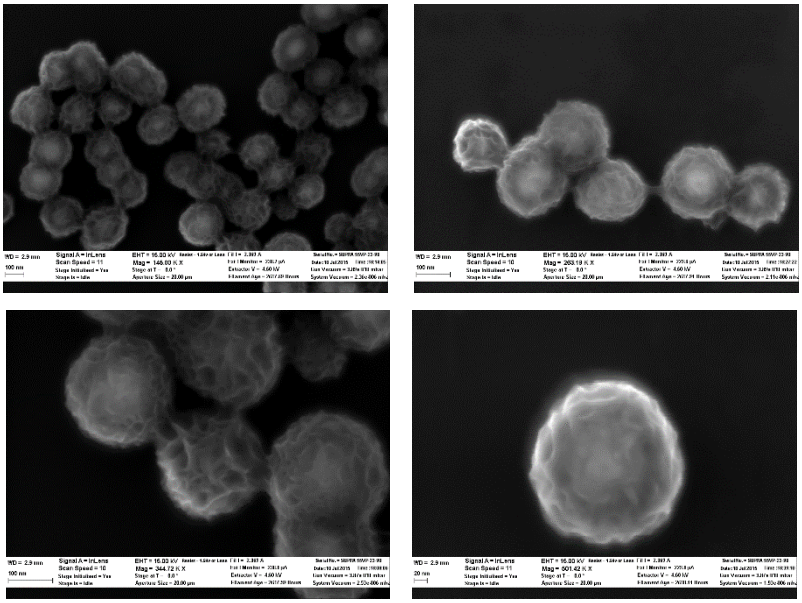

Figure 5-2 SEM images of APC NPs at low to high magnifications.

The transmission electron microscopy (TEM) images of the APC NPs with different magnifications are shown in Figure 5-3. A distinct contrast of the core and shell parts can be observed clearly, where the dark cores are Au@Pd NPs and the bright shells are cobalt. From the TEM images, the average thickness of the cobalt layers can be determined to be around 70 nm. The high resolution image (Figure 5-3) strongly suggests the deposited cobalt is basically amorphous, as no clear lattice fringe can be seen in the HRTEM image. The formation of amorphous cobalt coating through wet-chemical methods has been reported in other studies as well [233-235]. It has been shown that the nanosize amorphous Co-B alloys can be well crystallized into metallic structure by heat treatment regimens of 673-873 K for 2-3 h [233, 235].

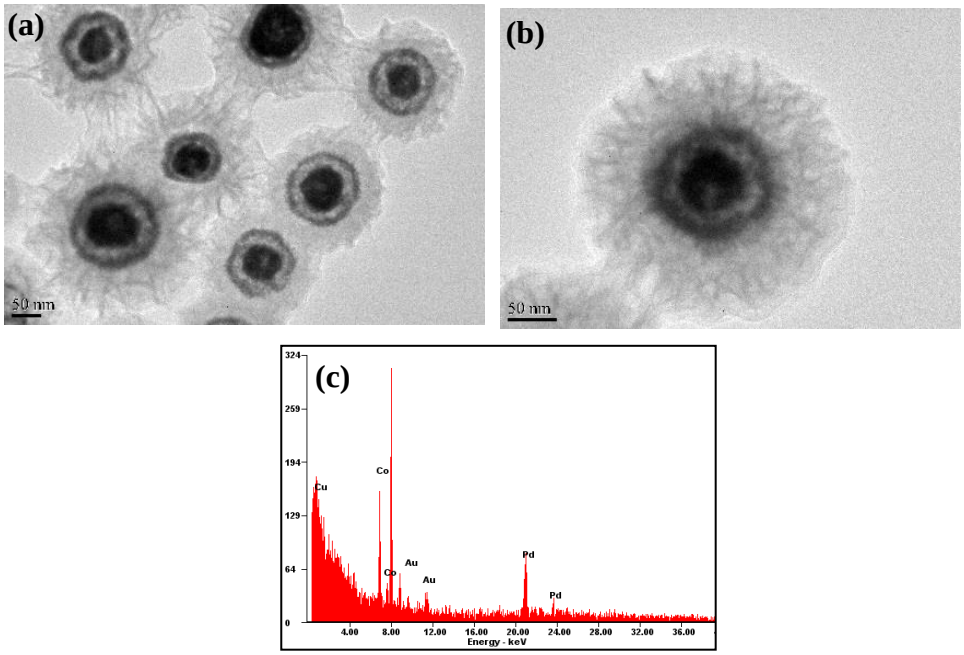

Figure 5-3 TEM images of APC NPs with (a) low, (b) high magnifications and (c) EDX spectrum of the nanoparticles.

Amorphous alloys are materials having a noncrystalline structure that is produced by some form of nonequilibrium processing. Usually, the rapid formation prohibit the development of long-range topological and chemical order in the alloy. Under non-equilibrium conditions, exploiting fast diffusion and chemical thermodynamics, the kinetics of the fabrication process itself can override the tendency for the atoms to order locally the way they do in the equilibrium state. However, in order to stabilize their glassy structure, it is generally necessary to alloy the metallic elements with glass formers such as B, C, Si or P. The absence of long-range order

leaves amorphous materials empty of some microstructural defetcs such as grain boundaries, precipitates, or phase segregation [236].

In case of electroless deposition, it has been emphasized that to form and stabilize the amorphous structure, some metalloids (e.g., B or P) should be incorporated in amorphous alloys [235]. Apart from hydrogen, on the reduction of nickel, cobalt and iron ions by DMAB, boron hydride, and hypophosphite, a various but appreciable amount of boron or phosphorus is deposited together with them. This causes difficulties in crystallization of the metal during deposition, and if the quantity of the above-mentioned non-metals is sufficient, would result in the formation of amorphous metals, essentially alloys of the metal with boron or phosphorus [230].

In the present sudy, amorphous cobalt layer could form due to the nonequilibrium condition of the reaction, and stabalized by boron co-deposited according to the specified chemical reaction (reaction). It has been claimed that the process to form Co–B alloy is very sensitive to reaction conditions; including temperature, rate of reducing agent addition, metal precursor, solution pH, and the presence of other ions. Furthermore, it was reported that the reactions involved are very fast and almost immediate[236]. This seems to be true in our study as well. In many cases, anodic oxidation of a reducing agent is the limiting stage that determines the reaction rate of the electroless plating [230]. However, the catalyzing effect of Pd shell surface in the Au@Pd NPs could drive the instantaneous reaction start in our experiment, leading to the formation of amorphous structure.

The amorphous cobalt layer was further characterized after being annealed under Argon gas atmosphere for 2 h at a temperature of 200 ^{o}C. The TEM images of the cobalt layer after being annealed are shown in Figure 5-4. It can be observed that the amorphous cobalt has partially crystalized as the temperature and time of annealing was not enough to fully crystalize the cobalt layer. The crystal parts of the cobalt layer can be noticed by their lattice fringes.

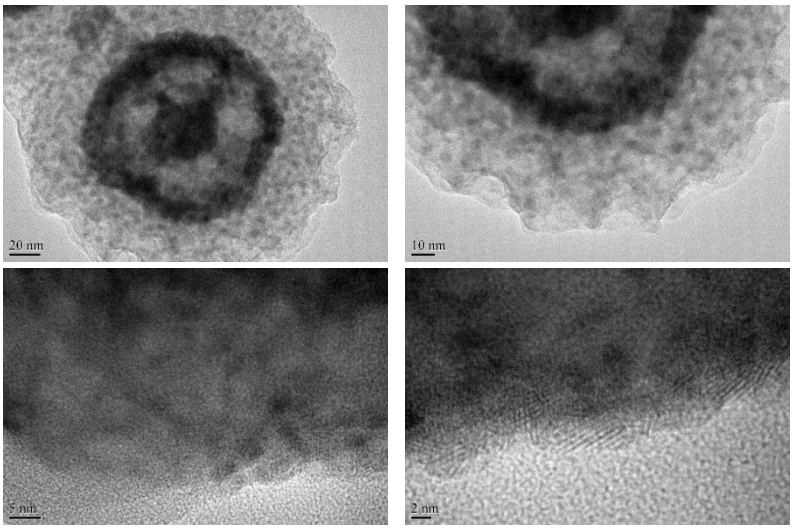

Figure 5-4 HRTEM images of annealed APC NPs at 200 ^{o}C for 2 hours, showing the partial crystallization of amorphous cobalt layer. The crystalized parts can be noticed by the revealed lattice fringes.

5.3.2 Au@Pd@Co@Au nanoparticles

The coating of cobalt nanoparticles with an appropriate shell is likely to overcome the oxidation (and hence deterioration of the magnetic properties) and poor biocompatibility of Co. Therefore, efforts have been made in creating biocompatible cobalt nanoparticles by growing a gold shell [237]. Likewise, here we add another gold layer to the nanoseeds to prevent the cobalt from participating in the chemical reactions inside the body. Figure 5-5 demonstrates the SEM and TEM images of the Au@Pd@Co@Au (APCA) core-multi-shells nanoparticles fabricated by coating APC NPs with gold using $HAuCl_4$ aqueous solution for 20 min. The SEM image of APCA NPs (Figure 5-5 a) shows that they have irregular shapes, with bumpy surfaces. The TEM images show the multi-shell structure of the APCA NPs with brighter areas in between the shells. It should be mentioned that the TEM contrast are coming from the difference between

the Z of metals and the thickness of the sample. Thus, the brighter areas should belong to either lighter materials or porous structure. The HRTEM image of the outermost atomic planes of surface Au clearly shows the lattice fringes, implying to the crystal structure of the gold layer in contrast to the cobalt deposition structure.

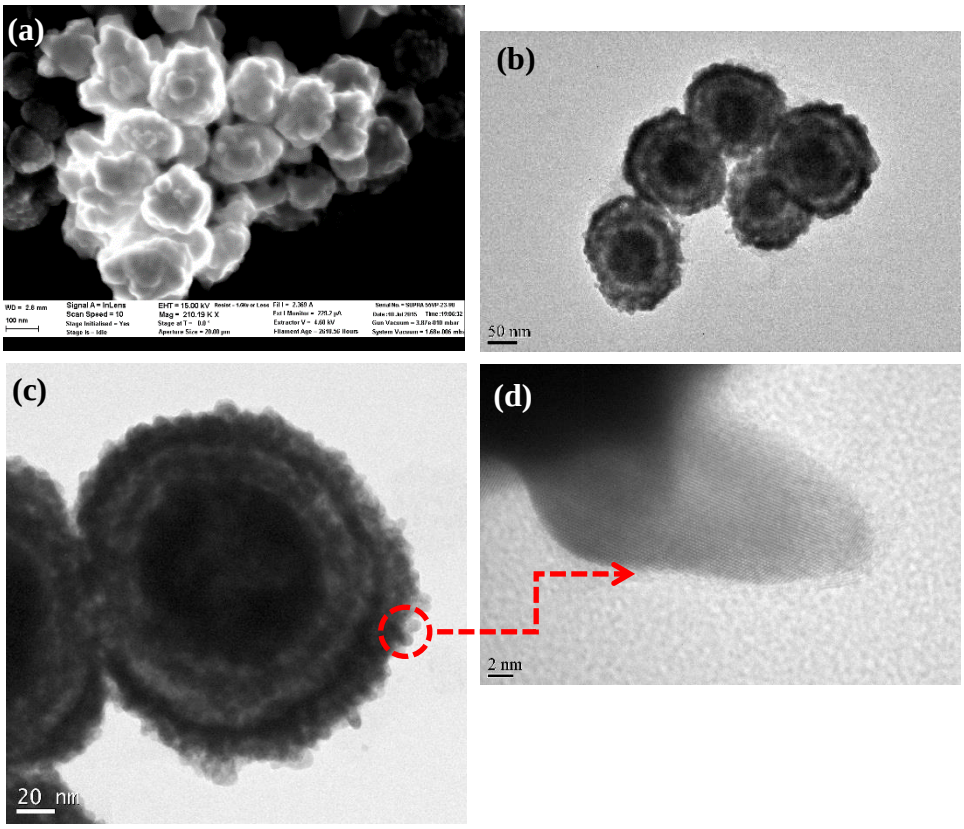

Figure 5-5 (a) SEM image and (b-d) TEM images of APCA NPs.

Galvanic replacement reaction (also known as galvanic exchange) is a redox process, in which one metal is reduced (cathodic half reaction) at the expense of the oxidation of another metal (anodic half reaction). The thermodynamic driving force for this reaction comes from the

difference in the reduction potentials of the two metals involved, wherein the reduction potential of the deposited metal is necessarily higher than that of the sacrificial metal. The reduction potentials of cobalt and gold ions are as follow [210]:

$Co^{2+} + 2e^- \rightarrow Co \quad E^0 = -0.28$ (V vs. SHE, for ideal condition at 25 ^oC and 1 atm)

$Au^{3+} + 3e^- \rightarrow Au \quad E^0 = +1.50$ (V vs. SHE, for ideal condition at 25 ^oC and 1 atm)

Since the redox potential difference between Au and Co is significant, the galvanic replacement reaction between them is thermodynamically favorable. Accordingly, when the AAO membrane containing NPs was added to the aqueous $HAuCl_4$ solution, galvanic replacement was initiated immediately at most cobalt sites in contact with the solution. This leads to replacement of surface cobalt atoms with Au atoms. The covering of Co with Au protects most parts of inner Co layer from more oxidation by a direct redox reaction. However, the galvanic reaction can still continue between the Co inner electrode and the Au outer one through the so-called “pinholes” located mostly at surface defects, in which Co serves as the anode and is oxidized and its electrons are stripped. The released electrons can easily migrate to the surface of the nanoparticles through the Au shell and are captured by $AuCl_4^-$ ions to generate gold atoms that preferentially nucleate and grow on the surface of the template [210].

The APCA NPs were further characterized by scanning transmission electron microscopy and EDS line scan. The results (shown in Figure 5-6) indicate the presence of Au at outer shell, Pd at the inner shell, and all three elements with much less amount at the brighter area of the nanoparticle. Also, it can be seen that the total amount of cobalt is much less than other composing metals, which means most of the cobalt has been replaced with Au atoms during galvanic replacement reaction.

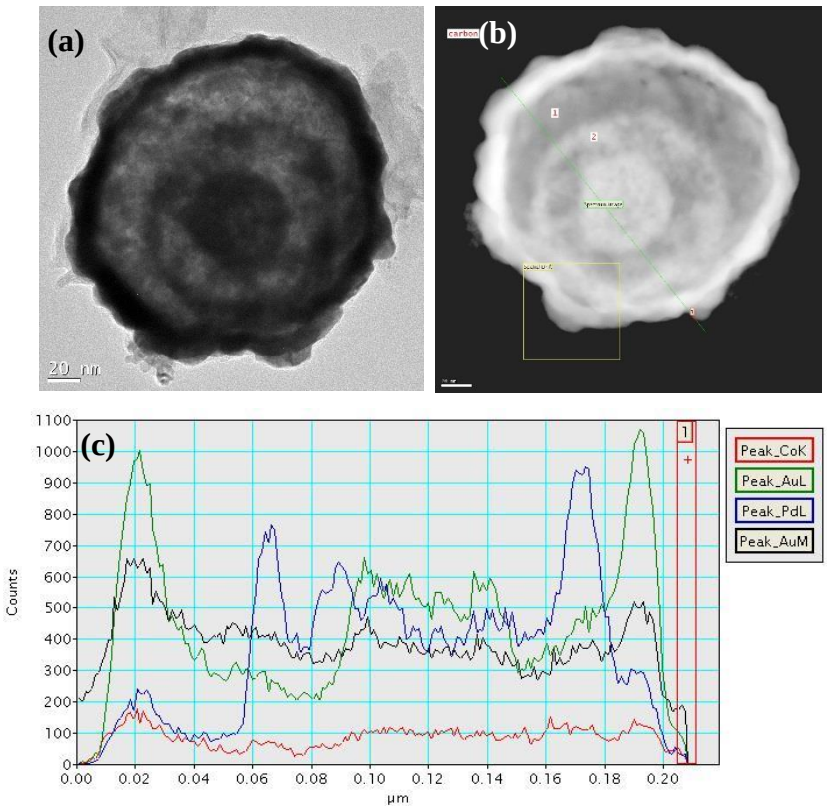

Figure 5-6 (a) TEM, (b) STEM image of APCA NP and (c) their corresponding EDS line scan.

Formation of voids along with remaining unreacted metal cores is well known as an phenomenon for “conversion chemical reactions” of metal NPs that proceed through the Kirkendall effect [209]. Kirkendall effect refers to the result of the difference between the solid-state diffusion rates of two species in a diffusion couple. It is based on vacancy diffusion mechanism, wherein the atomic diffusion occurs through vacancy exchange, so the net directional flow of matter is balanced by an opposite flow of vacancies. These vacancies can coalesce and form pores (or voids), or can be annihilated in microstructural defects such as dislocations and grain boundaries. If the faster-diffusing species are confined into a nanocrystal core, the net rate of vacancy injection should increase markedly, because of the high surface-

to-volume ratio of the particle and the absence of defects in the core. Thus, within the small volume of a transforming nanocrystal, the vacancies can rapidly become supersaturated and are likely to coalesce into pores and/or a single void [238]. This nanoscale Kirkendall effect has been used to produce hollow nanoparticles with complex morphologies [209, 239].

Similarly, directional material flows also result from coupled reaction-diffusion phenomena at solid/gas or solid/liquid interfaces, leading to deformation, void formation, or both during the growth of metal oxide or sulfide films. Again, these voids are usually explained by outward transport of fast-moving cations through the oxide layer and a balancing inward flow of vacancies to the vicinity of the metal-oxide interface [238]. Theoretically, the mobility of reacting species do not have to be markedly different to result in vacancy transport. Placing solid nanocrystals containing one reactant in a comparatively dilute solution creates an additional asymmetry that may favor the creation of hollow structures. The relatively large change in the concentration of the core material between the core and the solution provides a greater driving force for the outward diffusion of the core material.

In our experiment, cobalt cations are dissolved inside the solution by the replacement reaction in the inner parts of the NPs. The ongoing outward flow of cobalt cations through the pinholes on gold shell can result in supersaturation of vacancies, which condensed to form pores. This porous structure in the TEM images appears as the bright area between the palladium and gold shells (Figure 5-6). The dissolution of Co^{+} ions increases the local concentrations of Cl^{-} at the reaction interface, favored by autocatalytic galvanic processes. Hence, the concentration gradient and electrical field drive the outward diffusion of cobalt cations from interior parts of the NPs.

Diffusion processes are known to be enhanced in NPs due to various reasons; the large volume fraction of the interfaces formed in these structures, which provides short-circuit diffusion paths; a high density of defects, such as grain boundaries and vacancies caused by the galvanic replacement; and defects originating from the curvature of surfaces and by

replacement of the capping agents. In those situations the diffusion coefficient at room temperature on a nanoscale should be several orders of magnitude higher than that in bulk-type systems [240].

The formation of porous structure during galvanic replacement reaction between Au and Co can also be examined through a mechanism called “selective etching”. There have been several reports of void formation in multi-metal NPs containing Pt mixed with transition metals where the transition metal (Co or Ni) is removed through selective etching. Nevertheless, the mechanism for dissolving Co or Ni has yet to be fully clarified. It was shown that if Co or Ni diffuses to the NP surface prior to removal by oxidative etching, the remaining nanostructure can be significantly enriched in Pt. In this case, void formation would be driven by the Kirkendall effect. While it seems that the void formation is a result of nanoscale Kirkendall effect, additional studies are still needed to further discern the mechanism of Co or Ni removal [209].

5.4 Magnetic properties of the magnetic nanoseeds

5.4.1 Magnetic anisotropy

Magnetic anisotropy is described when the susceptibility of a material depends on the measurement directions. Due to magnetic anisotropy, the total magnetization moment of a ferromagnetic material (M_s) will incline to lie along a particular direction, called easy axis, which is associated with an energy term, known as anisotropy energy. The anisotropy energy in its lowest order form is given by

$$E_a = K \sin^2\theta \qquad (5\text{-}6)$$

where θ is the angle between M_s and the easy axis, and K is the anisotropy constant.

Magnetic anisotropy arises from different sources, among which two are more important and common; magnetocrystalline anisotropy and shape anisotropy. Only magnetocrystalline anisotropy (or simply crystal anisotropy) is an intrinsic property of materials, while other anisotropies are induced. Crystal anisotropy means that for different crystallographic directions in a crystalline material, the ease of obtaining saturation magnetization is different. The crystallographic directions for which the M_s is obtained most easily in bcc, fcc, and hcp crystal structures are [100], [111], and [0001] (c-axis), respectively. In other words, in these crystal structures, the spontaneous magnetization below Curie temperature (T_c) is aligned to their corresponding easy axes. However, if a magnetic field is applied to a material in a direction other than its easy axis, an energy is required to redirect the magnetization from easy axis to the direction of the magnetic field. This energy translates to crystal anisotropy energy, which for a uniaxial material can be parametrized to lowest order by the anisotropy constant $K = K_1$ (erg per cm^3 or gram of material). The calculated values of K_1 for iron (Fe, bcc structure), nickel (Ni, fcc structure) and cobalt (Co, hcp structure) are 4.8, -0.45, and 45 ($\times 10^5$ erg/cm^3), respectively. Crystal anisotropy physically originates from the coupling of the electron spins, which carry the magnetic moment, to the electronic orbit, which in turn is coupled to the lattice [241].

Shape anisotropy, as another major source of magnetic anisotropy, is based on spatial directions (rather than crystallographic directions), and directly is related to the shape of the material. Accordingly, for a spherical piece of material (even in nanoscale) all spatial directions are basically identical and hence the shape anisotropy will be zero. On the other hand, for a nonspherical piece of material, it is generally easier to induce magnetization along a long direction than along a short direction, as the demagnetizing field is less in the long direction. For a prolate spheroid with major axis c and shorter equal axes of length a, the shape anisotropy constant is given by

$$K_s = ½ (N_a – N_c)M^2 \qquad (5\text{-}7)$$

where Nc and Na are demagnetizing factors. Shape anisotropy can be significantly greater than the crystal anisotropy for nonspherical materials[241].

Since nanoscale materials have very high surface to volume ratio, another anisotropy term, surface anisotropy, can be applied to them. Surface anisotropy is the additional energy that binds the magnetization to the nanoparticle, similar to the crystal anisotropy. This stems from the broken symmetry (in comparison to the bulk) of the spins at the surface, which consequently affects the spin alignment relative to the surface. Nevertheless, it should be noted that surface anisotropy, like other nanoscale magnetic properties, is usually significant only at very small sizes (namely less than 3 nm).

5.4.2 Physical basis of superparamagnetism

In a ferromagnetic or ferromagnetic material, all the spins are coupled together below Tc, and hence yield a large total magnetic moment, whose direction is rigidly bound to the particle by some kinds of anisotropies. The energy of this bond is the total anisotropy energy, expressed as KV, where V is the volume of the particle. Obviously, as the particle size decreases, KV drops as well until it reaches a level comparable to the thermal energy, kT (k = Boltzmann constant), at which the bonding of the total moment to the particle is disrupted and

become free to change. The magnetic moment of these particles is given by $\mu_p = M_s V$, which can be quite large (super moment). Since the thermal energy would fight the alignment of this super moment, as it does in a paramagnetic material, it is called “superparamagnetism”. It should be noted that the superparamagnetic behavior is timescale-dependent due to the stochastic nature of the thermal energy. As the switching of magnetization in a superparamagnetic nanoparticle from one direction to another direction can be considered a thermally activated process, the timescale for a successful redirection can be specified by an Arrhenius equation as

$$\tau = \tau_0 e^{-KV/kT} \qquad (5\text{-}8)$$

where τ_0 is the attempt timescale, and KV is the anisotropy energy barrier to the total spin reorientation.

For a system to be superparamagnetic, the timescale of the experimental magnetization measurement must be larger than the attempt timescale (also called Neel relaxation time). The attempt timescale is about 10^{-9}, while the typical experiment with a magnetometer takes 10 to 100 s. Using τ = 100 s and $\tau_0 = 10^{-9}$ s, the critical volume under which the nanoparticle would act superparamagnetically at a certain temperature can be calculated from equation 4-8 by

$$V_{sp} = 25kT/K \qquad (5\text{-}9)$$

Typical superparamagnetic sizes for spherical (only crystal anisotropy) iron and cobalt are 16 and 7.6 nm, respectively, for T = 300 K [241].

Superparamagnetic materials will not show a hysteresis loop in magnetization measurement, as opposed to ferromagnetic materials. Superparamagnetic nanoparticles can be easily saturated in the presence of an external magnetic field, but the magnetization returns to zero upon removal of the field as a result of thermal fluctuations. Thus, both remnant magnetization (M_r) and coercivity (H_c) are zero. This behavior is analogous to conventional paramagnets, with the only difference that instead of individual electronic spins responding to thermal fluctuating, it is the collective moment of the entire particle that responds[242].

5.4.3 Superparamagnetic nanoparticles

Superparamagnetic nanoparticles, characterized by high saturation magnetization accompanied by a low saturation field and no remnant magnetization, have been shown to be ideal for biomedical applications. The lack of inter-particle interactions, which normally lead to aggregations of particles, enable the superparamagnetic NPs dispersion to be injected into biological systems and manipulated by external field gradients. Such NPs are currently finding applications in site specific treatments such as targeted drug delivery, localized heating of cancer cells (hyperthermia), and magnetic resonance imaging (MRI) contrast enhancement[242].

On the other side, biomedical applications require the magnetic particles to be stable in water at pH 7 and in the body physiological environment. Thus, for in vivo applications, the magnetic nanoparticles have been encapsulated with a biocompatible polymer during or after the preparation process to prevent changes from the original structure, the formation of large aggregates, and biodegradation when exposed to the biological system. The nanoparticle coated with polymer will also allow binding of drugs by entrapment on the particles, adsorption, or covalent attachment. Superparamagnetic iron oxide nanoparticles (SPION) such as magnetite (Fe_3O_4) or its oxidized form maghemite (γ-Fe_2O_3) have been by far the most commonly used nanoparticles for biomedical applications. The biomedical applications of other highly magnetic materials such as cobalt and nickel have been restricted due to their oxidation and toxicity [243].

5.4.4 Magnetic properties measurement by VSM

Magnetic properties of the synthesized magnetic nanoseeds were characterized using a vibrating sample magnetometer (VSM). VSM works by applying a uniform magnetic field generated from electromagnets across an oscillating sample near a set of voltage pick-up coils. The flux of uniform field will be distorted by the magnetization of the sample, which subsequently induces a potential drop, according to Faraday's law of induction, across the pick-

up coils. The voltage potential (V) is proportional to the magnetic moment of the sample, so the hysteresis loop (M-H curve) can be obtained by varying applied field while measuring the induced potential which translates to magnetic moment of the sample. To measure the magnetic properties of the synthesized nanoparticles, a small piece (typically a square of roughly 5 × 5 mm) of the AAO membrane containing the nanoparticles were mounted at the center of the VSM sampler holder (plastic rod). Then, the magnetic moment was measured by applying magnetic fields in the range of -10000 to 10000 Oe.

5.4.5 Magnetic behavior of Au@Pd@Co and Au@Pd@Co@Au nanoparticles

The M-H curve (hysteresis loop) obtained for APC sample by VSM measurement at room temperature is depicted in Figure 5-7. As can be observed, APC sample surprisingly shows the superparamagnetic characteristics; i.e. large magnetization with zero remanence and coercivity. As it was mentioned in the previous section, the calculated size of a superparamagnetic cobalt nanoparticle around room temperature based on crystal anisotropy (hcp structure) is 7.6 nm. Besides, a superparamagnetic limit of 9 nm has been reported for pure monocrystalline cobalt nanoparticles with fcc structure (fcc cobalt can be stable for small particles at room temperature)[244]. However, as can be seen from Figure 5-3, the thickness of the cobalt coating in APC NPs is around 70-80 nm, which is by far greater than the superparamagnetic limit, regardless of the supposed crystal structure.

Essentially, the superparamagnetic behavior of APC NPs at room temperature, despite their large size, should be related to their structural properties. It was indicated that superparamagnetic behavior appears when the anisotropy energy (KV) becomes comparable to the thermal energy (kT) at a certain temperature. The anisotropy energy can emerge from different sources, mostly crystal structure and shape of the material. Interestingly, the cobalt coating layer in the APC NPs was found to be amorphous, which means crystal anisotropy

energy can be considered as low as zero due to the lack of any symmetric crystal structure. Hence, a significant energy term is eliminated from the total anisotropy energy.

On the other side, despite the complex morphology of the synthesized APC NPs, their shapes are radial, which make them roughly identical from different spatial directions, particularly with random distributions over the NPs. As a result, shape anisotropy can also be considered negligible, at least in the conventional sense. Since the two major components of the anisotropy energy are not significant here, the total anisotropy energy (KV) would be comparable to the thermal energy (kT) under the measurement condition. The magnetic moment fluctuations caused by the thermal energy, therefore, would let the APC NPs act superparamagnetically.

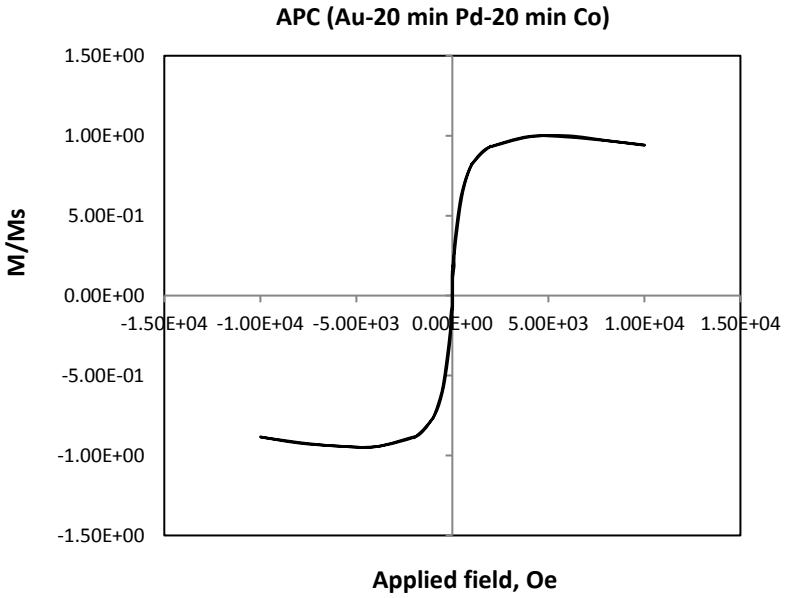

Figure 5-7 Magnetic hysteresis loop of Au-Pd-Co core-shell NPs (APC) at room temperature.

Amorphous alloys have homogeneous microstructures; i.e. there are no grains, no grain boundaries, and no precipitates of any substantial size. Most impurities tend to remain in solution rather than precipitating out when these alloys are rapidly quenched. As the particle size increases, a multi-magnetic-domain state is expected, but because the domain walls are wide in amorphous alloys and the defects are weak, there is a little pinning of domain walls on defects in amorphous materials and coercivity is expected to be very small (order of millioersteds) [236].

The 3d transition metal-based amorphous alloys are generally soft magnetic materials that lack long-range atomic order and consequently exhibit high metallic resistivity due to electron scattering from atomic disorder, no macroscopic magnetocrystalline anisotropy (only residual anisotropies due to internal stress) and no microstructural discontinuities (grain boundaries) on which magnetic domain walls can be pinned. These amorphous magnetic alloys have been demonstrated to show specific characteristics with potential for relevant applications. [236].

Although an amorphous microstructure can justify the room-temperature superparamagnetic behavior of cobalt-coated nanoseeds, other mechanisms can still be possible or partially contribute to the phenomenon. As such, it is possible that the Co layer consists of magnetically decoupled very small (< 7nm) Co superparamagnetic nanoparticles. However, the evidence of existing such small Co nanoparticles requires further characterization, as they were not directly observed here by TEM.

The result of magnetization measurement by VSM at room temperature for APCA sample is demonstrated in Figure 5-8. It can be seen that even after replacing some part of the cobalt coating with Au, the nanoseeds still show superparamagnetic behavior. This is, indeed, a big advantage of the developed synthesis process, as it provides superparamagnetic nanoparticles with biocompatible surface (Au), eliminating the concerns over the in vivo toxicity and chemical activity of cobalt coating. Furthermore, the versatile Au surface, with well-developed biochemistry, can be used for any subsequent functionalization and/or conjugation.

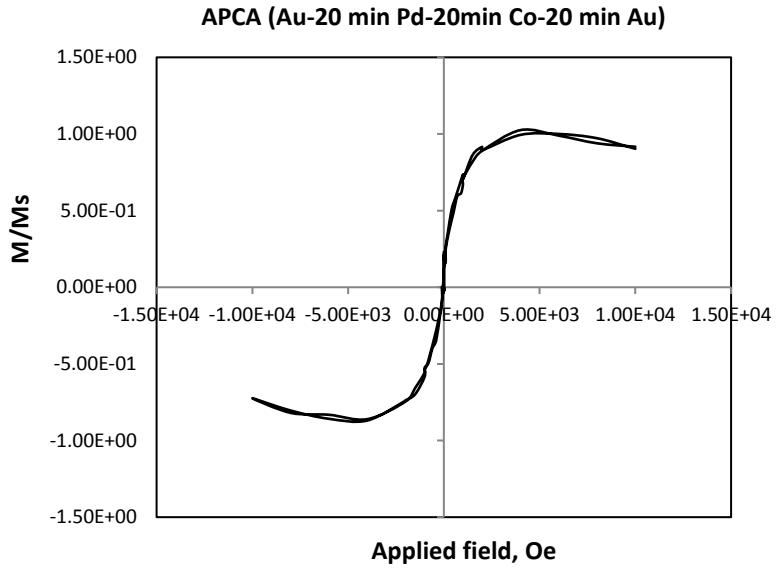

Figure 5-8 Magnetic hysteresis loop of Au-Pd-Co-Au core-shell NPs (APCA) at room temperature.

According to the VSM measurements, the only difference between the magnetic properties of APC and APCA samples is their total magnetization moment (Ms), which is higher for APC NPs, as shown in Figure 5-9. This seems a reasonable observation, as the total amount of magnetic material (cobalt) in APCA NPs was less than that in APC NPs. It should be mentioned that remaining of the template after incomplete nanoscale galvanic replacement reaction is considered a routine phenomenon. Nevertheless, the biomedical application of APCA NPs as MRI contrast agents during brachytherapy will not be affected by their smaller magnetization, as they should be still magnetic enough to be detected by MRI.

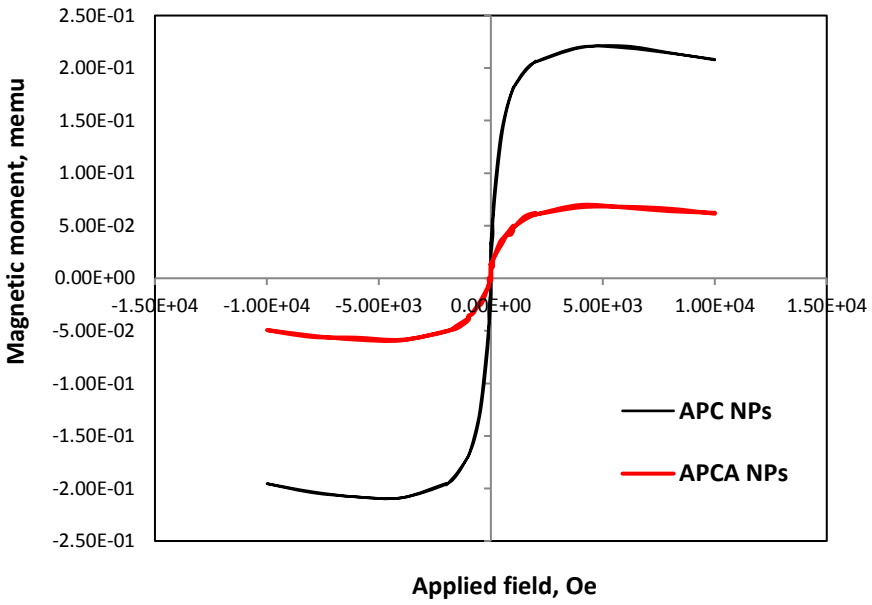

Figure 5-9 Magnetic properties of APC and APCA NPs measured by VSM at room temperature.

5.5 Magnetic resonance imaging (MRI) preliminary study

Magnetic resonance imaging relies on the counterbalance between the small magnetic moment on a proton and the large numbers of protons present in the tissue, and this effect can be measured in the presence of a large magnetic field. While X-ray and CT contrast agents can be detected directly by their different electron-density, in MRI the contrast enhancement occurs as a result of the interaction between the contrast agents and neighboring water protons [226].

Here, magnetic nanoseeds were investigated for the possibility of using them as MRI contrast agents during brachytherapy. Phantom scans of NPs solution along with DI water as control were done using a preclinical MRI scanner (Aspect Imaging M2TM). The samples were subjected to a magnetic field strength of 1 T (tesla), and T_2–weighted images were acquired using a sequence of two-dimensional spin echo (SE 2D), where T_R = 5000 ms (repetition time) and T_E = 500 ms (echo time).

The T_2-weighted MRI image of magnetic nanoseeds and water is shown in Figure 5-10. As can be observed, water appears brighter, while nanoseeds solution is darker, which implies the nanoseeds had T2 contrast. These results clearly show that magnetic nanoseeds can act as T_2-contrast agent, enabling MRI-guided brachytherapy.

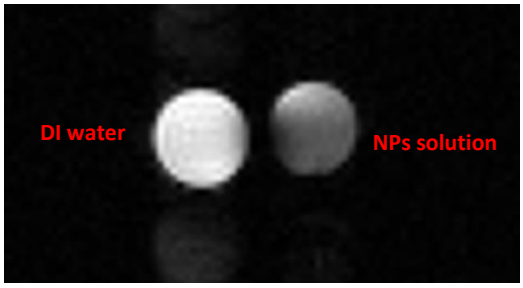

Figure 5-10 T_2-weighted image of MRI phantom scan of magnetic nanoseeds solution beside DI water.

Chapter 6 Summary

We have demonstrated that with the presence of a new type of Au nanoparticles, hollow Au nanoparticles (HAuNPs), the radiation damage to breast cancer MDA-MB-231cells are significantly enhanced when the cells are exposed to both kilo-voltage and mega-voltage X-rays. In the in vivo study, HAuNPs showed remarkable high tumor retention after being injected intratumorally to breast cancer tumor bearing mice, providing a practical potential to use AuNPs as radiosensitizing agents for radiotherapy enhancement at realistic concentrations of gold. A significant survival benefit was clearly observed when a single fraction radiation therapy (225 KeV, 10 Gy dose) was applied in the presence of HAuNPs in tumors, further confirming the radiosensitization effect of AuNPs. While the underlying mechanism is still under debate, this class of hollow shell gold nanoparticles hold great promise to synergize the treatment effect and index of radiation therapy for cancer.

We have demonstrated a facile method to efficiently incorporate radioactive isotopes onto HAuNPs to form brachytherapy nanoseeds. We have incorporated palladium-103 (^{103}Pd), a radioisotope currently in clinical brachytherapy, into a HAuNP. The therapeutic efficacy of ^{103}Pd@Au nanoseeds have been tested when intratumorally injected into a prostate cancer xenograft model. Capable of being permanently retained in tumor sites after intratumoral implantation and effectively reducing tumor burden without causing adverse side effects, this type of nanoseeds is expected to find applications in anti-cancer therapies, especially for the treatment of unresectable solid tumors. Given the results presented in this work, we believe the brachytherapy approach enabled by our nanoseeds would overcome the main drawbacks of the conventional brachytherapy with significantly reduced side effects and offer earlier thus more efficacious treatment that would lead to prolonged survival and better life quality of cancer patients.

We have synthesized multi-functional magnetic nanoseeds by electroless deposition of Co onto HAuNPs. Their magnetic properties showed such nanoseeds are potentially trackable by MRI, making real clinical application of nanoseeds more plausible for imaging-guided radiotherapy.

References

1. R. L. Siegel, K. D. Miller and A. Jemal, CA: A Cancer Journal for Clinicians 66 (1), 7 (2016)

2. Z. X. Liao, R. R. Komaki, H. D. Thames, Jr., H. H. Liu, S. L. Tucker, R. Mohan, M. K. Martel, X. Wei, K. Yang, E. S. Kim, G. Blumenschein, W. K. Hong and J. D. Cox, International Journal of Radiation Oncology Biology Physics 76 (3), 775 (2010)

3. S. Komatsu, Y. Hori, T. Fukumoto, M. Murakami, Y. Hishikawa and Y. Ku, World Journal of Gastroenterology 16 (14), 1800 (2010)

4. J. Klein, J. Livergant and J. Ringash, Oral Oncology 50 (4), 254 (2014)

5. M. Roach, European Urology 32, 48 (1997)

6. M. R. Mirza, E. Jakobsen, P. Pfeiffer, B. LindebjergClasen and J. C. Rose, Acta Oncologica 36 (2), 171 (1997)

7. R. Labianca, G. D. Beretta, B. Kildani, L. Milesi, F. Merlin, S. Mosconi, M. A. Pessi, T. Prochilo, A. Quadri, G. Gatta, F. de Braud and J. Wils, Critical Reviews in Oncology Hematology 74 (2), 106 (2010)

8. K. A. Goodman and C. Hajj, Journal of Surgical Oncology 107 (1), 86 (2013)

9. P. P. Connell and S. Hellman, Cancer Res. 69 (2), 383 (2009)

10. Y. Gavhane, A. Shete, A. Bhagat, V. Shinde, K. Bhong, G. Khairnar and A. Yadav, International Journal of Pharma Sciences and Research 2 (1), 1 (2011)

11. M. D. Glasgow and M. B. Chougule, Journal of biomedical nanotechnology 11 (11), 1859 (2015)

12. , American Cancer Society, (2016),

13. R. Banerjee and M. Kamrava, Int J Womens Health 6, 555 (2014)

14. R. R. Patel and D. W. Arthur, Hematology/Oncology Clinics of North America 20 (1), 97 (2006)

15. N. Suntharalingam, E. B. Podgorsak and H. TÖLLI, Podgorsak EB. Radiation Oncology Physics: a handbook for teachers and students. Vienna: International Atomic Energy Agency, 451 (2005)

16. J. C. Blasko, P. D. Grimm, J. E. Sylvester, K. R. Badiozamani, D. Hoak and W. Cavanagh, International Journal of Radiation Oncology*Biology*Physics 46 (4), 839 (2000)

17. V. Takiar, T. J. Pugh, D. Swanson, R. J. Kudchadker, T. L. Bruno, S. McAvoy, U. Mahmood and S. J. Frank, Brachytherapy 13 (1), 68 (2014)

18. M. Lock, J. Q. Cao, D. P. D'Souza, J. A. Hammond, S. Karnas, C. Lewis, V. M. Venkatesan, E. Whiston, G. Yau, E. Yu, J. Gilchrist and G. B. Rodrigues, Radiotherapy and Oncology 98 (3), 352 (2011)

19. A. I. Kassis and S. J. Adelstein, Journal of Nuclear Medicine 46 (1 suppl), 4S (2005)

20. J. C. Blasko, T. Mate, J. E. Sylvester, P. D. Grimm and W. Cavanagh, Brachytherapy for carcinoma of the prostate: techniques, patient selection, and clinical outcomes. In *Seminars in radiation oncology*, Elsevier, (2002), Vol. 12, pp 81

21. A. M. Nicolae, N. Venugopal and A. Ravi, Cancer Nanotechnology 7 (1), 1 (2016)

22. J. Mohler, R. R. Bahnson, B. Boston, J. E. Busby, A. D'Amico, J. A. Eastham, C. A. Enke, D. George, E. M. Horwitz and R. P. Huben, Journal of the National Comprehensive Cancer Network 8 (2), 162 (2010)

23. D. G. Petereit, S. J. Frank, A. N. Viswanathan, B. Erickson, P. Eifel, P. L. Nguyen and D. E. Wazer, Journal of Clinical Oncology 33 (9), 980 (2015)

24. D. Batchelar, M. Gaztañaga, M. Schmid, C. Araujo, F. Bachand and J. Crook, Brachytherapy 13 (1), 75 (2014)

25. P. Agoston, G. Stelczer, Z. Szabo, K. Jorgo, J. Lovey, T. Major and C. Polgar, International Journal of Radiation Oncology • Biology • Physics 90 (1), S441

26. V. E. Arterbery, A. Frazier, P. Dalmia, J. Siefer, M. Lutz and A. Porter, Seminars in surgical oncology 13 (6), 461 (1997)

27. R. G. Stock, J. Kao and N. N. Stone, The Journal of Urology 165 (2), 436 (2001)

28. P. Wardman, Clinical Oncology 19 (6), 397 (2007)

29. E. Amato, A. Italiano and S. Pergolizzi, International Journal of Nanotechnology 10 (12), 1045 (2013)

30. M. Ghorbani, D. Pakravan, M. Bakhshabadi and A. S. Meigooni, Nukleonika 57 (3), 401 (2012)

31. W. Ngwa, H. Korideck, A. I. Kassis, R. Kumar, S. Sridhar, G. M. Makrigiorgos and R. A. Cormack, Nanomedicine: Nanotechnology, Biology and Medicine 9 (1), 25 (2013)

32. Y. Huang, M. Ma, S. W. Chen, J. Dai, F. Chen and Z. Z. Wang, Rsc Advances 4 (51), 26861 (2014)

33. G. A. Lamoureux, W. Johnston and L. Costantini, Spacers for use in brachytherapy, radiotherapy, and other medical therapy. Google Patents, (2014),

34. R. Kumar, J. Belz, S. Markovic, T. Jadhav, W. Fowle, M. Niedre, R. Cormack, M. G. Makrigiorgos and S. Sridhar, International Journal of Radiation Oncology*Biology*Physics 91 (2), 393 (2015)

35. R. A. Cormack, S. Sridhar, W. W. Suh, A. V. D'Amico and G. M. Makrigiorgos, International Journal of Radiation Oncology*Biology*Physics 76 (2), 615 (2010)

36. N. Sinha, G. Cifter, E. Sajo, R. Kumar, S. Sridhar, P. L. Nguyen, R. A. Cormack, G. M. Makrigiorgos and W. Ngwa, International Journal of Radiation Oncology Biology Physics 91 (2), 385 (2015)

37. G. L. Mayers, Drug Development Research 67 (1), 94 (2006)

38. N. Chanda, P. Kan, L. D. Watkinson, R. Shukla, A. Zambre, T. L. Carmack, H. Engelbrecht, J. R. Lever, K. Katti, G. M. Fent, S. W. Casteel, C. J. Smith, W. H. Miller, S. Jurisson, E. Boote, J. D. Robertson, C. Cutler, M. Dobrovolskaia, R. Kannan and K. V. Katti, Nanomedicine-Nanotechnology Biology and Medicine 6 (2), 201 (2010)

39. R. Shukla, N. Chanda, A. Zambre, A. Upendran, K. Katti, R. R. Kulkarni, S. K. Nune, S. W. Casteel, C. J. Smith, J. Vimal, E. Boote, J. D. Robertson, P. Kan, H. Engelbrecht, L. D. Watkinson, T. L. Carmack, J. R. Lever, C. S. Cutler, C. Caldwell, R. Kannan and K. V. Katti, Proceedings of the National Academy of Sciences 109 (31), 12426 (2012)

40. M. K. Khan, L. D. Minc, S. S. Nigavekar, M. S. T. Kariapper, B. M. Nair, M. Schipper, A. C. Cook, W. G. Lesniak and L. P. Balogh, Nanomedicine: Nanotechnology, Biology and Medicine 4 (1), 57 (2008)

41. S. Yook, Z. L. Cai, Y. J. Lu, M. A. Winnik, J. P. Pignol and R. M. Reilly, Journal of Nuclear Medicine 57 (6), 936 (2016)

42. M. D. Shultz, J. D. Wilson, C. E. Fuller, J. Zhang, H. C. Dorn and P. P. Fatouros, Radiology 261 (1), 136 (2011)

43. E. Allard, C. Passirani and J.-P. Benoit, Biomaterials 30 (12), 2302 (2009)

44. W. T. Phillips, B. Goins, A. Bao, D. Vargas, J. E. Guttierez, A. Trevino, J. R. Miller, J. Henry, R. Zuniga, G. Vecil and A. J. Brenner, Neuro-Oncology 14 (4), 416 (2012)

45. F. M. Paes and A. N. Serafini, Seminars in Nuclear Medicine 40 (2), 89 (2010)

46. T. J. Whelan, J. Julian, J. Wright, A. R. Jadad and M. L. Levine, Journal of Clinical Oncology 18 (6), 1220 (2000)

47. A. Abner, A. Becht, J. L. Connolly, S. J. Schnitt, A. Nixon, B. Silver and J. R. Harris, International Journal of Radiation Oncology* Biology* Physics 24, 128 (1992)

48. B. J. Moeller, R. A. Richardson and M. W. Dewhirst, Cancer and Metastasis Reviews 26 (2), 241 (2007)

49. S. J. Oldenburg, S. L. Westcott, R. D. Averitt and N. J. Halas, Journal of Chemical Physics 111 (10), 4729 (1999)

50. M. Kerker, D. S. Wang and H. Chew, Applied Optics 19 (24), 4159 (1980)

51. L. Olofsson, T. Rindzevicius, I. Pfeiffer, M. Kall and F. Hook, Langmuir 19 (24), 10414 (2003)

52. J. Chen, F. Saeki, B. J. Wiley, H. Cang, M. J. Cobb, Z. Y. Li, L. Au, H. Zhang, M. B. Kimmey, X. D. Li and Y. Xia, Nano Lett. 5 (3), 473 (2005)

53. A. M. Gobin, M. H. Lee, N. J. Halas, W. D. James, R. A. Drezek and J. L. West, Nano Lett. 7 (7), 1929 (2007)

54. S. Keren, C. Zavaleta, Z. Cheng, A. de la Zerda, O. Gheysens and S. S. Gambhir, Proceedings of the National Academy of Sciences of the United States of America 105 (15), 5844 (2008)

55. X. M. Qian, X. H. Peng, D. O. Ansari, Q. Yin-Goen, G. Z. Chen, D. M. Shin, L. Yang, A. N. Young, M. D. Wang and S. M. Nie, Nat. Biotechnol. 26 (1), 83 (2008)

56. X. H. Huang, I. H. El-Sayed, W. Qian and M. A. El-Sayed, J. Am. Chem. Soc. 128 (6), 2115 (2006)

57. P. K. Jain, I. H. El-Sayed and M. A. El-Sayed, Nano Today 2 (1), 18 (2007)

58. S. Lee, E. J. Cha, K. Park, S. Y. Lee, J. K. Hong, I. C. Sun, S. Y. Kim, K. Choi, I. C. Kwon, K. Kim and C. H. Ahn, Angewandte Chemie-International Edition 47 (15), 2804 (2008)

59. S. Link and M. A. Ei-Sayed, Annual Review of Physical Chemistry 54, 331 (2003)

60. R. Gans, Ann. Phys. (37), 881 (1912)

61. R. D. Averitt, S. L. Westcott and N. J. Halas, Journal of the Optical Society of America B-Optical Physics 16 (10), 1824 (1999)

62. R. Weissleder, Nat. Biotechnol. 19 (4), 316 (2001)

63. M. faraday, Philosophical Transactions of the Royal Society of London 147 (147), 145 (1857)

64. N. R. Jana, L. Gearheart and C. J. Murphy, Langmuir 17 (22), 6782 (2001)

65. S. J. Oldenburg, R. D. Averitt, S. L. Westcott and N. J. Halas, Chemical Physics Letters 288 (2-4), 243 (1998)

66. S. E. Skrabalak, L. Au, X. D. Li and Y. Xia, Nature Protocols 2 (9), 2182 (2007)

67. C. W. Huang, J. C. Jiang, M. Y. Lu, L. Sun, E. I. Meletis and Y. W. Hao, Nano Lett. 9 (12), 4297 (2009)

68. E. C. Dreaden, A. M. Alkilany, X. Huang, C. J. Murphy and M. A. El-Sayed, Chemical Society Reviews 41 (7), 2740 (2012)

69. A. Jemal, R. Siegel, E. Ward, Y. P. Hao, J. Q. Xu and M. J. Thun, Ca-a Cancer Journal for Clinicians 59 (4), 225 (2009)

70. J. Y. Chen, B. Wiley, Z. Y. Li, D. Campbell, F. Saeki, H. Cang, L. Au, J. Lee, X. D. Li and Y. N. Xia, Advanced Materials 17 (18), 2255 (2005)

71. Y. Luo, W. Sun, Y. Gu, G. F. Wang and N. Fang, Analytical Chemistry 82 (15), 6675 (2010)

72. D. Kim, S. Park, J. H. Lee, Y. Y. Jeong and S. Jon, J. Am. Chem. Soc. 129 (24), 7661 (2007)

73. V. Kattumuri, K. Katti, S. Bhaskaran, E. J. Boote, S. W. Casteel, G. M. Fent, D. J. Robertson, M. Chandrasekhar, R. Kannan and K. V. Katti, Small (Weinheim an der Bergstrasse, Germany) 3 (2), 333 (2007)

74. Q. Y. Cai, S. H. Kim, K. S. Choi, S. Y. Kim, S. J. Byun, K. W. Kim, S. H. Park, S. K. Juhng and K. H. Yoon, Investigative Radiology 42 (12), 797 (2007)

75. J. A. Copland, M. Eghtedari, V. L. Popov, N. Kotov, N. Mamedova, M. Motamedi and A. A. Oraevsky, Mol. Imaging. Biol. 6 (5), 341 (2004)

76. P. Sharma, S. C. Brown, N. Bengtsson, Q. Z. Zhang, G. A. Walter, S. R. Grobmyer, S. Santra, H. B. Jiang, E. W. Scott and B. M. Moudgil, Chem Mater 20 (19), 6087 (2008)

77. X. M. Yang, S. E. Skrabalak, Z. Y. Li, Y. N. Xia and L. H. V. Wang, Nano Lett. 7 (12), 3798 (2007)

78. Y. W. Wang, X. Y. Xie, X. D. Wang, G. Ku, K. L. Gill, D. P. O'Neal, G. Stoica and L. V. Wang, Nano Lett. 4 (9), 1689 (2004)

79. S. Moeendarbari, A. Mulgaonkar, A. S. Hande, W. Silvers, C. Zhang, Y. Liu, A. K. Pillai, X. Sun and Y. Hao, Reviews in Nanoscience and Nanotechnology 5 (1), 28 (2016)

80. B. I. Lee, K. S. Lee, J. H. Lee, I. S. Lee and S. H. Byeon, Dalton Transactions (14), 2490 (2009)

81. J. J. Crochet, S. C. Gnyawali, Y. C. Chen, E. C. Lemley, L. H. V. Wang and W. R. Chen, J Biomed Opt 11 (3), (2006)

82. A. B. Fuertes and P. Tartaj, Chem Mater 18 (6), 1675 (2006)

83. A. O. Govorov and H. H. Richardson, Nano Today 2 (1), 30 (2007)

84. M. Rashidi-Huyeh and B. Palpant, Journal of Applied Physics 96 (8), 4475 (2004)

85. S. Lal, S. E. Clare and N. J. Halas, Accounts of Chemical Research 41 (12), 1842 (2008)

86. G. S. Terentyuk, G. N. Maslyakova, L. V. Suleymanova, N. G. Khlebtsov, B. N. Khlebtsov, G. G. Akchurin, I. L. Maksimova and V. V. Tuchin, J Biomed Opt 14 (2), 9 (2009)

87. C. H. Liu, C. C. Mi and B. Q. Li, Ieee Transactions on Nanobioscience 7 (3), 206 (2008)

88. V. P. Zharov, K. E. Mercer, E. N. Galitovskaya and M. S. Smeltzer, Biophysical Journal 90 (2), 619 (2006)

89. S. Link, M. B. Mohamed and M. A. El-Sayed, J. Phys. Chem. B 103 (16), 3073 (1999)

90. E. B. Dickerson, E. C. Dreaden, X. H. Huang, I. H. El-Sayed, H. H. Chu, S. Pushpanketh, J. F. McDonald and M. A. El-Sayed, Cancer Lett 269 (1), 57 (2008)

91. G. von Maltzahn, J. H. Park, A. Agrawal, N. K. Bandaru, S. K. Das, M. J. Sailor and S. N. Bhatia, Cancer Research 69 (9), 3892 (2009)

92. D. P. O'Neal, L. R. Hirsch, N. J. Halas, J. D. Payne and J. L. West, Cancer Lett 209 (2), 171 (2004)

93. J. M. Stern, J. Stanfield, W. Kabbani, J. T. Hsieh and J. R. A. Cadeddu, Journal of Urology 179 (2), 748 (2008)

94. J. Y. Chen, C. Glaus, R. Laforest, Q. Zhang, M. X. Yang, M. Gidding, M. J. Welch and Y. N. Xia, Small (Weinheim an der Bergstrasse, Germany) 6 (7), 811 (2010)

95. R. S. Pieters, L. Ding, H. Bushe and J. N. Aronowitz, (2014)

96. X. B. Yao, C. N. Huang, X. P. Chen, Y. Zheng and L. Sanche, Journal of Biomedical Nanotechnology 11 (3), 478 (2015)

97. C. D. Zhu, Q. Zheng, L. X. Wang, H. F. Xu, J. L. Tong, Q. A. Zhang, Y. Wan and J. Q. Wu, Journal of Nanobiotechnology 13, (2015)

98. Y. Liu, X. Liu, X. D. Jin, P. B. He, X. G. Zheng, Z. Y. Dai, F. Ye, T. Zhao, W. Q. Chen and Q. Li, Physica Medica-European Journal of Medical Physics 31 (3), 210 (2015)

99. J. Wu, D. Liang, Q. Jin, J. Liu, M. Zheng, X. Duan and X. Tang, Chemistry-a European Journal 21 (37), 12914 (2015)

100. C. W. Huang, V. Kearney, S. Moeendarbari, R. Q. Jiang, P. Christensen, R. Tekade, X. K. Sun, W. H. Mao and Y. W. Hao, Journal of Nano Research 32, 106 (2015)

101. S. Setua, M. Ouberai, S. G. Piccirillo, C. Watts and M. Welland, Nanoscale 6 (18), 10865 (2014)

102. W. N. Rahman, S. Corde, N. Yagi, S. A. A. Aziz, N. Annabell and M. Geso, International Journal of Nanomedicine 9, 2459 (2014)

103. K. Khoshgard, B. Hashemi, A. Arbabi, M. J. Rasaee and M. Soleimani, Physics in Medicine and Biology 59 (9), 2249 (2014)

104. L. Cui, K. Tse, P. Zahedi, S. M. Harding, G. Zafarana, D. A. Jaffray, R. G. Bristow and C. Allen, Radiation Research 182 (5), 475 (2014)

105. E. Lechtman, S. Mashouf, N. Chattopadhyay, B. M. Keller, P. Lai, Z. Cai, R. M. Reilly and J. P. Pignol, Physics in Medicine and Biology 58 (10), 3075 (2013)

106. M. Douglass, E. Bezak and S. Penfold, Medical Physics 40 (7), (2013)

107. S. Jain, J. A. Coulter, A. R. Hounsell, K. T. Butterworth, S. J. McMahon, W. B. Hyland, M. F. Muir, G. R. Dickson, K. M. Prise, F. J. Currell, J. M. O'Sullivan and D. G. Hirst, International Journal of Radiation Oncology Biology Physics 79 (2), 531 (2011)

108. F. Geng, K. Song, J. Z. Xing, C. Yuan, S. Yan, Q. Yang, J. Chen and B. Kong, Nanotechnology 22 (28), (2011)

109. S. H. Cho, Physics in Medicine and Biology 50 (15), N163 (2005)

110. T. Kong, J. Zeng, X. Wang, X. Yang, J. Yang, S. McQuarrie, A. McEwan, W. Roa, J. Chen and J. Z. Xing, Small 4 (9), 1537 (2008)

111. W. N. Rahman, N. Bishara, T. Ackerly, C. F. He, P. Jackson, C. Wong, R. Davidson and M. Geso, Nanomedicine-Nanotechnology Biology and Medicine 5 (2), 136 (2009)

112. W. Roa, X. Zhang, L. Guo, A. Shaw, X. Hu, Y. Xiong, S. Gulavita, S. Patel, X. Sun, J. Chen, R. Moore and J. Z. Xing, Nanotechnology 20 (37), (2009)

113. K. T. Butterworth, J. A. Coulter, S. Jain, J. Forker, S. J. McMahon, G. Schettino, K. M. Prise, F. J. Currell and D. G. Hirst, Nanotechnology 21 (29), (2010)

114. J. F. Hainfeld, F. A. Dilmanian, Z. Zhong, D. N. Slatkin, J. A. Kalef-Ezra and H. M. Smilowitz, Physics in Medicine and Biology 55 (11), 3045 (2010)

115. B. L. Jones, S. Krishnan and S. H. Cho, Medical Physics 37 (7), 3809 (2010)

116. C.-J. Liu, C.-H. Wang, S.-T. Chen, H.-H. Chen, W.-H. Leng, C.-C. Chien, C.-L. Wang, I. M. Kempson, Y. Hwu, T.-C. Lai, M. Hsiao, C.-S. Yang, Y.-J. Chen and G. Margaritondo, Physics in Medicine and Biology 55 (4), 931 (2010)

117. K. T. Butterworth, S. J. McMahon, F. J. Currell and K. M. Prise, Nanoscale 4 (16), 4830 (2012)

118. S. J. McMahon, W. B. Hyland, M. F. Muir, J. A. Coulter, S. Jain, K. T. Butterworth, G. Schettino, G. R. Dickson, A. R. Hounsell, J. M. O'Sullivan, K. M. Prise, D. G. Hirst and F. J. Currell, Radiotherapy and Oncology 100 (3), 412 (2011)

119. Y. T. Lin, S. J. McMahon, H. Paganetti and J. Schuemann, Physics in Medicine and Biology 60 (10), 4149 (2015)

120. J. C. Roeske, L. Nunez, M. Hoggarth, E. Labay and R. R. Weichselbaum, Technology in cancer research & treatment 6 (5), 395 (2007)

121. D. B. Chithrani, S. Jelveh, F. Jalali, M. van Prooijen, C. Allen, R. G. Bristow, R. P. Hill and D. A. Jaffray, Radiat. Res. 173 (6), 719 (2010)

122. S. Jain, J. A. Coulter, A. R. Hounsell, K. T. Butterworth, S. J. McMahon, W. B. Hyland, M. F. Muir, G. R. Dickson, K. M. Prise, F. J. Currell, J. M. O'Sullivan and D. G. Hirst, International journal of radiation oncology, biology, physics 79 (2), 531 (2011)

123. M. Y. Chang, A. L. Shiau, Y. H. Chen, C. J. Chang, H. H. W. Chen and C. L. Wu, Cancer Science 99 (7), 1479 (2008)

124. P. Diagaradjane, A. Shetty, J. C. Wang, A. M. Elliott, J. Schwartz, S. Shentu, H. C. Park, A. Deorukhkar, R. J. Stafford, S. H. Cho, J. W. Tunnell, J. D. Hazle and S. Krishnan, Nano Letters 8 (5), 1492 (2008)

125. J. K. Kim, S. J. Seo, H. T. Kim, K. H. Kim, M. H. Chung, K. R. Kim and S. J. Ye, Physics in Medicine and Biology 57 (24), 15 (2012)

126. J. F. Hainfeld, H. M. Smilowitz, M. J. O'Connor, F. A. Dilmanian and D. N. Slatkin, Nanomedicine 8 (10), 1601 (2013)

127. D. Y. Joh, G. D. Kao, S. Murty, M. Stangl, L. Sun, A. Al Zaki, X. S. Xu, S. M. Hahn, A. Tsourkas and J. F. Dorsey, Translational Oncology 6 (6), 722 (2013)

128. J. F. Hainfeld, L. Lin, D. N. Slatkin, F. A. Dilmanian, T. M. Vadas and H. M. Smilowitz, Nanomedicine-Nanotechnology Biology and Medicine 10 (8), 1609 (2014)

129. I. Miladi, C. Alric, S. Dufort, P. Mowat, A. Dutour, C. Mandon, G. Laurent, E. Brauer-Krisch, N. Herath, J. L. Coll, M. Dutreix, F. Lux, R. Bazzi, C. Billotey, M. Janier, P. Perriat, G. Le Duc, S. Roux and O. Tillement, Small 10 (6), 1116 (2014)

130. D. M. Herold, I. J. Das, C. C. Stobbe, R. V. Iyer and J. D. Chapman, Int. J. Radiat. Biol. 76 (10), 1357 (2000)

131. J. F. Hainfeld, D. N. Slatkin and H. M. Smilowitz, Physics in Medicine and Biology 49 (18), N309 (2004)

132. X. D. Zhang, D. Wu, X. Shen, J. Chen, Y. M. Sun, P. X. Liu and X. J. Liang, Biomaterials 33 (27), 6408 (2012)

133. T. Wolfe, D. Chatterjee, J. Lee, J. D. Grant, S. Bhattarai, R. Tailor, G. Goodrich, P. Nicolucci and S. Krishnan, Nanomedicine-Nanotechnology Biology and Medicine 11 (5), 1277 (2015)

134. N. Chattopadhyay, Z. Cai, Y. L. Kwon, E. Lechtman, J.-P. Pignol and R. M. Reilly, Breast cancer research and treatment 137 (1), 81 (2013)

135. E. M. Hebert, P. J. Debouttiere, M. Lepage, L. Sanche and D. J. Hunting, International Journal of Radiation Biology 86 (8), 692 (2010)

136. J. F. Hainfeld, H. M. Smilowitz, M. J. O'Connor, F. A. Dilmanian and D. N. Slatkin, Nanomedicine : nanotechnology, biology, and medicine 8 (10), 1601 (2013)

137. X. D. Zhang, Z. T. Luo, J. Chen, X. Shen, S. S. Song, Y. M. Sun, S. J. Fan, F. Y. Fan, D. T. Leong and J. P. Xie, Advanced Materials 26 (26), 4565 (2014)

138. X. D. Zhang, Z. T. Luo, J. Chen, S. S. Song, X. Yuan, X. Shen, H. Wang, Y. M. Sun, K. Gao, L. F. Zhang, S. J. Fan, D. T. Leong, M. L. Guo and J. P. Xie, Scientific Reports 5, (2015)

139. C. McQuade, A. Al Zaki, Y. Desai, M. Vido, T. Sakhuja, Z. L. Cheng, R. J. Hickey, D. Joh, S. J. Park, G. Kao, J. F. Dorsey and A. Tsourkas, Small 11 (7), 834 (2015)

140. J. Park, J. Park, E. J. Ju, S. S. Park, J. Choi, J. H. Lee, K. J. Lee, S. H. Shin, E. J. Ko, I. Park, C. Kim, J. J. Hwang, J. S. Lee, S. Y. Song, S. Y. Jeong and E. K. Choi, Journal of Controlled Release 207, 77 (2015)

141. X. Yang, M. X. Yang, B. Pang, M. Vara and Y. N. Xia, Chemical Reviews 115 (19), 10410 (2015)

142. B. Merchant, Biologicals 26 (1), 49 (1998)

143. Y. Pan, S. Neuss, A. Leifert, M. Fischler, F. Wen, U. Simon, G. Schmid, W. Brandau and W. Jahnen-Dechent, Small (Weinheim an der Bergstrasse, Germany) 3 (11), 1941 (2007)

144. W. I. H. J. H. Fan, W. T. Li and J. M. Yeh, IFBME Proceedings 23, 870 (2009)

145. L. Truong, S. C. Tilton, T. Zaikova, E. Richman, K. M. Waters, J. E. Hutchison and R. L. Tanguay, Nanotoxicology 7 (2), 192 (2013)

146. Y. S. Chen, Y. C. Hung, I. Liau and G. S. Huang, Nanoscale Res Lett 4 (8), 858 (2009)

147. D. Shenoy, W. Fu, J. Li, C. Crasto, G. Jones, C. DiMarzio, S. Sridhar and M. Amiji, International journal of nanomedicine 1 (1), 51 (2006)

148. R. Shukla, V. Bansal, M. Chaudhary, A. Basu, R. R. Bhonde and M. Sastry, Langmuir 21 (23), 10644 (2005)

149. C. Zhou, M. Long, Y. Qin, X. Sun and J. Zheng, Angewandte Chemie (International ed. in English) 50 (14), 3168 (2011)

150. M. Zhou, B. Wang, Z. Rozynek, Z. Xie, J. O. Fossum, X. Yu and S. Raaen, Nanotechnology 20 (50), 0957 (2009)

151. A. M. Alkilany, P. K. Nagaria, C. R. Hexel, T. J. Shaw, C. J. Murphy and M. D. Wyatt, Small (Weinheim an der Bergstrasse, Germany) 5 (6), 701 (2009)

152. L. Sun, D. Liu and Z. Wang, Langmuir 24 (18), 10293 (2008)

153. S. Deokule, L. Alencar, G. Vizzeri, F. Medeiros and R. N. Weinreb, Ophthal Surg Las Im 43 (1), 39 (2012)

154. G. F. Paciotti, D. G. I. Kingston and L. Tamarkin, Drug Dev. Res. 67 (1), 47 (2006)

155. E. E. Connor, J. Mwamuka, A. Gole, C. J. Murphy and M. D. Wyatt, Small (Weinheim an der Bergstrasse, Germany) 1 (3), 325 (2005)

156. C.-H. Su, H.-S. Sheu, C.-Y. Lin, C.-C. Huang, Y.-W. Lo, Y.-C. Pu, J.-C. Weng, D.-B. Shieh, J.-H. Chen and C.-S. Yeh, J. Am. Chem. Soc. 129 (7), 2139 (2007)

157. T. Niidome, M. Yamagata, Y. Okamoto, Y. Akiyama, H. Takahashi, T. Kawano, Y. Katayama and Y. Niidome, Journal of controlled release : official journal of the Controlled Release Society 114 (3), 343 (2006)

158. C. M. Goodman, C. D. McCusker, T. Yilmaz and V. M. Rotello, Bioconjug Chem 15 (4), 897 (2004)

159. C. Di Guglielmo, D. R. Lopez, J. De Lapuente, J. M. Mallafre and M. B. Suarez, Reprod Toxicol 30 (2), 271 (2010)

160. N. Pernodet, X. Fang, Y. Sun, A. Bakhtina, A. Ramakrishnan, J. Sokolov, A. Ulman and M. Rafailovich, Small (Weinheim an der Bergstrasse, Germany) 2 (6), 766 (2006)

161. C. Villiers, H. Freitas, R. Couderc, M. B. Villiers and P. Marche, J Nanopart Res 12 (1), 55 (2010)

162. T. Mironava, M. Hadjiargyrou, M. Simon, V. Jurukovski and M. H. Rafailovich, Nanotoxicology 4 (1), 120 (2010)

163. H. K. Patra, S. Banerjee, U. Chaudhuri, P. Lahiri and A. K. Dasgupta, Nanomedicine : nanotechnology, biology, and medicine 3 (2), 111 (2007)

164. S. Rao, V. Lin, C. Huang, U. Tata, P. Wu, N. Arora, K. Pokhrel, Y. Hao and J.-C. Chiao, Journal of Nanotechnology 2014 (Article ID 631248), 7 pages (2014)

165. G. Sonavane, K. Tomoda and K. Makino, Colloids Surf B Biointerfaces 66 (2), 274 (2008)

166. C. Lasagna-Reeves, D. Gonzalez-Romero, M. A. Barria, I. Olmedo, A. Clos, V. M. Sadagopa Ramanujam, A. Urayama, L. Vergara, M. J. Kogan and C. Soto, Biochem Biophys Res Commun 393 (4), 649 (2010)

167. D. T. Wiley, P. Webster, A. Gale and M. E. Davis, Proc Natl Acad Sci U S A 110 (21), 8662 (2013)

168. J. H. Kim, K. W. Kim, M. H. Kim and Y. S. Yu, Nanotechnology 20 (50), 0957 (2009)

169. J. Liu, M. Yu, C. Zhou and J. Zheng, Materials Today 16 (12), 477 (2013)

170. R. L. Siegel, K. D. Miller and A. Jemal, CA: A Cancer Journal for Clinicians 65 (1), 5 (2015)

171. B. D. Lehmann, J. A. Bauer, X. Chen, M. E. Sanders, A. B. Chakravarthy, Y. Shyr and J. A. Pietenpol, The Journal of Clinical Investigation 121 (7), 2750 (2011)

172. M. S. Moran, The Lancet Oncology 16 (3), e113

173. B. S. Abdulkarim, J. Cuartero, J. Hanson, J. Deschênes, D. Lesniak and S. Sabri, Journal of Clinical Oncology 29 (21), 2852 (2011)

174. L. T. Steward, F. Gao, M. A. Taylor and J. A. Margenthaler, Oncology Letters 7 (2), 548 (2014)

175. A. V. Mesa, A. Norman, T. D. Solberg, J. J. Demarco and J. B. Smathers, Physics in Medicine and Biology 44 (8), 1955 (1999)

176. D. Regulla, E. Schmid, W. Friedland, W. Panzer, U. Heinzmann and D. Harder, Radiation Research 158 (4), 505 (2002)

177. J. L. Robar, S. A. Riccio and M. A. Martin, Physics in Medicine and Biology 47 (14), 2433 (2002)

178. E. M. Hébert, P.-J. Debouttière, M. Lepage, L. Sanche and D. J. Hunting, Int. J. Radiat. Biol. 86 (8), 692 (2010)

179. C. Huang, J. Jiang, M. Lu, L. Sun, E. I. Meletis and Y. Hao, Nano Letters 9 (12), 4297 (2009)

180. C. Lee, N. N. Cheng, R. A. Davidson and T. Guo, The Journal of Physical Chemistry C 116 (20), 11292 (2012)

181. T. T. Puck and P. I. Marcus, Journal of Experimental Medicine 103 (5), 653 (1956)

182. Y. Pan, A. Leifert, D. Ruau, S. Neuss, J. Bornemann, G. Schmid, W. Brandau, U. Simon and W. Jahnen-Dechent, Small 5 (18), 2067 (2009)

183. C. M. Goodman, C. D. McCusker, T. Yilmaz and V. M. Rotello, Bioconjugate Chemistry 15 (4), 897 (2004)

184. Y. Pan, S. Neuss, A. Leifert, M. Fischler, F. Wen, U. Simon, G. Schmid, W. Brandau and W. Jahnen-Dechent, Small 3 (11), 1941 (2007)

185. G. Sonavane, K. Tomoda and K. Makino, Colloids and Surfaces B-Biointerfaces 66 (2), 274 (2008)

186. R. Miralbell, A. Zietman, P. Okunieff, H. D. Thames and H. D. Suit, International Journal of Radiation Oncology*Biology*Physics 18 (4), 867 (1990)

187. M. M. Tomayko and C. P. Reynolds, Cancer chemotherapy and pharmacology 24 (3), 148 (1989)

188. L. E. Taggart, S. J. McMahon, F. J. Currell, K. M. Prise and K. T. Butterworth, Cancer Nanotechnology 5 (1), 5 (2014)

189. N. N. Cheng, Z. Starkewolf, R. A. Davidson, A. Sharmah, C. Lee, J. Lien and T. Guo, Journal of the American Chemical Society 134 (4), 1950 (2012)

190. D. K. Chatterjee, T. Wolfe, J. Lee, A. P. Brown, P. K. Singh, S. R. Bhattarai, P. Diagaradjane and S. Krishnan, Translational cancer research 2 (4), 256 (2013)

191. J. F. Hainfeld, F. A. Dilmanian, D. N. Slatkin and H. M. Smilowitz, Journal of Pharmacy and Pharmacology 60 (8), 977 (2008)

192. A. Akinbami, A. Popoola, A. Adediran, A. Dosunmu, O. Oshinaike, P. Adebola and S. Ajibola, Caspian Journal of Internal Medicine 4 (1), 574 (2013)

193. S. S. K. Kamal, P. K. Sahoo, B. Sreedhar, M. M. Raja, L. Durai and S. Ram, Mater. Sci. Eng. B-Adv. Funct. Solid-State Mater. 177 (14), 1200 (2012)

194. M. Mac Manus, K. Lamborn, W. Khan, A. Varghese, L. Graef and S. Knox, Blood 89 (7), 2303 (1997)

195. E. G. Giannini, R. Testa and V. Savarino, CMAJ : Canadian Medical Association Journal 172 (3), 367 (2005)

196. J. P. Kassirer New England Journal of Medicine 285 (7), 385 (1971)

197. D. Y. Joh, L. Sun, M. Stangl, A. Al Zaki, S. Murty, P. P. Santoiemma, J. J. Davis, B. C. Baumann, M. Alonso-Basanta, D. Bhang, G. D. Kao, A. Tsourkas and J. F. Dorsey, PLoS ONE 8 (4), e62425 (2013)

198. W. Ngwa, R. Kumar, S. Sridhar, H. Korideck, P. Zygmanski, R. A. Cormack, R. Berbeco and G. M. Makrigiorgos, Nanomedicine (London, England) 9 (7), 1063 (2014)

199. S. Saito, H. Nagata, M. Kosugi, K. Toya and A. Yorozu, Int J Clin Oncol 12 (6), 395 (2007)

200. G. S. Merrick, K. E. Wallner and W. M. Butler, The Journal of Urology 169 (5), 1643 (2003)

201. R. E. Peschel, J. W. Colberg, Z. Chen, R. Nath and L. D. Wilson, Cancer J. 10 (3), 170 (2004)

202. J. M. Cosset, T. Flam, N. Thiounn, J. C. Rosenwald, D. Pontvert, M. Timbert, S. Solignac and L. Chauveinc, Bulletin Du Cancer 93 (8), 761 (2006)

203. R. R. Patel and D. W. Arthur, Hematology-Oncology Clinics of North America 20 (1), 97 (2006)

204. T. J. Wilt and I. M. Thompson, British Medical Journal 333 (7578), 1102 (2006)

205. M. Kanikowski, J. Skowronek, M. Kubaszewska, A. ChicheŁ and P. Milecki, Reports of Practical Oncology & Radiotherapy 13 (3), 150 (2008)

206. S. Bensaleh, E. Bezak and M. Borg, Acta Oncologica 48 (4), 487 (2009)

207. Y. Yoshioka, Int J Clin Oncol 14 (1), 31 (2009)

208. E. Semenova and P. T. Finger, Ophthalmology 120 (11), 2353 (2013)

209. B. D. Anderson and J. B. Tracy, Nanoscale 6 (21), 12195 (2014)

210. X. Xia, Y. Wang, A. Ruditskiy and Y. Xia, Advanced Materials 25 (44), 6313 (2013)

211. M. E. Phelps, *PET: molecular imaging and its biological applications*. Springer, (2004),

212. G. J. Kelloff, J. M. Hoffman, B. Johnson, H. I. Scher, B. A. Siegel, E. Y. Cheng, B. D. Cheson, J. O'Shaughnessy, K. Z. Guyton and D. A. Mankoff, Clinical Cancer Research 11 (8), 2785 (2005)

213. K. Chen and X. Y. Chen, Semin. Oncol. 38 (1), 70 (2011)

214. M. D. Farwell, D. A. Pryma and D. A. Mankoff, Cancer 120 (22), 3433 (2014)

215. A. Pottier, E. Borghi and L. Levy, Anticancer Research 34 (1B), 443 (2014)

216. A. J. Berdis, Expert Opinion on Drug Discovery 9 (2), 167 (2014)

217. J. A. Coulter, W. B. Hyland, J. Nicol and F. J. Currell, Clinical Oncology 25 (10), 593 (2013)

218. A. G. Linkous and E. M. Yazlovitskaya, Anticancer Research 32 (7), 2487 (2012)

219. S. H. Cho, B. L. Jones and S. Krishnan, Physics in Medicine and Biology 54 (16), 4889 (2009)

220. J. C. Roeske, L. Nunez, M. Hoggarth, E. Labay and R. R. Weichselbaum, Technol. Cancer Res. Treat. 6 (5), 395 (2007)

221. W. Ngwa, G. M. Makrigiorgos and R. I. Berbeco, Physics in Medicine and Biology 55 (21), 6533 (2010)

222. N. Khlebtsov and L. Dykman, Chem. Soc. Rev. 40 (3), 1647 (2011)

223. R. Shukla, N. Chanda, A. Zambre, A. Upendran, K. Katti, R. R. Kulkarni, S. K. Nune, S. W. Casteel, C. J. Smith, J. Vimal, E. Boote, J. D. Robertson, P. Kan, H. Engelbrecht, L. D. Watkinson, T. L. Carmack, J. R. Lever, C. S. Cutler, C. Caldwell, R. Kannan and K. V. Katti, Proc. Natl. Acad. Sci. U. S. A. 109 (31), 12426 (2012)

224. E. B. Ehlerding and W. B. Cai, Journal of Nuclear Medicine 57 (6), 834 (2016)

225. J. Xie, S. Lee and X. Chen, Advanced Drug Delivery Reviews 62 (11), 1064 (2010)

226. H. B. Na, I. C. Song and T. Hyeon, Advanced Materials 21 (21), 2133 (2009)

227. T. L. Wen and K. M. Krishnan, J. Phys. D-Appl. Phys. 44 (39), 24 (2011)

228. S. Salman, T. Usami, K. Kuroda and M. Okido, Journal of Nanotechnology 2014, (2014)

229. W.-r. Lee, M. G. Kim, J.-r. Choi, J.-I. Park, S. J. Ko, S. J. Oh and J. Cheon, J. Am. Chem. Soc. 127 (46), 16090 (2005)

230. V. Sviridov, T. Gaevskaya, L. Stepanova and T. Vorobyova, (2003)

231. L. C. Nagle and J. F. Rohan, Journal of The Electrochemical Society 153 (11), C773 (2006)

232. G. O. Mallory and J. B. Hajdu, *Electroless plating: fundamentals and applications*. William Andrew, (1990),

233. J.-M. Yan, X.-B. Zhang, T. Akita, M. Haruta and Q. Xu, Journal of the American Chemical Society 132 (15), 5326 (2010)

234. Z. Zhuang, W. Sheng and Y. Yan, Advanced Materials 26 (23), 3950 (2014)

235. Z. Zhu, J. Ma, L. Xu, L. Xu, H. Li and H. Li, ACS Catalysis 2 (10), 2119 (2012)

236. A. B. Davila-Ibanez, J. L. Legido-Soto, J. Rivas and V. Salgueirino, Physical Chemistry Chemical Physics 13 (45), 20146 (2011)

237. D. Llamosa Pérez, A. Espinosa, L. Martínez, E. Román, C. Ballesteros, A. Mayoral, M. García-Hernández and Y. Huttel, The Journal of Physical Chemistry C 117 (6), 3101 (2013)

238. Y. Yin, R. M. Rioux, C. K. Erdonmez, S. Hughes, G. A. Somorjai and A. P. Alivisatos, Science 304 (5671), 711 (2004)

239. Y. Vasquez, A. E. Henkes, J. Chris Bauer and R. E. Schaak, Journal of Solid State Chemistry 181 (7), 1509 (2008)

240. E. González, J. Arbiol and V. F. Puntes, Science 334 (6061), 1377 (2011)

241. C. M. Sorensen, Magnetism. In *Nanoscale Materials in Chemistry*, John Wiley & Sons, Inc., (2002), pp 169

242. N. A. Frey, S. Peng, K. Cheng and S. Sun, Chemical Society Reviews 38 (9), 2532 (2009)

243. A. Akbarzadeh, M. Samiei and S. Davaran, Nanoscale Research Letters 7 (1), 1 (2012)

244. J. A. D. Toro, J. P. Andrés, J. A. González, P. Muñiz and J. M. Riveiro, Nanotechnology 20 (8), 085710 (2009)

Biographical Information

Sina Moeendarbari received his BSc in materials engineering-metallurgy from Semnan University, Iran, in 2009. and his MSc of materials science and engineering from University of Tehran, Iran, in 2012. During his master's study, he worked in the formability and tribology labs at University of Tehran on the high-temperature mechanical and tribological properties of magnesium alloys. Then, Sina joined Dr. Yaowu Hao's group as a PhD student in 2012, where he conducted research in Nanoscale Materials lab fabricating novel nanostructures, and investigating their magnetic and optical properties. Sina Moeendarbari received his PhD of materials science and engineering at the University of Texas at Arlington in 2016. His research interests included the fabrication, fundamental properties, and applications of nanoscale materials. Some of the projects he worked on includes magnetic properties of metallic nanovoid arrays, radiosensitizing effect of novel gold nanoparticles for cancer radiotherapy enhancement, synthesis of silver nanostructures to make SERS-based sensors, synthesis bimetallic nanoparticles for catalytic applications and biomedical imaging, and developing nanoscale brachytherapy seeds (nanoseeds) for internal radiation therapy of malignant solid tumors.